

**NOVEL APPROACHES TO THE
FABRICATION OF NANOSCALE DEVICES**

Nilanthy Balakrishnan, MSc by Research in Physics (Dist).

Thesis submitted to the University of Nottingham
for the degree of Doctor of Philosophy
October 2014

Abstract

This thesis describes the effects of a *post-growth* hydrogenation on as-grown samples and device structures based on III-N-V and III-V semiconductor compounds. The spectral response of quantum wells (QWs) or superlattices (SLs) are tuned by the control dissociation of N-H complexes using a focused laser beam (*photon* assisted dissociation) or by thermal annealing. These approaches could be implemented in other materials and heterostructure devices, and offer the advantage of enabling an accurate control of the spectral response of a device using a layer compound with a single N-concentration. A focused laser beam is also used to diffuse hydrogen from the *p*-type contact layer towards the III-N-V superlattice in the intrinsic region of a *p-i-n* diode, thus creating preferential injection paths for the carriers and creating nanoscale light emitting diodes. Opportunities for realizing a movable micron size-light emitting diode (μ -LED) are also demonstrated.

Moreover, room temperature electroluminescence from semiconductor junctions formed from combinations of *n*-InSe, *p*-InSe, *p*-GaSe and *n*-In₂O₃ is demonstrated. These *p-n* junctions are fabricated using mechanical exfoliation of Bridgman-grown crystals and a simple mechanical contact method or thermal annealing. These results demonstrate the technological potential of mechanically formed heterojunctions and homojunctions of direct band gap layered GaSe and InSe compounds with an optical response over an extended wavelength range, from the near-infrared to the visible spectrum. These layered crystals could be combined in different sequences of layer stacking, thus offering exciting opportunities for new structures and devices.

List of publications

1. N. Balakrishnan, A. Patanè, O. Makarovsky, A. Polimeni, M. Capizzi, F. Martelli and S. Rubini. Laser writing of the electronic activity of N- and H-atoms in GaAs. *Applied Physics Letters* **99**, 021105 (2011).
2. N. Balakrishnan, G. Pettinari, O. Makarovsky, L. Turyanska, M. W. Fay, M. De Luca, A. Polimeni, M. Capizzi, F. Martelli, S. Rubini and A. Patanè. Band-gap profiling by laser writing of hydrogen-containing III-N-Vs. *Physical Review B* **86**, 155307 (2012).
3. G. Pettinari, N. Balakrishnan, O. Makarovsky, R.P. Campion, A. Patanè, A. Polimeni and M. Capizzi. A micrometer-size movable light emitting area in a resonant tunneling light emitting diode. *Applied Physics Letters* **103**, 241105 (2013).
4. N. Balakrishnan, G. Pettinari, O. Makarovsky, M. Hopkinson, and A. Patanè. Tunable spectral response by hydrogen irradiation of Ga(AsN) superlattice diodes. *Applied Physics Letters* **104**, 242110 (2014).
5. N. Balakrishnan, Z. R. Kudrynskyi, M. W. Fay, G. W. Mudd, S. A. Svatek, O. Makarovsk, Z. D. Kovalyuk, L. Eaves, P. H. Beton, and A. Patanè. Room temperature electroluminescence from mechanically –formed van der Waals III-VI homojunctions and heterojunctions. *Advanced Optical Materials* **2**, 1064 (2014)

List of conference abstracts

1. N. Balakrishnan, A. Patanè, O. Makarovsky, A. Polimeni, M. Capizzi, F. Martelli and S. Rubini: Photodissociation of N-H complexes in dilute nitride Ga(AsN): *UK Semiconductors 2011, Sheffield, UK; 07/2011.*
2. N. Balakrishnan, G. Pettinari, O. Makarovsky, M. W. Fay, A. Polimeni, M. Capizzi, F. Martelli, S. Rubini, and A. Patanè: In-plane band gap profiling by laser writing of hydrogenated Ga(AsN): *European Materials Research Society Spring meeting, Strasbourg, France; 05/2012.*
3. N. Balakrishnan, G. Pettinari, O. Makarovsky, M. W. Fay, A. Polimeni, M. Capizzi, F. Martelli, S. Rubini, and A. Patanè: In-plane band gap profiling by laser writing of hydrogen-containing III-N-V alloys: *31st International Conference on the Physics of Semiconductors, Zurich, Switzerland; 08/2012.*
4. N. Balakrishnan, G. Pettinari, L. Turyanska, O. Makarovsky, L. Turyanska, M. W. Fay, M. De Luca, A. Polimeni, M. Capizzi, F. Martelli, S. Rubini, and A. Patanè: Laser writing of hydrogen containing III-N-Vs: *16th International Conference on Modulated Semiconductor Structures, Wroclaw, Poland; 07/2013.*
5. G. Pettinari, N. Balakrishnan, O. Makarovsky, R. P. Campion, A. Polimeni, M. Capizzi, and A. Patanè: A movable light emitting area in resonant tunneling diodes: *16th International Conference on Modulated Semiconductor Structures, Wroclaw, Poland; 07/2013.*
6. G. Pettinari, N. Balakrishnan, O. Makarovsky, R. P. Campion, A. Polimeni, M. Capizzi, and A. Patanè. A movable light emitting area in resonant tunneling diodes: *The 18th International conference on Electron Dynamics in Semiconductors, Optoelectronics and Nanostructures, Matsue, Japan; 07/2013.*

7. N. Balakrishnan, G. Pettinari, O. Makarovsky, M. Hopkinson, and A. Patanè: Tunable spectral response of a Ga(AsN) superlattice diode by post-growth hydrogenation and thermal annealing: *UK Semiconductors 2014, Sheffield, UK; 07/2014.*
8. N. Balakrishnan, G. Pettinari, A. Patanè, O. Makarovsky, A. Polimeni, M. Capizzi, and M. Hopkinson: Using hydrogen to engineer the electronic band structure of superlattice LEDs based on Ga(AsN): *32nd International Conference on the Physics of Semiconductors, Austin, Texas; 08/2014.*
9. N. Balakrishnan, G.W. Mudd, S. A. Svatek, T. Ren, A. Patanè, O. Makarovsky, L. Eaves, P. H. Beton, Z. D. Kovalyuk, G. V.Lashkarev, Z. R. Kudrynskyi and A. I. Dmitriev: Tuning the Band gap of Exfoliated InSe Nanosheets by Quantum Confinement: *32nd International Conference on the Physics of Semiconductors, Austin, Texas; 08/2014.*

Acknowledgements

First of all, I wish to express my heartfelt thanks to my supervisor, Prof. Amalia Patanè, for providing me with the opportunity to work under her supervision, guiding me throughout this research work, and giving valuable advices and encouragement, which allowed me to carry out my PhD research successfully.

Secondly, my thanks go to Dr. Giorgio Pettinari and Dr. Oleg Makarovsky for their support in the laboratory and fruitful discussions in planning experiments, interpreting results and theoretical modellings.

I am grateful to Prof. A. Polimeni and Prof. M. Capizzi (The University of Rome, Italy) for providing hydrogenation facilities for this research study, and for their contribution to our join publications.

I thank Dr. F. Martelli and Dr. S. Rubini (TASC-INFM-CNR, Italy), Prof. A. Forchel (University of Wuerzburg, Germany), Dr. W. Stolz (Philipps-University, Marburg, Germany), Dr. R. P. Champion (The University of Nottingham, UK), Dr. M. Hopkinson (The University of Sheffield, UK) and Prof. Z. Kovalyuk and Mr. Z. Kudrynskyi (Institute for Problems of Materials Science, The National Academy of Sciences of Ukraine Chernivtsi, Ukraine) for growing the samples for this research.

I acknowledge the University of Nottingham, the EU (under grant agreement N° PIEF-GA-2010-272612), the COST Action MP0805 and the Engineering and Physical Sciences Research Council (EPSRC) for funding this research work.

My special thanks go to my colleagues for their moral supports and providing a fantastic life in the Wendy house.

Physical constants

Quantity	Symbol	Value	Unit
Boltzmann constant	k_B	1.38065×10^{-23}	JK^{-1}
Electron charge	e	1.60218×10^{-19}	C
Electron mass in vacuum	m_0	9.10938×10^{-31}	kg
Permittivity in vacuum	ϵ_0	8.85419×10^{-12}	Fm^{-1}
Plank constant	h	6.62617×10^{-34}	Js
Reduced Plank constant ($h/2\pi$)	\hbar	1.05458×10^{-34}	Js
Speed of light in vacuum	c	2.99792×10^8	ms^{-1}

List of Contents

Abstract	i
List of publications	ii
List of conference abstracts	iii
Acknowledgements	v
Physical constants	vi
1 Introduction	1
1.1 Motivation	2
1.2 Thesis overview	4
2 Dilute nitride III-V:H alloys and III-VI van der Waals crystals	6
2.1 Effect of N- and H-atoms on the electronic properties of III-Vs	7
2.1.1 Nitrogen incorporation in III-V compounds	7
2.1.1.1 Band anticrossing model of the dilute nitride III-V alloys	9
2.1.1.2 Electron effective mass in dilute nitride III-V alloys	11
2.1.2 Hydrogen in III-V compounds	12
2.1.2.1 Hydrogen-impurity complexes in III-Vs	13
2.1.3 Hydrogen in dilute nitride III-V alloys	14
2.1.3.1 Hydrogen diffusion in dilute nitride III-V alloys	16
2.2 van der Waals layered crystals	17
2.2.1 III-VI layered semiconductors	18
2.2.1.1 Rhombohedral γ -InSe	19
2.2.1.2 Hexagonal ϵ -GaSe	23

3 Semiconductor devices	27
3.1 <i>p-n</i> junction	27
3.2 <i>p-i-n</i> diode	35
3.2.1 Resonant tunneling diode	36
3.2.2 Superlattice	39
3.2.2.1 Kroning-Penney model	40
4 Samples and experimental setup	45
4.1 Sample growth and hydrogenation	45
4.1.1 III-N-V epilayers and QW structures	45
4.1.1.1 Ga(AsN)/GaAs QW	45
4.1.1.2 Ga(AsN) epilayer	48
4.1.1.3 (InGa)(AsN)/GaAs QW	48
4.1.1.4 Ga(PN) alloy and Ga(PN)/GaP MQW	49
4.1.2 Superlattice <i>p-i-n</i> diode structures	49
4.1.3 Resonant tunneling diodes	51
4.1.4 Mechanically-formed van der Waals junctions	52
4.2 Experimental techniques: transport measurements	53
4.2.1 Low noise current – voltage measurements	53
4.2.2 Capacitance – voltage measurements	54
4.3 Experimental techniques: optical studies	55
4.3.1 Room temperature micro-photoluminescence/electroluminescence	55
4.3.2 Low temperature micro-photoluminescence/electroluminescence	58
4.3.3 Laser writing	59
4.3.4 Photocurrent measurement	60
4.4 Experimental techniques: topographical/compositional studies	61

4.4.1 Scanning electron microscopy (SEM)	61
4.4.2 Transmission electron microscopy (TEM)	62
4.4.3 Atomic force microscopy (AFM)	63
5 Band-gap profiling by laser writing of H- containing III-N-Vs	65
5.1 Introduction	65
5.2 Room temperature photoluminescence studies	66
5.3 Laser writing and band gap profiling of Ga(AsN)	68
5.4 Laser writing and photonic effects in Ga(AsN)	74
5.5 In-plane band gap profiling of Ga(AsN)	76
5.6 Hydrogen containing (InGa)(AsN) and Ga(PN)	78
5.7 Summary	80
6 Tunable spectral response by hydrogen irradiation of Ga(AsN) superlattice diodes	82
6.1 Introduction	82
6.2 Room temperature electrical and optical studies	83
6.3 Low temperature optical studies	87
6.4 Controlled thermal dissociation of N-H complexes	88
6.5 Photo-stimulated diffusion of hydrogen	91
6.6 Summary	96
7 A movable resonant tunneling light emitting diode	97
7.1 Introduction	97
7.2 Effects of hydrogen on transport properties	98
7.3 Electroluminescence studies	99

7.4 Movable LED	101
7.5 Simultaneous resonant injection of electrons and holes	104
7.6 Simulation of the EL spatial map	107
7.7 Temperature dependent study	109
7.8 Summary	110
8 Room temperature electroluminescence from mechanically formed van der Waals III-VI <i>p-n</i> junctions	112
8.1 Introduction	112
8.2 Structural and compositional studies	114
8.3 Room temperature <i>I-V</i> characteristics and photoresponse	115
8.4 Room temperature electroluminescence	120
8.5 Raman spectroscopy	125
8.6 Temperature dependent electrical and optical studies	126
8.7 Summary	127
9 Conclusion and future directions	128
9.1 Band-gap profiling by laser writing of H-containing III-N-Vs	128
9.2 Tunable spectral response by hydrogen irradiation of Ga(AsN) superlattice diodes	129
9.3 A movable resonant tunneling light emitting diode	130
9.4 Room temperature electroluminescence from mechanically formed van der Waals III-VI <i>p-n</i> junctions	131
9.5 Future directions	132
Appendix A Electron effective mass in dilute nitride III-V alloys	134

Appendix B	Electronic bound states of a GaAs_{1-x}N_x/GaAs QW	136
Appendix C	Laser induced lattice heating in GaAs	140
Bibliography		143

Chapter 1

Introduction

The nitrogen-induced reduction of the band gap energy of III-V semiconductor compounds is a unique phenomenon in condensed matter physics relevant for several applications, including laser diodes and solar cells.¹ Even more remarkable is the combined effect of N and H atoms. The incorporation of hydrogen in III-N-Vs tends to passivate the electronic activity of nitrogen through the formation of N-H complexes.²⁻⁴ Recently, thermal annealing and masking techniques were used to dissociate these N-H complexes,⁵⁻⁷ thus enabling the control of the band gap energy of Ga(AsN) with sub-micron spatial resolution.

This thesis presents a novel technique that enables a similar control. We control the electronic activity of N- and H-atoms in III-N-V quantum wells (QWs) using a focussed laser beam. We investigate the laser-induced modification of the N-H bonds by micro-photoluminescence (μ PL) spectroscopy and mapping, and Scanning Electron Microscopy (SEM). We show that the laser-assisted dissociation of the N-H complexes is a local process that can be activated at temperatures that are significantly smaller than those (> 200 °C) required for thermal dissociation. This provides a means of patterning with submicron spatial resolution *in-plane* band gap profiles of different shapes. Since this direct laser writing technique does not require lithography and etching, it offers a promising route to cost-effective, large-volume and fast nanofabrication methods.

We tune the spectral response of Ga(AsN) superlattice *p-i-n* diodes by controlled thermal dissociation of N-H complexes. This approach offers the advantage of enabling an accurate control of the spectral response of a diode using a

single wafer, thus providing an alternative to re-growth techniques. Opportunities for realizing a movable micro-LED are also demonstrated in a GaAs/AlAs resonant tunnelling diode.

This thesis also presents preliminary results on the development of a new class of semiconductor structures based on van der Waals III-VI (InSe and GaSe) homojunctions and heterojunctions. Flakes with thickness between 1 nm and 10 μm can be prepared from the Bridgman-grown crystals by mechanical exfoliation and then laid one onto another. The adhesive van der Waals forces between the layers enable to form a homojunction (n -InSe on p -InSe) or a heterojunction (p -GaSe on n -InSe). Heterojunctions based on n -In₂O₃ on p -InSe, can be also fabricated by annealing the freshly cleaved p -InSe flake at temperature $T = 450$ °C for 96 hours.⁸ All these p - n junctions show rectification behaviour in the I - V characteristics and electroluminescence at room temperature.

1.1 Motivation

Research in Nanoscience and Nanotechnology will drive the scientific and technological development of future years with revolutionary perspectives in many different aspects of our society, from materials to telecommunications and energy, from medicine to the environment. Future large-volume applications will require fast and flexible methods to fabricate and miniaturize electronic and photonic components. One of the objectives of my PhD project is to develop novel approaches to the fabrication of nanoscale current channels and nano-LEDs that exploits the controlled diffusion or removal, by laser writing, of hydrogen atoms in different p - i - n LED structures and dilute nitride III-V alloys. Laser writing is a fast, flexible and low-cost approach that has the potential for large-volume applications and for

making miniaturized components of photonic devices. Nano-LEDs are of potential use for inter- and intra-chip optical communication, ultrahigh-density optical information storage, high resolution micro-displays, Lab-on-a-Chip experiments, bio-imaging, etc.

This project is motivated by the recent fabrication of nano-LEDs by diffusing Mn^{2+} in *p-i-n* structures based on a *p*-type GaMnAs layer and a GaAs/AlAs QW at the University of Nottingham [O. Makarovskiy *et al.*, *Adv. Mater.* **22**, 3176 (2010)]. These nano-LEDs are stable, reproducible, and can work at high current densities ($> 108 \text{ A/m}^2$) over the temperature range 4 - 325 K for a long time (> 100 hours). Also, when a forward bias is applied to the *p-i-n* junction, a small region of the device emits light at a bias well below the threshold voltage for emission from the non-annealed regions, thus indicating the creation of a preferential tunneling path for the injected carriers. The use of hydrogen rather than manganese as mobile atom in the new nano-LEDs presents several and important advantages: hydrogen is highly mobile; it can be incorporated after the material growth and fabrication; it can be incorporated using low energy implantation techniques.

My PhD project also aimed to fabricate semiconductor junction devices using mechanical exfoliation of Bridgman-grown III-VI van der Waals crystals and a simple mechanical contact method or thermal annealing. The study of layer materials lies in the extreme anisotropy in their physical properties and in the ability of the crystals to cleave down to thicknesses of the order of a unit cell. This makes it possible to study solids as nearly two-dimensional arrays. The possibility of making multilayer van der Waals heterostructures has been demonstrated experimentally only recently [K. Geim and I. V. Grigorieva, *Nature* **499**, 420 (2013)]. These van der Waals heterostructures are made from more than two atomically thin crystals, and

only graphene and few-layer hBN, MoS₂ and WS₂ have been used. The III-VI layered semiconductors (InSe and GaSe) provide an important class of direct-band gap semiconductors, whose band gap can be tuned in the near infrared spectral range when the crystals are exfoliated into nanometer-thick flakes, and are promising candidates for nanoscale optoelectronics and LEDs.

1.2 Thesis overview

This thesis is structured as follows.

Chapter 2 discusses the effect of N- and H-atoms on the electronic properties of GaAs and an introduction to III-VI layered van der Waals crystals.

Chapter 3 introduces the basic principles of semiconductor devices studied in this research, such as *p-n* junctions, *p-i-n* diodes based on superlattices and resonant tunnelling diodes.

Chapter 4 provides a brief overview of the sample growth, the hydrogenation technique, and the experimental techniques used during my PhD.

Chapter 5 introduces the photon-assisted N-H complex dissociation and *in-plane* band gap profiling using a focussed laser beam. Light emitting sub-micron spots are produced by laser writing with different exposure conditions (laser wavelength and power) and the resonant photo-dissociation condition is discussed.

Chapter 6 presents the tunable spectral response of a hydrogenated Ga(AsN)/AlAs superlattice *p-i-n* diode by the controlled thermal dissociation of N-H complexes. A focused laser beam is also used to diffuse hydrogen from the *p*-type GaAs contact layer towards the superlattice, thus creating a preferential path for the injection of carriers and activating a nanoscale light emitting region. The thermal

activation energy of these hydrogen related states is determined from the temperature dependent electroluminescence studies.

Chapter 7 describes the realization of a bias controlled, micrometer-size movable light emitting area in an inorganic resonant tunnelling light emitting diode containing a GaAs/AlAs quantum well (QW). *Post-growth* hydrogenation passivates the C-dopants on the *p*-type contact layer of the diode resulting into an increase of the resistivity of the *p*-type contact layer. This causes a lateral voltage drop from the metal contact edge towards the center of the diode. Thus the resonant injection of electrons and holes into the QW sub-bands occurs at different positions for each applied bias, enabling the realization of a movable-LED.

Chapter 8 demonstrates a novel approach to the fabrication of *p-n* junctions based on III-VI van der Waals crystals by exfoliation and mechanical contact method or thermal annealing. These *p-n* junctions show room temperature electroluminescence, thus demonstrating the technological potential of mechanically formed *p-n* junctions of layered III-VI crystals with an optical response over an extended wavelength range, from the near-infrared to the visible spectrum.

Chapter 9 concludes this thesis by providing a summary of the main findings and a proposal for future studies.

This Thesis contains three appendixes. Appendix A describes the derivation of the dependence of the electron effective mass in dilute nitride III-V alloys on the N-content. Appendix B describes the electronic bound states of a Ga(AsN)/GaAs QW using the band anticrossing (BAC) model and a QW square potential model. Appendix C describes the laser induced lattice heating in GaAs.

Chapter 2

Dilute nitride III-V:H alloys and III-VI van der Waals crystals

This chapter discusses the effects of hydrogen on the electronic properties of dilute nitride III-V alloys. The effects of hydrogen in crystalline semiconductors have attracted considerable interest during several decades. It is well known that hydrogen can passivate non-radiative centers, point and extended defects, neutralizing the effect of dopants, and traps in semiconductors.⁹⁻¹¹ It can also modify pure InN to a *p*-type semiconductor by increasing the band gap,¹² turns the metallic ferromagnetic state of GaMnAs to a semiconducting paramagnetic state by passivating the electric activity of the Mn acceptors,¹³ and transforms graphene from a highly conductive semimetal into an insulator.¹⁴ In particular, hydrogen leads to tunable and reversible changes in the electronic, optical, and structural properties of dilute nitride III-Vs.³ Also, hydrogenation and masking techniques provide a novel approach for the fabrication of nanostructures, such as quantum wires⁴ and quantum dots¹⁵⁻¹⁶ in the growth plane.

This chapter also discusses the electronic properties of III-VI van der Waals layered crystals such as InSe and GaSe. The remarkable properties of graphene, such as its high carrier mobility ($\mu \sim 10^5 \text{ cm}^2\text{V}^{-1}\text{s}^{-1}$ at $n \sim 10^{11} \text{ cm}^{-2}$ and $T = 300 \text{ K}$),¹⁷ superior thermal and electric conductivity,¹⁸ and semi-metallic properties¹⁹ promoted the research on graphene-like layered materials, including dichalcogenides (MoS₂, MoSe₂, WS₂, WSe₂ etc.) and III-VI layered semiconductors (InSe and GaSe). The weak interlayer interaction in these materials enable one to mechanically exfoliate bulk crystals into atomically thin layers.²⁰⁻²⁴ These layered crystals have a thickness dependent electronic band structure.²⁴⁻²⁷ The realization of field-effect transistors

(FETs)^{21-22, 28} and photodetectors²⁹⁻³⁰ based on layered dichalcogenides promoted the research on III-VI layered semiconductors. FETs based on ultrathin layered GaSe ($\mu \approx 0.6 \text{ cm}^2\text{V}^{-1}\text{s}^{-1}$ and I_{ON}/I_{OFF} ratio $\approx 10^5$ at $T = 300 \text{ K}$)³¹ and UV–visible range photodetectors with outstanding responsivity ($2.8 - 12.3 \text{ AW}^{-1}$) and quantum efficiency ($\sim 1367 \%$) based on few-layer GaSe²³ and InSe³²⁻³³ can be all fabricated by mechanical exfoliation.

2.1 Effect of N- and H-atoms on the electronic properties of III-Vs

The controlled incorporation of impurities in a semiconductor crystal during or after the synthesis is routinely used to tailor electronic properties and has played a key role in the discovery of physical phenomena and their exploitation in device applications. Among various elements, nitrogen and hydrogen in III-V compounds have revealed intriguing effects of fundamental interest and technological importance. In this section we discuss the unique effect of nitrogen (N) and hydrogen (H) atoms on the electronic properties of III-V compounds.

2.1.1 Nitrogen incorporation in III-V compounds

During the last decade, III-V-N alloys such as Ga(AsN), Ga(PN), (InGa)(AsN), In(NAsP), and (InGa)(PN) have received considerable attention due to their unique electronic properties and useful applications in optoelectronic devices.^{1, 34-36} In these alloys, the group V anions are partially substituted by a low concentration of highly electronegative N atoms (see Figure 2.1a).³⁷ In general, a smaller lattice constant increases the band gap; however, nitrogen with a smaller size causes a giant band gap bowing by stretching and compressing the neighbouring bonds,³⁸ see Figure 2.1b. Moreover, a small amount ($\sim 1\%$) of N in III-Vs produces a considerable decrease in

the electron mobility,³⁹ an increase of the electron effective mass⁴⁰ and an unusual response to external perturbations, such as hydrostatic pressure.⁴¹ All these effects are due to the formation of N-related localized states that are resonant with (or close to) the extended states of the conduction band (CB) of the host lattice, see Figure 2.1c.⁴² Many of these effects can be explained by a two-level band anticrossing (BAC) model in which the extended conduction band (CB) states of III-V admix and hybridize with the localized N-level above the CB edge.⁴¹ This model is described in the following section.

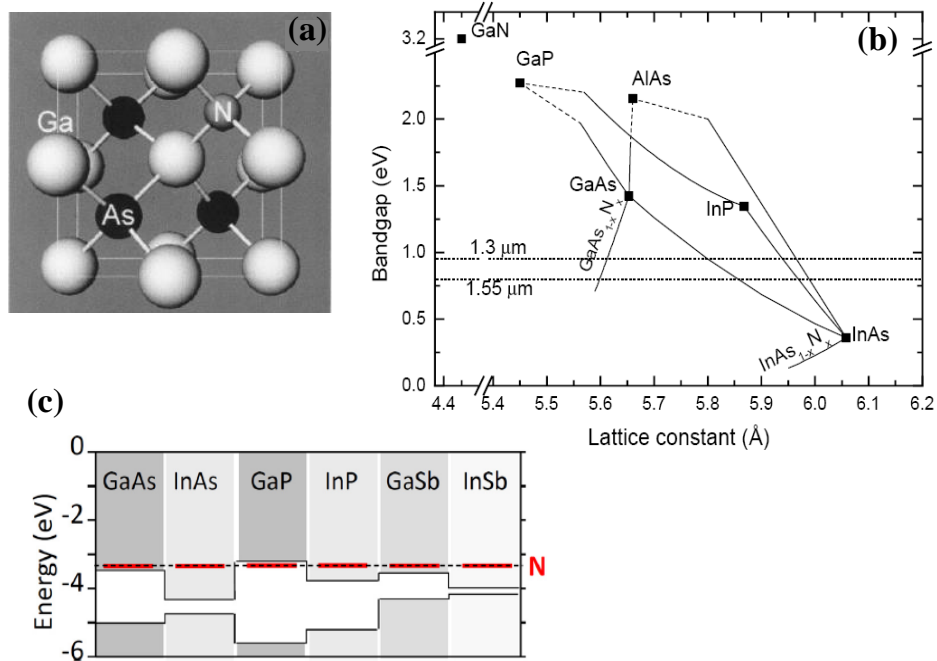


Figure 2.1: (a) Unit cell of GaAs (zincblende structure) in which an As atom is replaced by a N atom to form Ga(AsN). (b) Dependence of the band gap energy on the lattice constant for III-V semiconductors. The solid and dashed lines are, respectively, the ternary compounds' direct and indirect band gaps. The horizontal lines represent fiber-optical communication wavelengths (1.55 and 1.3 μm). (c) Band lineups and positions of the N level (horizontal red lines) for a range of III-V compounds. For each material, the upper and lower lines indicate the position of the conduction band minima and the valence band maxima, respectively. Pictures reproduced from Ref [37, 38, and 42].

2.1.1.1 Band anticrossing model of the dilute nitride III-V alloys

The unexpected red shift of the photoluminescence (PL) and absorption edge of the dilute Ga(AsN) alloy, instead of a blue shift, was firstly reported by Weyers et al.⁴³ This discovery has opened an important question about the physical mechanism responsible for this unusual behavior. Wei and Zunger⁴⁴ have explained the origin of this red shift and corresponding band gap reduction in terms of an optical bowing parameter, which is largely dependent on the N-content. On the other hand, the two-level BAC model has explained the behavior of many highly mismatched alloys (HMAs) and was originally developed by W. Shan et al.⁴¹ to describe the dependence of the band gap on composition and pressure for the (InGa)(AsN) alloy. The BAC model has predicted many interesting effects, such as an enhancement of the electron effective mass⁴⁰ and donor binding energy⁴⁵ due to N-incorporation, which have been experimentally proved.

The two-level BAC model is the solution of the degenerate perturbation theory applied to a system of localized and extended states. Following W. Walukiewicz et al.,⁴⁶ the interaction between these two types of states leads to the following eigenvalue problem

$$\begin{vmatrix} E(k) - E_M(k) & -V_{NM} \\ -V_{NM} & E(k) - E_N \end{vmatrix} = 0, \quad (2.1)$$

where $E_M(k)$ and E_N are, respectively, the energies of the CB minima of the host material and the N level measured with respect to the top of the valence band (VB), $V_{NM} = \langle k|V|N \rangle$ is the matrix element describing the interaction between the localized N states and extended CB state, and V is the potential generated by a single N-atom on a substitutional site. The two possible solutions of this problem can be written as

$$E_{\pm}(k) = \frac{1}{2} \left\{ (E_N + E_M(k)) \pm \sqrt{[(E_N - E_M(k))^2 + 4V_{NM}^2]} \right\}. \quad (2.2)$$

If we assume that V_{NM} is independent of k near the CB edge, then V_{NM} can be written as $V_{NM} = C_{NM}x^{1/2}$, where C_{NM} is a constant dependent on the host matrix and x is the mole fraction of substitutional N. Therefore Eq. 2.1 can be also rewritten as

$$E_{\pm}(k) = \frac{1}{2} \left\{ (E_N + E_M(k)) \pm \sqrt{[(E_N - E_M(k))^2 + 4C_{NM}^2 x]} \right\}. \quad (2.3)$$

In the BAC model, the interaction between the localized N states and extended states of the host material has been treated in the simplest possible manner. A many-impurity Anderson model has been developed to evaluate the interaction between the randomly distributed localized states and the extended states of the host material.⁴⁷ The calculations reproduced the BAC model and the imaginary part of the Green's function yields information on the CB broadening,⁴⁸ see Figure 2.2(a). The energy broadening can explain the wavelength dependence absorption coefficient and the effects of the hybridization on the transport properties of the HMAs.⁴⁷

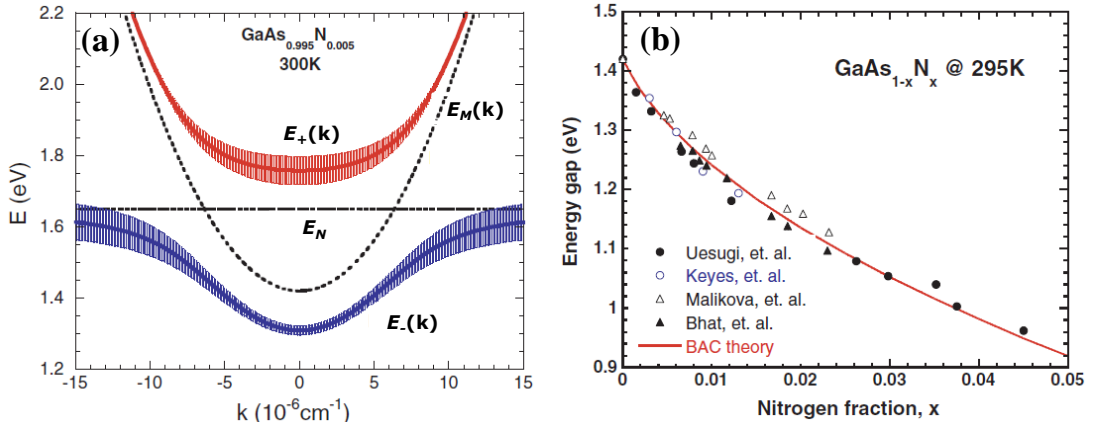


Figure 2.2: (a) (solid lines) Calculated dispersion relationships for E_{\pm} subbands of $\text{GaAs}_{0.995}\text{N}_{0.005}$ using the BAC model, Eq. 2.3. The broadening of the dispersion curves of the newly formed subbands illustrates the energy uncertainties introduced by the many-impurity Anderson model. The dashed lines show the unperturbed energies of the N level (E_N) and the GaAs conduction band. (b) Dependence of the band gap energy of $\text{GaAs}_{1-x}\text{N}_x$ on x reported by different groups. The solid line is the best fit to the data with $C_{NM} = 2.7$ eV and a N-level $E_N = 1.65$ eV. Pictures reproduced from Ref. [47].

2.1.1.2 Electron effective mass in dilute nitride III-V alloys

The incorporation of N in III-Vs not only changes the band gap energy, but also it modifies the curvature of the energy-wave vector $E(k)$ dispersion of the conduction band, thus changing the electron effective mass m^* . The second derivative effective mass, m^* , can be written as

$$m^*(k) = \frac{\hbar^2}{\frac{d^2 E(k)}{dk^2}}. \quad (2.4)$$

Using Eq. 2.4 and the k -dependence of the $E_-(k)$ subband in Eq. 2.3, we find that the effective mass at $k=0$ can be expressed as

$$m^* = \frac{2m_0^*}{\left[1 - \frac{(E_N - E_M(k))}{\sqrt{(E_N - E_M(k))^2 + 4 C_{NM}^2 x}} \right]}, \quad (2.5)$$

where m_0^* is the electron effective mass in the III-V. The detailed derivation of Eq. 2.5 is given in Appendix A.

The x dependence of m^* in Ga(AsN) is shown in Figure 2.3. In this Figure the value of m^* is normalized to the value of the electron mass in vacuum (m_0).

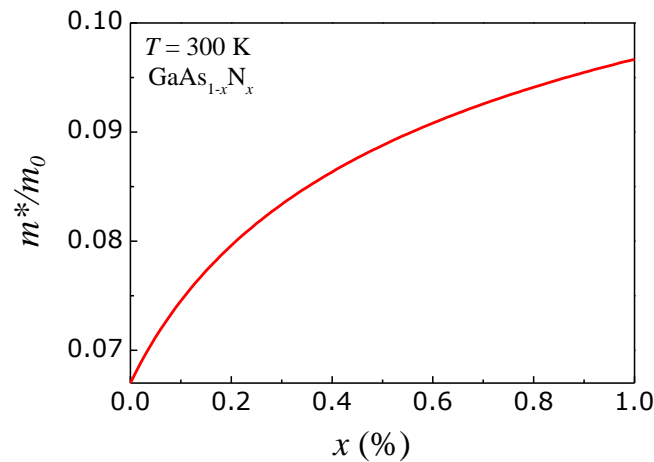


Figure 2.3: Dependence of the electron effective mass on x in GaAs_{1-x}N_x calculated using the BAC model at $T = 300$ K ($E_N = 1.65$ eV, $E_M(k=0) = 1.424$ eV, $C_{NM} = 2.7$ eV and $m_0^* = 0.067 m_0$).

2.1.2 Hydrogen in III-V compounds

The unavoidable presence of hydrogen during the sample growth and/or device processing steps, has stimulated a great interest in the effects of H in semiconductor compounds.¹⁰ The properties of hydrogen interstitial in Si are well understood experimentally and theoretically.⁴⁹⁻⁵¹ The H impurity can exist in three different charge states H^+ , H^0 , and H^- depending on the occupied site of the crystal lattice.⁵⁰⁻⁵¹ In III-V semiconductor compounds such as GaAs, the general behavior of isolated H is expected to be similar to that in Si.⁹ This section reviews the recent literature on isolated hydrogen in III-Vs.

Theoretical studies show that in GaAs the body centred (BC) site is a stable configuration for both H^0 and H^+ states, but H^- is stable at the antibonding site of the Ga atom (AB_{Ga}), see Figure 2.4.⁵² On the other hand, in *p*-GaAs the H^+ state is stable at the bond center site. In *n*-type GaAs, H^- is ascribed to the interstitial tetrahedral site as a result of hopping mechanisms between antibonding sites.⁵³ Photoluminescence (PL) studies on unintentionally lightly doped *p*-GaAs show that the Fermi level raises in the band gap following the hydrogen incorporation.⁵⁴ The hydrogen irradiation activates the donor-acceptor (*D-A*)-like PL bands. This is confirmed by theory.⁵⁵ Near band-edge states induced by hydrogen were predicted by A. Amore Bonapasta and co-authors.⁵⁵ In the case of H_{BC}^+ , a donor level and an acceptor level can arise, 34 meV below the CB edge and 30 meV above the VB edge respectively.⁵⁵ Finally, the formation of dihydrogen complexes and molecules in GaAs was also predicted.⁵² Positive and negative hydrogen ions easily diffuse in III-Vs and form complexes with dopants and other impurities, which turn out to be passivated.⁹ The following section discusses hydrogen-impurity complexes.

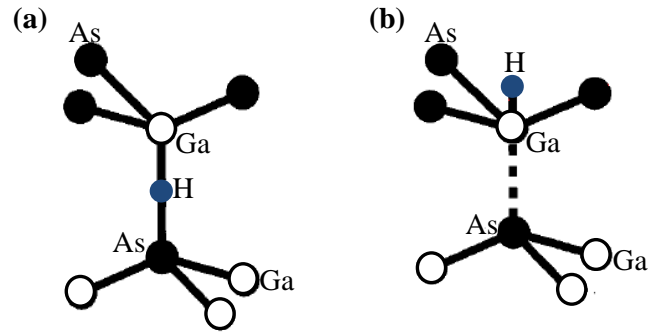


Figure 2.4: The relaxed structures for a single interstitial hydrogen atom as referred to in the text. The hydrogen atom is located at (a) the Ga-As bond-centered site, (b) the antibonding site of Ga atom. Picture reproduced from Ref. [52].

2.1.2.1 Hydrogen-impurity complexes in III-Vs

Direct observation of PL emission from H-related complexes in *post-growth* hydrogenated GaAs and (AlGa)As epilayers, and In(GaAs) multiquantum wells have been reported by M. Capizzi and co-authors.⁵⁶ They observed free electron – acceptor (e -A) transitions from three different impurities such as Zi, Si, and C. Carbon is the favored p -type dopant in III-Vs due to its low diffusivity compared to that of other p -type dopants such as Be and Zn. Also, high concentrations ($10^{20} - 10^{21} \text{ cm}^{-3}$) of C can be incorporated into the material during the growth.⁵² In As-containing III-Vs, C atoms tend to sit on the As-lattice sites, thus acting as acceptors.^{52, 57-58} Hydrogen incorporation passivates the electronic activity of C_{As} acceptors through the formation of $H-C_{As}$ complexes.⁵⁹ The $H-C_{As}$ complex more willingly dissociates under minority carrier injection. There are no defect levels in the band gap associated with the neutral $H-C_{As}$ complex. Thus the charge state of the complex is independent of the Fermi level.⁵² Figure 2.5 shows the modelled configurations of the $H-C_{As}$ complex in GaAs.⁵² As shown in Figure 2.5a, the H atom lies on the body centered (BC) site between the C and Ga atoms. This is a stable configuration for the neutral $H-C_{As}$ complex. Figure 2.5b shows the most stable

configuration of the H-C_{As} complex where the H atom is strongly bonded to the As atom in the neutral charge state and to the Ga atom in the negative charge state.⁵²

Finally, Figure 2.5c shows a H atom strongly bonded to a C atom on the anti-bonding site.

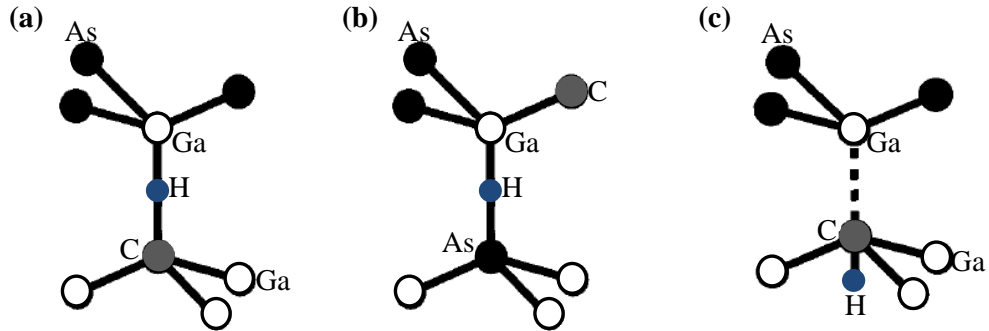


Figure 2.5: The relaxed structures of H-C_{As} pairs in GaAs. The H atom is located at (a) a C-Ga body centered site, (b) a Ga-As body centered site with C as a nearest neighbor of the Ga, and (c) the anti-bonding of the C site. Picture reproduced from Ref [52].

2.1.3 Hydrogen in dilute nitride III-V alloys

Hydrogen is an impurity of fundamental importance in semiconductor materials due to its high diffusion rate and ability to react with a wide variety of crystal defects.⁹⁻¹¹ In particular, the incorporation of H in III-N-Vs acts to neutralize the electronic activity of N through the formation of N-H complexes, thus reversing the effect of the N-atoms on the band structure of the host crystal.³⁻⁴ Moreover, H turns the tensile strain of Ga(AsN) into compressive and induces an expansion of the lattice constant, which can become larger than that of GaAs.⁶⁰⁻⁶¹ This section reviews the recent literature on N-H complexes.

Several theoretical calculations initially proposed nitrogen-stabilized $\text{H}_2^*(\text{N})$ structures with one H-atom at a BC site and a second H-atom at an AB site of the N-atom along the same Ga-N $\langle 111 \rangle$ axis to explain the band gap red-shift caused by H.⁶²⁻⁶⁷ However, these $\text{H}_2^*(\text{N})$ complexes were inconsistent with the vibrational

properties of hydrogenated Ga(AsN) studied by infrared (IR) absorption spectroscopy.⁶⁸⁻⁶⁹ These results showed that N has two in-equivalent, weakly coupled N-H stretching modes.⁶⁸⁻⁶⁹ Therefore, alternative N-2H complexes with C_{2V} symmetry or with a canted C_{1h} geometry have been proposed.^{2, 69-71} The observed vibrational properties are more consistent with the canted N-2H complexes with C_{1h} symmetry,^{3, 69} see Figure 2.6. Additionally, x-ray absorption spectroscopy and theory provided evidence for N-2H complex with canted or asymmetric C_{2V} structure, described by the C_{1h} symmetry, consistent with the IR experiment.^{70, 72} These N-2H complexes with symmetry C_{1h} or asymmetric C_{2V} configurations are responsible for nitrogen passivation.^{3, 72}

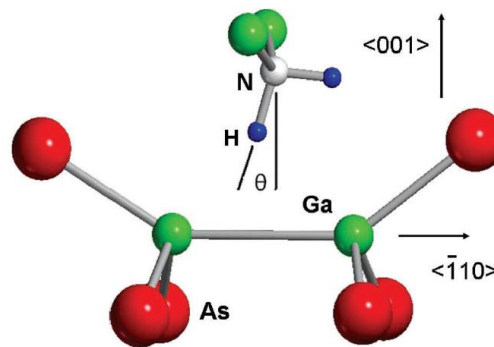


Figure 2.6: The relaxed C_{1h} complex in Ga(AsN). The angle θ is the canting angle of the N-passivating C_{1h} center. Two H^+ ions break two Ga-N bonds and form $N-2H_{BC}^{2+}$ complex. Then this complex transforms to canted N-2H complex by passing the positive charges to Ga atoms, thus forming the weak Ga-Ga bond.⁶⁵ Picture reproduced from Ref [73].

The x-ray diffraction measurement shows the evidence for a third H-atom more weakly trapped near passivated N atoms. This causes a compressive strain in the Ga(AsN) layer.⁷³ Combined thermal annealing and x-ray diffraction studies show that this third H-atom can be removed from its site at a temperature $T_a = 250$ °C with an activation energy of 1.77 eV.⁷ At the same time, the compressive strain disappears while N atoms are still electronically passivated. Annealing at higher temperatures

($T_a > 250$ °C) dissociates the N-2H complexes with an activation energy of 1.89 eV and recovers the electronic properties and the tensile strain of the as-grown Ga(AsN) lattice.⁷

2.1.3.1 Hydrogen diffusion in dilute nitride III-V alloys

R. Trotta et al. probed the hydrogen (deuterium) diffusion profile in different GaAs_{1-x}N_x samples by secondary ion mass spectroscopy (SIMS),⁷³ see Figure 2.7a. All samples were deuterated (deuterium, rather than hydrogen, was used in order to increase sizably the SIMS sensitivity) at a temperature $T_D = 300$ °C. They observed that the deuterium forefront becomes sharper with increasing N concentration. Particularly, the D concentration falls by a factor of 10 within 10 nm for $x = 1.5$ %. Remarkably, this quantity decreases with decreasing deuteration temperature, shown in Figure 2.7b for $x = 0.7$ % along with a model developed to take into account the particular formation and dissociation kinetics of the (N-2D)-D complex. Details of this study are described in the literature.⁷³

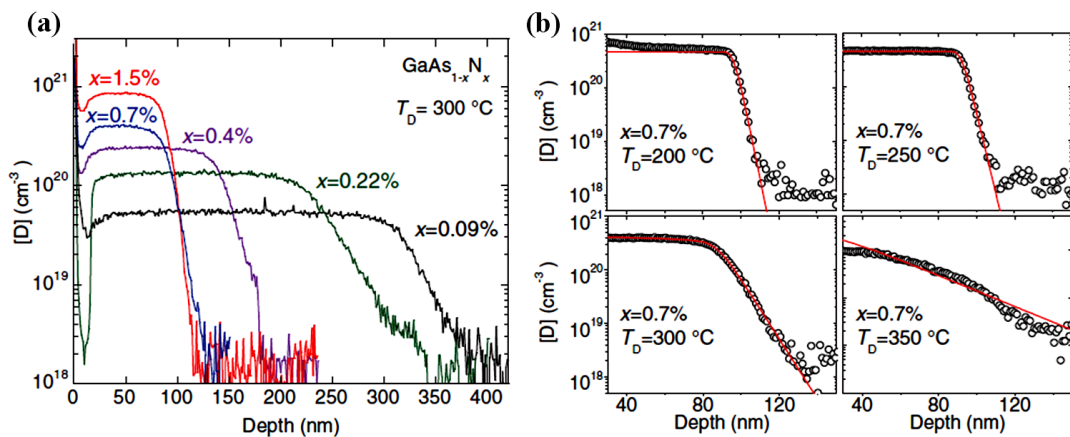


Figure 2.7: SIMS depth profile of deuterium concentration for GaAs_{1-x}N_x samples (a) with different N concentration, x , and deuterium radiation temperature of $T_D = 300$ °C, and (b) for $x = 0.7$ % and different irradiation temperatures. The origin is set at the sample surface. Picture reproduced from Ref [73].

2.2 van der Waals layered crystals

The relentless miniaturization of Si based electronics and the discovery of graphene have stimulated the research on atomically thin two-dimensional (2D) semiconductors.⁷⁴ In particular, since graphene is gapless, it is unsuitable for digital electronics,⁷⁴⁻⁷⁷ thus promoting the research on identifying alternative 2D semiconductors. Recently, a vast number of non-graphene layered compounds have received attention including hexagonal boron nitride (hBN), metallic dichalcogenides, layered semiconductors and oxides, see Figure 2.8.⁷⁹ However, only some of these crystals are classified as semiconductors and even few are stable under ambient conditions.⁷⁸

Graphene family	Graphene	hBN 'white graphene'	BCN	Fluorographene	Graphene oxide
2D chalcogenides	MoS ₂ , WS ₂ , MoSe ₂ , WSe ₂		Semiconducting dichalcogenides: MoTe ₂ , WTe ₂ , ZrS ₂ , ZrSe ₂ and so on	Metallic dichalcogenides: NbSe ₂ , NbS ₂ , TaS ₂ , TiS ₂ , NiSe ₂ and so on	
				Layered semiconductors: GaSe, GaTe, InSe, Bi ₂ Se ₃ and so on	
2D oxides	Micas, BSCCO	MoO ₃ , WO ₃	Perovskite-type: LaNb ₂ O ₇ , (Ca,Sr) ₂ Nb ₃ O ₁₀ , Bi ₄ Ti ₃ O ₁₂ , Ca ₂ Ta ₂ TiO ₁₀ and so on	Hydroxides: Ni(OH) ₂ , Eu(OH) ₂ and so on	
	Layered Cu oxides	TiO ₂ , MnO ₂ , V ₂ O ₅ , TaO ₃ , RuO ₂ and so on		Others	

Figure 2.8: Current 2D library. Monolayers proved to be stable under ambient conditions (at room temperature in air) are shaded blue; those probably stable in air are shaded green; and those unstable in air but that may be stable in inert atmosphere are shaded pink. Gray shading indicates 3D compounds that have been successfully exfoliated down to monolayers, as is clear from atomic force microscopy. After intercalation and exfoliation, the oxides and hydroxides may exhibit stoichiometry different from their 3D parents. 'Others' indicates that many other 2D crystals (including borides, carbides, nitrides etc.) have been or can be isolated. Picture reproduced from Ref [78].

In parallel with the research on graphene-like materials, the research on multilayer heterostructures and devices by stacking different 2D crystals on top of

each other has gained strength over the last three years.⁷⁹⁻⁸² In the artificial multilayer stacks, strong covalent bonds provide in-plane stability and relatively weak van der Waal forces are sufficient to keep them stacked together.⁷⁹ The possibility of fabricating such multilayer van der Waals heterostructures has been experimentally demonstrated.⁷⁹⁻⁸² Also, research on 2D chalcogenides has recently emerged due to its tunable electronic properties with layer thickness.²⁴⁻²⁷ The successful fabrication of FETs and photodetectors based on these materials have been reported.^{21-23, 28-33} This session describes the electronic properties of III-VI layered semiconductors, such as InSe and GaSe.

2.2.1 III-VI layered semiconductors

InSe and GaSe crystals are the most popular III–VI semiconductors. They have been widely investigated because of their potential applications in nonlinear optics,⁸³ terahertz generation⁸⁴ and solar energy conversion.⁸⁵ Each layer consists of four closely-packed, covalently bonded, monoatomic sheets in the sequence Se-X-X-Se (X = In, Ga). The layers are bounded together by weak van der Waals forces. This crystal structure is responsible for the anisotropy of many physical properties.⁸⁶⁻⁸⁷ In semiconductor technology, these layers serve as buffers for epitaxial growth of mismatched lattice structures.⁸⁸ Moreover, these layered crystals can form nanotubes.⁸⁹ The presence of an exciton peak near the fundamental absorption edge, the band gaps consistent with the lasing range of modern lasers, and the nonlinear properties make these crystals in demand for optoelectronics.⁹⁰

InSe and GaSe single crystals have four polytypes β , ϵ , γ , and δ varying between each other in the sequence of crystalline layer stacking, respectively, 2, 2, 3, and 4 layers in the unit cell.⁹¹ We have used Bridgman-grown crystals of

rhombohedral γ -InSe and hexagonal ε -GaSe for our experimental studies described in chapter 8. The structural and electronic properties of γ -InSe and ε -GaSe are described below.

2.2.1.1 Rhombohedral γ -InSe

The primitive unit cell of γ -InSe contains three layers, each consisting of four closely-packed, covalently bonded monoatomic sheets in the sequence Se-In-In-Se (Figure 2.9). Along the c -axis, the primitive unit cell of γ -InSe has a lattice parameter of $c = 24.961 \text{ \AA}$ and the distance between two neighboring layers is 8.4 \AA . Within each a - b plane, atoms form hexagons with lattice parameter $a = 4.002 \text{ \AA}$. The bulk InSe is usually an n -type semiconductor⁹² with a direct band gap of $E_g = 1.26 \text{ eV}$ at $T = 300 \text{ K}$ ⁹³ and anisotropic electronic properties,⁹⁴⁻⁹⁵ see Table 2.1.

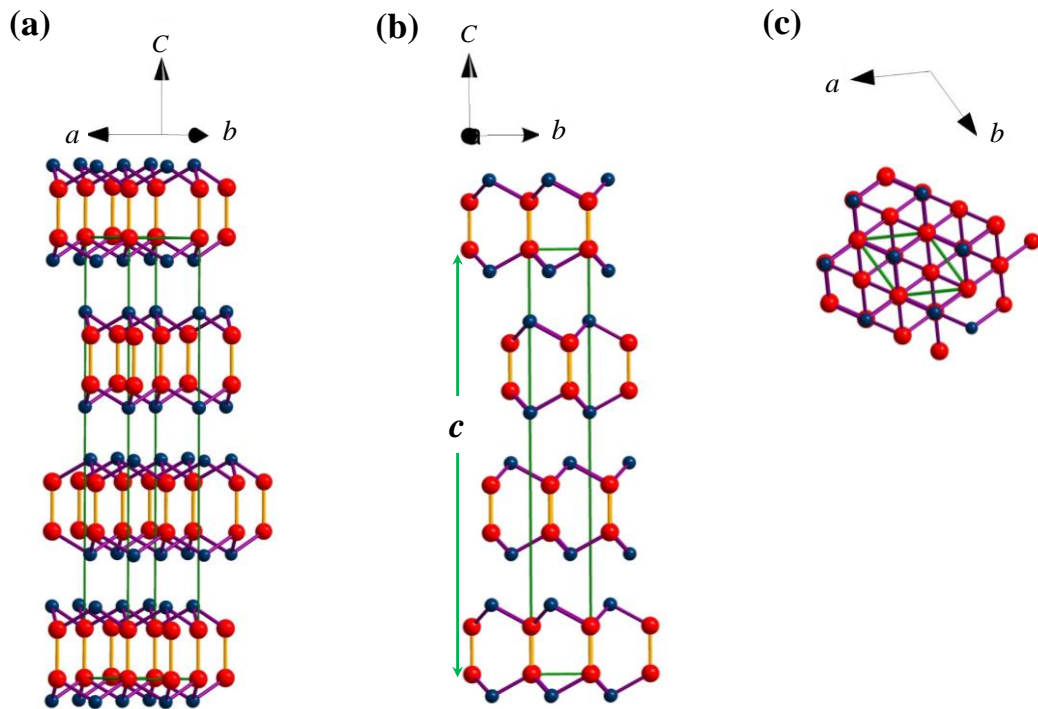


Figure 2.9: Crystal structure of rhombohedral γ -InSe (a) in three dimensions, (b) along the b - c plane, and (c) along the a - b plane. The blue spheres refer to In- and red sphere refer to Se-atoms. The unit cell has three monolayers.

Table 2.1: Electron (m_e^*), hole (m_h^*) and exciton (μ) effective masses, and static and dynamic dielectric permittivities along the c -axis and in the layer plane of γ -InSe. Table reproduced from Ref [94].

	m_e^*	m_h^*	μ	ϵ_∞	ϵ_0
$\parallel c$	$0.081 m_0$	$0.17 m_0$	$0.055 m_0$	7.0	7.6
$\perp c$	$0.138 m_0$	$0.73 m_0$	$0.116 m_0$	7.34	10.3

Recently, G. W. Mudd et al.²⁴ reported the successful exfoliation of thin layers of rhombohedral γ -InSe. It was shown that the near-band edge photoluminescence (PL) peak and absorption-induced photoconductivity undergo a strong blue-shift to higher photon energies with decreasing layer thickness, L , consistent with 2D quantum confinement of photo-excited carriers by atomically flat interfaces (Figure 2.10). They also observed a direct-to-indirect band gap crossover, which contrasts with the indirect-to-direct band gap transition previously reported for transition metal dichalcogenides as the film thickness is decreased.²⁵⁻²⁶ Consistent with this, recent theoretical studies show that a single layer of InSe has an indirect band gap with a sombrero-shaped dispersion of holes near the valence-band edge.⁹⁶

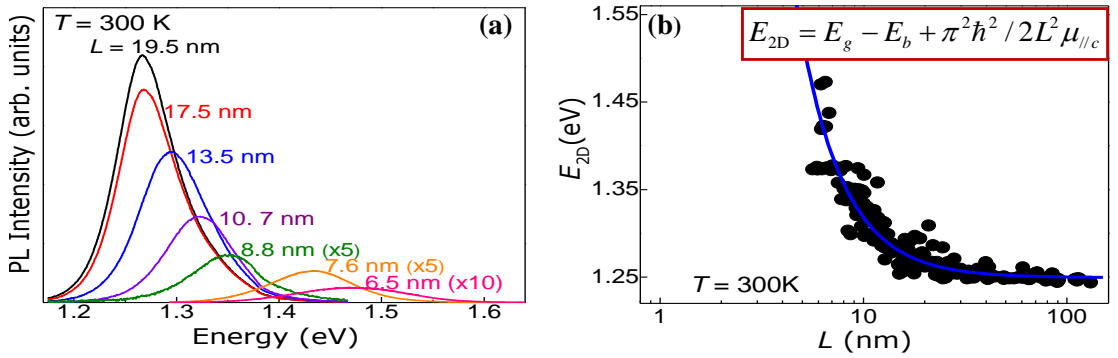


Figure 2.10: (a) Typical μ PL spectra of InSe layers at $T = 300$ K with peak energy strongly dependent on the layer thickness L ($P = 0.1$ mW and $\lambda = 633$ nm). (b) Measured dependence of the peak energy of the μ PL emission, E_{2D} , on the thickness L of the InSe layer at $T = 300$ K. The continuous line shows the calculated dependence of the exciton recombination energy for a quantum well of width L . Picture reproduced from Ref [24].

A layer thickness dependence of the resonance Raman peaks was reported by S. Lei and coworkers for γ -InSe.³² In γ -InSe, each unit cell has 12 atoms and, consequently, 36 vibrational modes. The resonant Raman spectra measured with laser excitation wavelength of $\lambda_{\text{exc}} = 514$ nm show Raman peaks at 117 cm^{-1} , 179 cm^{-1} , 201 cm^{-1} , and 227 cm^{-1} , see Figure 2.11a. The main Raman peak at 117 cm^{-1} corresponds to a non-polar phonon mode (Figure 2.11b) of energy $h\nu = 0.014$ eV. The Raman peaks tends to disappear when the number of layer is decreased to 5 layers. The exciton absorption band also shows a strong blue shift of ~ 180 meV with decreasing number of layers that is consistent with the disappearance of the Raman modes. The photocurrent signal was also shown to decay gradually with increasing wavelength, suggesting that a few layers InSe has an indirect band gap. Furthermore, the realization of ultrathin (< 10 layers) photodetectors with a relatively high photoresponsivity (12.3 AW^{-1} at $\lambda = 450$ nm and $T = 300$ K)³³ and fast response ($488\text{ }\mu\text{s}$) has been reported.³²

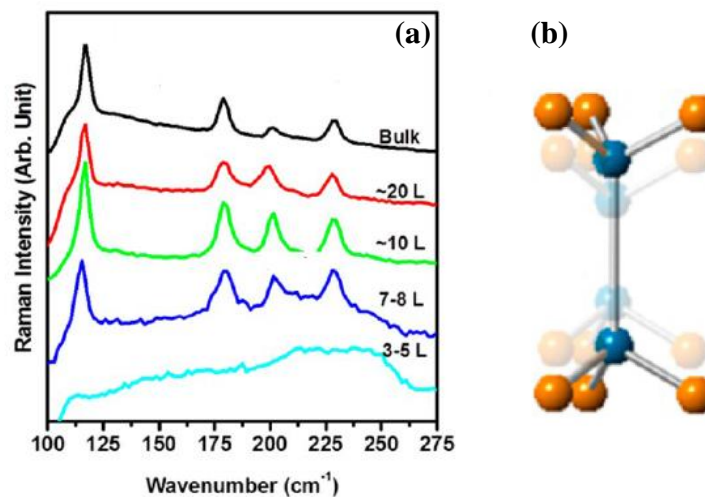


Figure 2.11: Raman studies of mechanically exfoliated γ -InSe flakes. (a) Thickness dependent resonant Raman spectra of InSe flakes with a 514 nm argon laser. (b) The sketch of non-polar phonon mode corresponds to the main Raman peak at 117 cm^{-1} . Picture reproduced from Ref [32].

High performance (I_{ON}/I_{OFF} ratio $\sim 10^8$) multilayer InSe transistors on poly-methyl methacrylate (PMMA)/ Al_2O_3 dielectric were fabricated and demonstrated by W. Feng et al.,⁹⁷ see Figure 2.12a. (PMMA)/ Al_2O_3 dielectric was used to increase the mobility of InSe through the suppression of Coulomb impurity scattering or surface polar phonon scattering. Figures 2.12b and 2.12c show the output and transfer characteristics of multilayer InSe FETs at room temperature. A typical n -type conductance and a saturation regime at high V_{ds} were observed. The I_{ds} - V_{ds} characteristics showed a linear regime at low V_{ds} and a saturation current regime at high V_{ds} . At high V_{ds} the conducting channel is under the *pinch-off* condition, thus causing a saturation in the drain current.⁹⁷

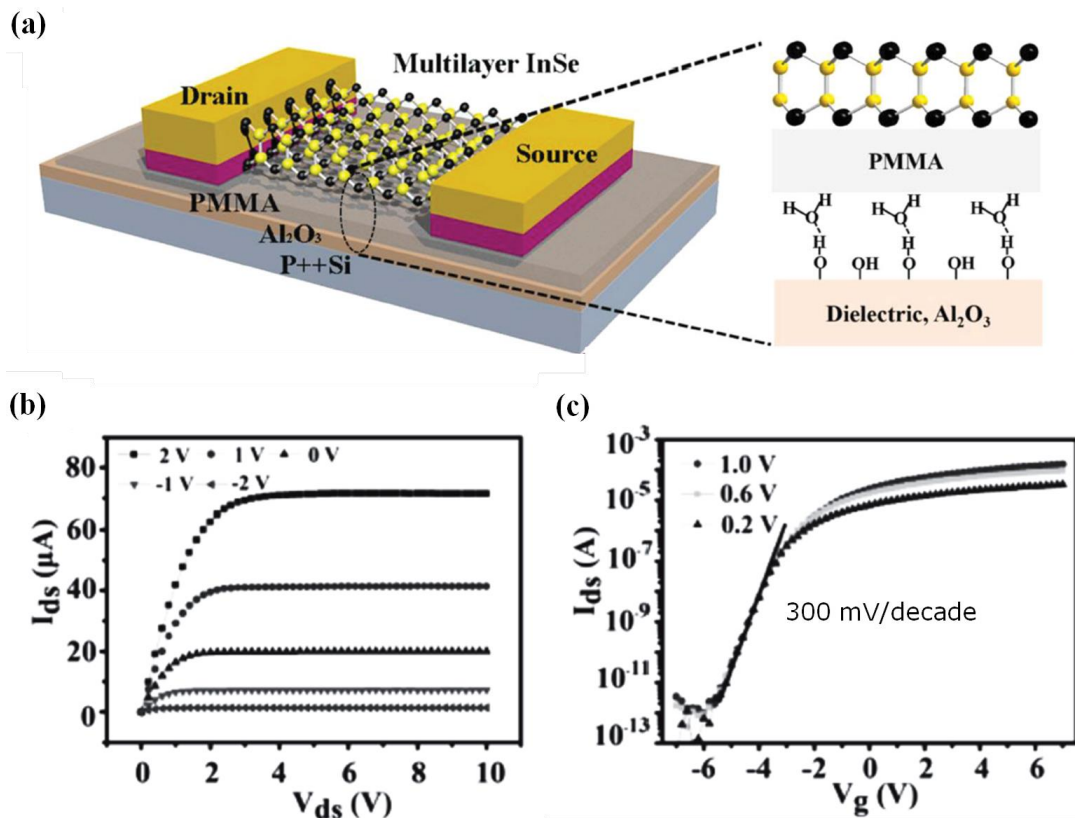


Figure 2.12: (a) Schematic of back-gate multilayer InSe FETs consisting of PMMA/ Al_2O_3 back-gate insulator and Au/Cr electrodes. (b) Output characteristics of FETs at various gate voltages, V_g . (c) Transfer characteristics of FETs at various V_{ds} . Picture reproduced from Ref [97].

2.2.1.2 Hexagonal ϵ -GaSe

The primitive unit cells of ϵ -GaSe contain two layers, each consisting of four closely-packed, covalently bonded monoatomic sheets in the sequence Se-Ga-Ga-Se. Along the c -axis, the primitive unit cell of ϵ -GaSe has a lattice parameter of $c = 15.949 \text{ \AA}$ ⁹³ and the distance between two neighboring layers is 8 \AA .⁹⁸ Within each a - b plane, atoms form hexagons with lattice parameter $a = 3.755 \text{ \AA}$. The bulk GaSe has a direct band gap of $E_g = 2.02 \text{ eV}$ at $T = 300 \text{ K}$.^{93, 98} It is usually a p -type semiconductor.⁹² Its anisotropic electronic properties are reported in Table 2.2.

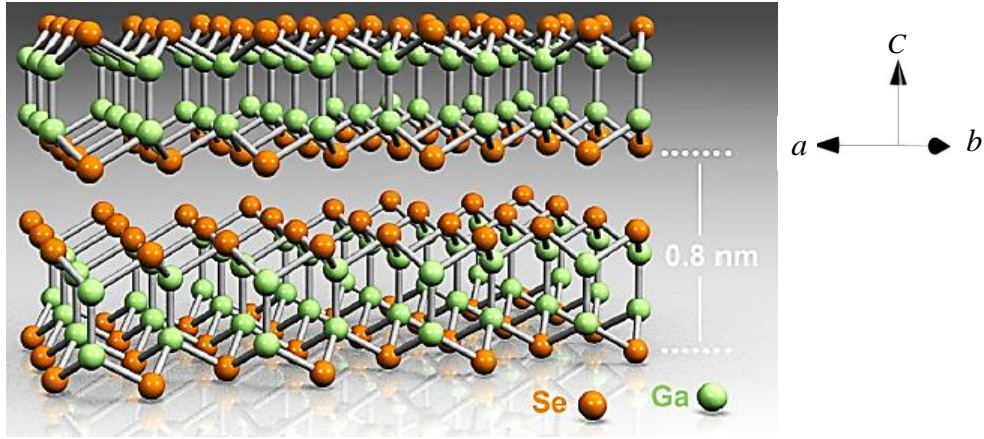


Figure 2.12: Schematic diagram of the crystal structure of layered GaSe. Two layers of GaSe are displayed where the Se and Ga atoms are represented by orange and green spheres, respectively. The distance between two layers along the c -axis is 8 \AA . Picture reproduced from Ref [99].

Table 2.2: Electron (m_e^*), hole (m_h^*) and exciton (μ) effective masses, and static and dynamic dielectric permittivities along the c -axis and in the layer plane of ϵ -GaSe. Table produced from Ref [93, 100].

	m_e^*	m_h^*	μ	ϵ_∞	ϵ_0
$\parallel c$	$1.6 m_0$	$0.2 m_0$	$0.178 m_0$	5.76	5.76
$\perp c$	$0.5 m_0$	$0.8 m_0$	$0.308 m_0$	7.44	10.6

The layer thickness dependent PL studies show a blue shift of 20 meV between bulk and bilayer GaSe,²³ which is smaller than for InSe. The Raman study reveals the relationship between the number of GaSe layers and the Raman spectra (Figure 2.13).⁹⁹ Three Raman peaks were observed in all samples at 59 cm⁻¹, 132 cm⁻¹ and 305 cm⁻¹. The relative intensity of the peaks at 59 cm⁻¹ and 132 cm⁻¹ (E_{1g}^1 and A_{1g} modes, respectively) decreases with the number of layers. The Raman peak at 305 cm⁻¹ shows a red shift with decreasing layer number, which corresponds to a reduction of the force constant in the atomic layers as the sample becomes thinner.⁹⁹

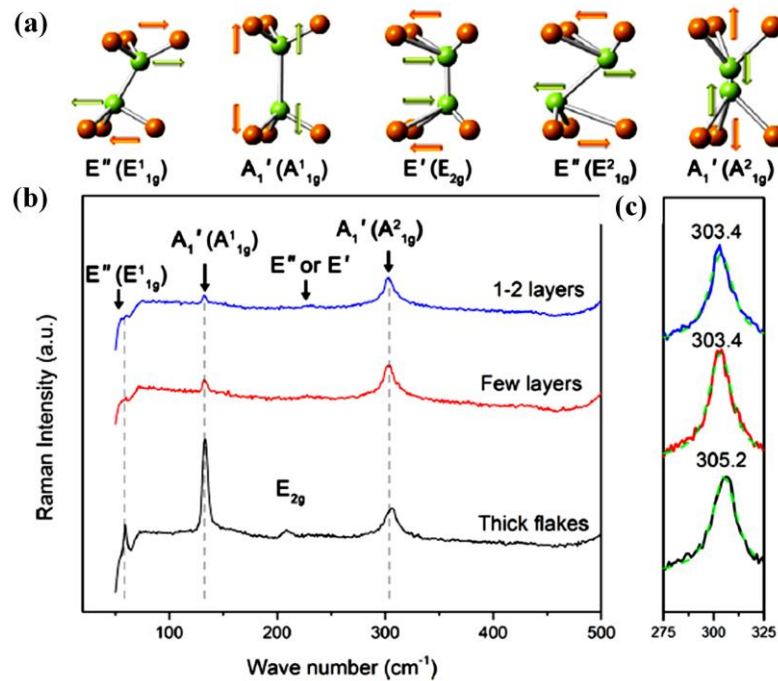


Figure 2.13: Raman spectra of layered GaSe with various thickness. (a) Schematics of the Raman modes of GaSe. The colored arrows indicate the vibrational directions of Se (orange) and Ga (green) atoms. (b) Thickness dependence normalized Raman spectra. With decreasing number of layers, the intensities of E_{1g}^1 mode at 59 cm⁻¹ and A_{1g} mode at 132 cm⁻¹ decrease, the E_{2g} mode at 208 cm⁻¹ diminishes, and a weak peak at 230 cm⁻¹ appears. (c) The A_{1g} peak at 305.2 cm⁻¹ shifts to 303.4 cm⁻¹ with reducing layer thickness. Picture reproduced from Ref [99].

Ultrathin GaSe based photodetectors were fabricated by P. Hu et al.,²³ see Figure 2.14a. The influence of wavelength on the photoresponse was investigated

(Figure 2.14b-c). Figure 2.14b shows the I - V curves of a GaSe photodetector under dark and illumination with different photon wavelengths. Figure 2.14c shows the wavelength dependent photocurrent (PC) at $V_{ds} = 5$ V, which is calculated from Figure 2.14b. The PC increases with decreasing wavelength from $\lambda = 610$ nm to 254 nm. This indicates that 2D GaSe based photodetectors are highly sensitive to UV – visible light. On and off light irradiation at $\lambda = 254$ nm gives an on/off switching current ratio of ~ 8 (Figure 2.14d).

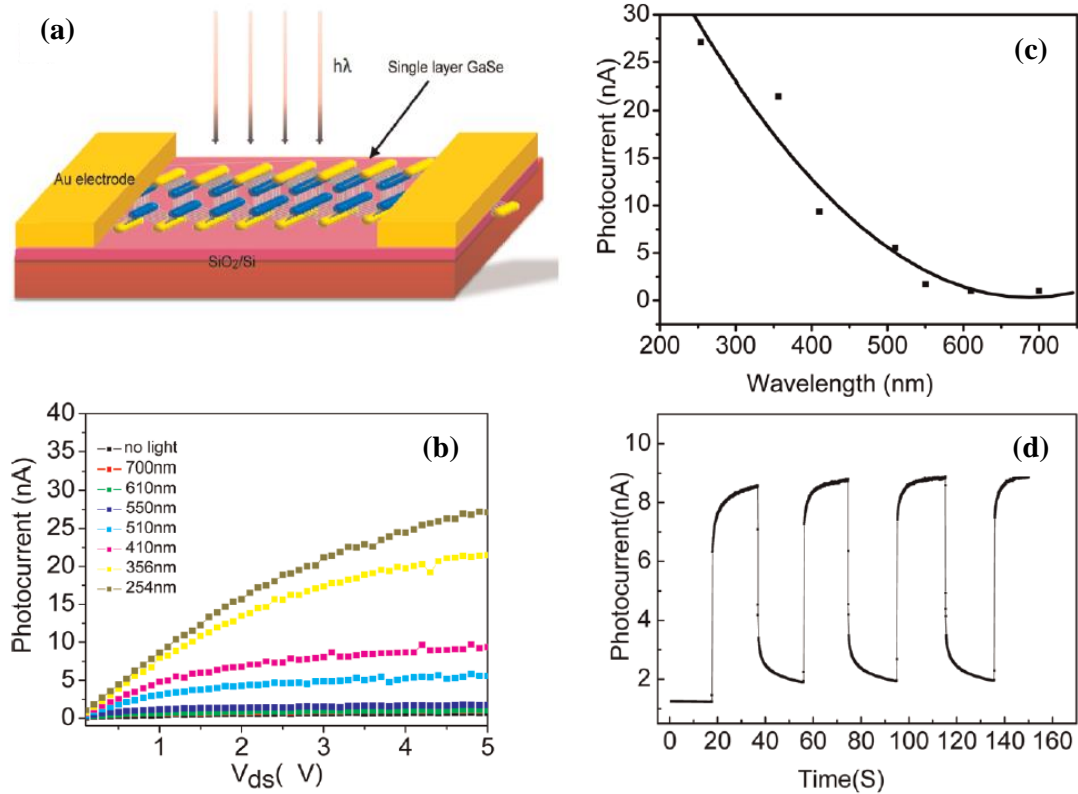


Figure 2.14: Characterization of a few-layer GaSe photodetector: (a) schematic drawing of the GaSe photodetector; (b) I - V curves of the photodetector for different photon wavelengths; (c) wavelength dependent photocurrent; (d) photocurrent as a function of time at a bias voltage of 1 V. Picture reproduced from Ref [23].

Recently, 2D single-sheet GaSe based FETs have been fabricated and demonstrated.³¹ Figure 2.15a shows an optical image of a single sheet of GaSe

deposited on a SiO₂/Si substrate using mechanical exfoliation. An optical image of electron-beam patterned electrodes on a GaSe single-sheet is shown in Figure 2.15b. The room temperature FET output characteristic (I_{ds} - V_{ds}) and transfer characteristics (I_{ds} - V_{gs}) are shown in Figure 2.15c-d.

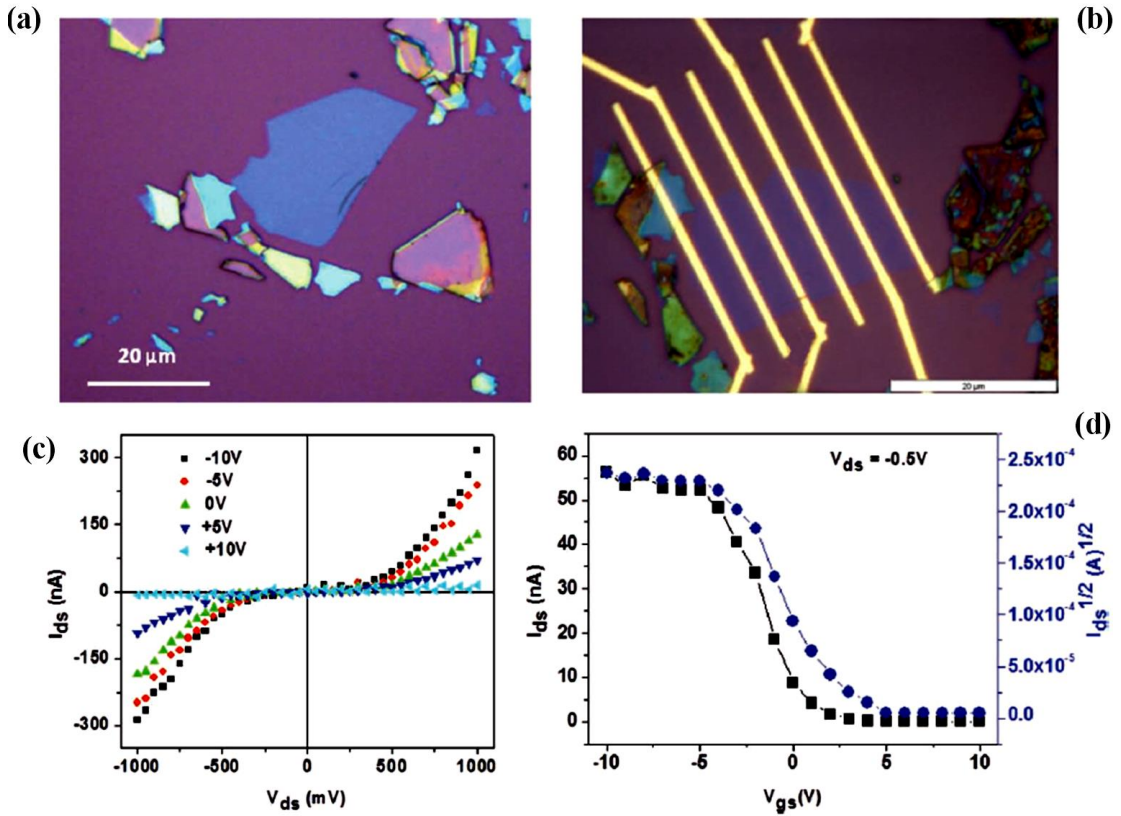


Figure 2.15: Single-sheet GaSe: (a) Typical optical image before patterning electrode and (b) optical image after patterning electrode. (c) Room-temperature FET output characteristics of single-sheet of GaSe in dark at constant humidity (22 %) and (d) transfer characteristics of a GaSe single sheet FET. Picture reproduced from Ref [31].

Chapter 3

Semiconductor devices

This chapter describes the basic principles of semiconductor devices studied during my PhD. This project explores numerous new concepts in semiconductor physics, which are underpinned by physical effects described in this chapter and that include tunneling, and carrier recombination in p - n junctions based on 2D van der Waals crystals, p - i - n diodes based on Ga(AsN)/AlAs superlattice, and GaAs/AlAs resonant tunneling diodes.

3.1 p - n junction

The p - n junction is a key building block for most semiconductor devices. This is formed between a p -type (with positively charged carriers) and an n -type (with negatively charged carriers) semiconductor. It is used widely in rectification, switching, amplification, etc. There are two types of p - n junctions: (i) the homojunction, made of one semiconductor and (ii) the heterojunction, made of different semiconductors.

Figure 3.1a shows two semiconductors with uniformly p - and n -type doping. The p -type material contains a concentration N_A^- of negatively charged acceptors and density of free holes $p = N_A^-$. The n -type material contains a concentration N_D^+ of positively charged donors and density of free electron $n = N_D^+$. Therefore, the Fermi level E_F is near the valence band edge in the p -type material and near the conduction band in the n -type material. When these two semiconductors come close together, the carrier concentration gradient at the junction causes carrier diffusion.¹⁰¹ As the free carriers move through the junction, they leave behind ionized acceptors (N_A^-) and

donors (N_D^+) on each side of the junction. This space charge creates an electric field, \mathcal{E} , and induces a drift current opposite to the diffusion current (see Figure 3.1b). Therefore a state of equilibrium occurs leading to a *potential difference*, V_{bi} , across the junction as the negatively charged acceptors repel the electrons and the positively charged donors repel the holes. At equilibrium the net current is zero and the Fermi level is constant across the sample. The regions on either sides of the junction become completely depleted of free carriers in comparison to the p - and n -type materials further away from the junction. This area around the p - n junction is called the “depletion region”.

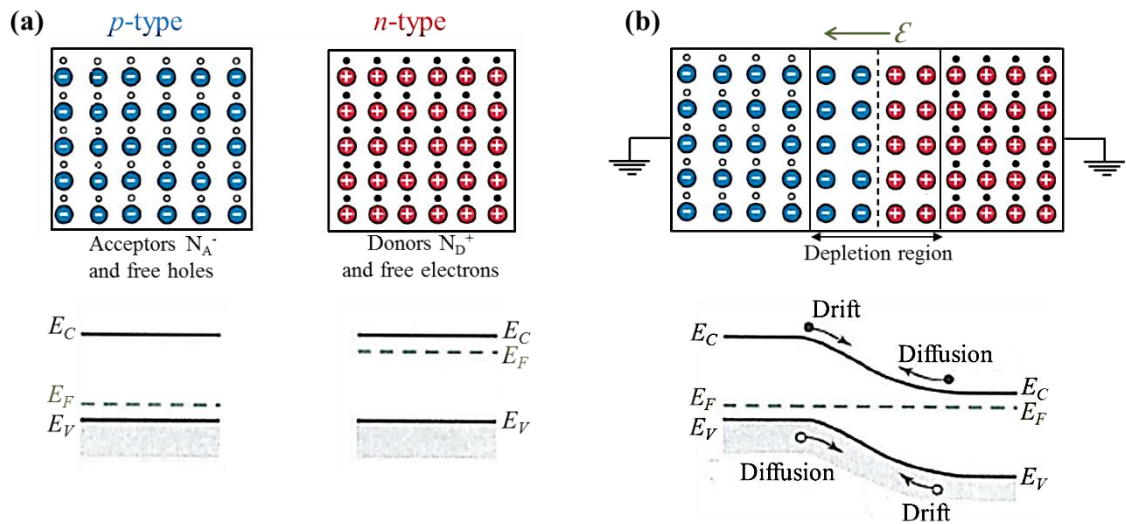


Figure 3.1: (a) Uniformly doped p - and n -type semiconductors before the junction is formed. (b) The electric field in the region and the energy band diagram of a p - n junction in thermal equilibrium.

When we apply a positive voltage on the p -side, the junction becomes forward biased. Majority carriers, electrons and holes, are attracted towards the junction and the depletion region becomes narrower. Electrons are injected into the p -side and holes are injected into the n -side, thus resulting into a large forward current (see Figure 3.2). When we apply a negative voltage on the p -side, the junction becomes

reverse biased. Majority carriers move far away from the junction thus broadening the depletion region. Fewer electrons are injected into the p -side and fewer holes are injected into the n -side thus resulting into a small reverse current.

The rectifying behavior of a p - n junction is the most important characteristic, i.e. the current easily flows only in one direction. The current-voltage (I - V) characteristic of a typical p - n junction is shown in Figure 3.2. At the forward bias condition, the current increases rapidly with increasing applied bias and at the reverse bias, virtually no current flows till a critical voltage is reached, at which point the current suddenly increases. This sudden increase in current is referred to as the junction breakdown. The breakdown mechanisms are the tunneling effect and avalanche multiplication, both occurring under a large applied electric field. A valence electron can make a transition from the valence band to the conduction band by penetrating through the energy gap. This effect is referred as tunneling. Also an electron can gain sufficient kinetic energy to break a bond thus creating an electron-hole pair. The newly created electron-hole pairs both acquire kinetic energy from the electric field and create additional pairs. This process is therefore called avalanche multiplication.¹⁰¹

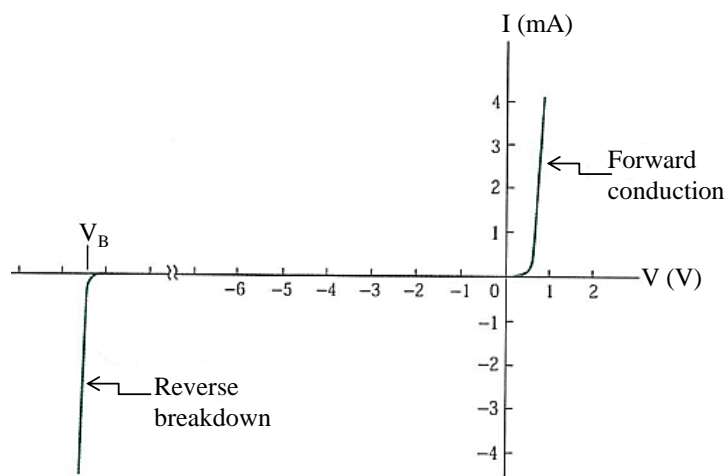


Figure 3.2: Current-voltage characteristics of a typical p - n junction. Picture reproduced from Ref [101].

A voltage applied to a p - n junction disturbs the precise balance between the diffusion current and drift current of electrons and holes. Following S. Sze et al.,¹⁰¹ the current-voltage characteristics of an ideal diode can be derived based on the following assumptions: (i) the depletion region has abrupt boundaries and the semiconductor is assumed to be neutral outside the boundaries; (ii) the carrier densities at the boundaries are related by the electrostatic potential difference across the junction; (iii) the low injection condition, i.e. the injected minority carrier densities are small compared to the majority carrier densities; (iv) neither generation nor recombination current exists in the depletion region and the electron and hole currents are constant throughout the depletion region.

At thermal equilibrium, the majority carrier density in the neutral region is equal to the doping concentration. Let's take n_{n0} and n_{p0} as the equilibrium electron densities in the n - and p -type regions, respectively. The built in potential V_{bi} can be written as

$$V_{bi} = \frac{kT}{q} \ln \frac{p_{p0}n_{n0}}{n_i^2} = \frac{kT}{q} \ln \frac{n_{n0}}{n_{p0}}, \quad (3.1)$$

where $q = -e$ is the electron charge, n_i is the intrinsic carrier density, and $p_{p0}n_{n0} = n_i^2$ is the mass action law. Rearranging Eq. 3.1 gives

$$n_{n0} = n_{p0} \exp\left(\frac{qV_{bi}}{kT}\right). \quad (3.2)$$

Similarly, we have

$$p_{p0} = p_{n0} \exp\left(\frac{qV_{bi}}{kT}\right). \quad (3.3)$$

One can note that the electron and hole densities at the boundaries of the depletion region are related by the electrostatic potential difference V_{bi} at thermal equilibrium. Under an applied forward bias, $V = V_F > 0$, the electrostatic potential difference is

reduced to $V_{bi} - V_F$. Under a reverse bias, $V = -V_R < 0$, the electrostatic potential difference is increased to $V_{bi} + V_R$ (see Figure 3.3). Therefore, Eq. 3.2 is modified to

$$n_n = n_p \exp \left[\frac{q(V_{bi} - V)}{kT} \right], \quad (3.4)$$

where n_n and n_p are the non-equilibrium electron densities at the boundaries of the depletion region in the n - and p -sides, respectively, with V positive for forward bias and negative for reverse bias.

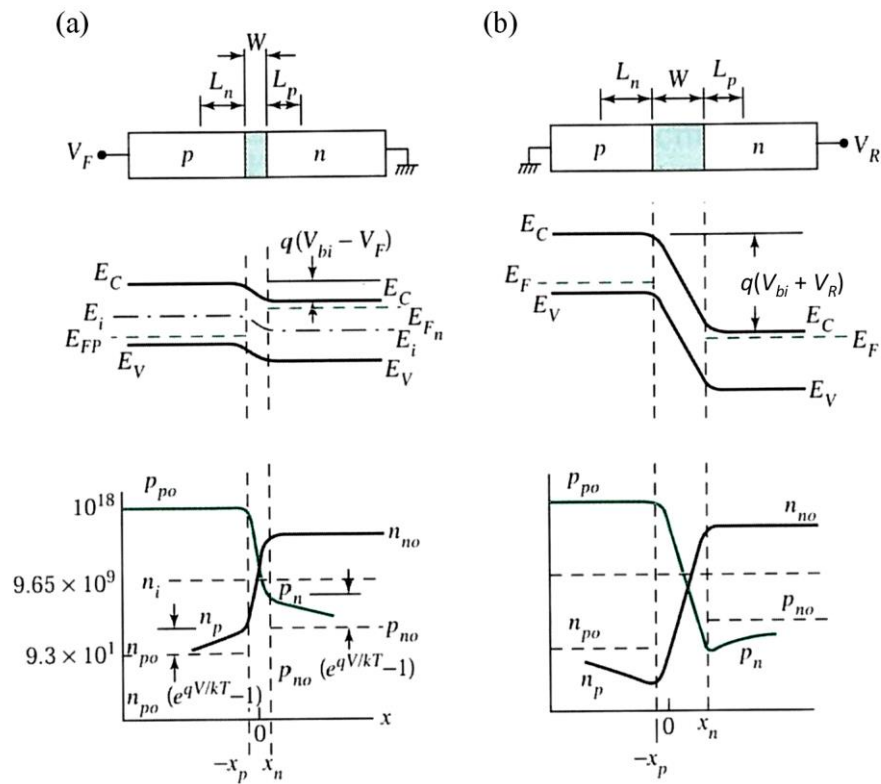


Figure 3.3: Depletion region, energy band diagram and carrier distribution for a p - n junction under (a) a forward bias and (b) a reverse bias. Under forward bias, the minority carrier densities at the boundaries ($-x_p$ and x_n) increase significantly above their equilibrium values, and under the reverse bias they decrease below their equilibrium. Equations 3.5 and 3.6 define the minority carrier densities at the depletion layer boundaries. The slopes of the carrier distributions decrease with the forward bias within the depletion region. This comes from the fast sweep of the carriers across the narrower depletion region. Picture reproduced from Ref [101].

According to assumption (iii), the injected minority carrier density is much smaller than the majority carrier density. Thus we can write $n_n \cong n_{n0}$. Substituting this condition and Eq. 3.2 into Eq. 3.4 yields the electron density at the boundary of the depletion region on the p -side ($x = -x_p$):

$$n_p - n_{p0} = n_{p0} \left[\exp\left(\frac{qV}{kT}\right) - 1 \right]. \quad (3.5)$$

Similarly, at $x = x_n$ for the n -type boundary we have

$$p_n - p_{n0} = p_{n0} \left[\exp\left(\frac{qV}{kT}\right) - 1 \right]. \quad (3.6)$$

According to the assumption (iv), all current comes from the neutral regions. There is no electric field in the neutral n -region, thus reducing the steady state continuity equation ($J_n = J_n(\text{drift}) + J_n(\text{diffusion}) = 0$) to

$$\frac{d^2 p_n}{dx^2} - \frac{p_n - p_{n0}}{D_p \tau_p} = 0. \quad (3.7)$$

where D_p is the hole diffusion constant and τ_p is the hole lifetime. When we apply the boundary conditions of Eq. 3.6 and $p_n(x = \infty) = p_{n0}$ to the solution of Eq. 3.7, we obtain

$$p_n - p_{n0} = p_{n0} \left[\exp\left(\frac{qV}{kT}\right) - 1 \right] \exp\left(-\frac{(x - x_n)}{L_p}\right), \quad (3.8)$$

where $L_p = \sqrt{D_p \tau_p}$ is the diffusion length of holes in the n -region. At $x = x_n$,

$$J_p(x_n) = -qD_p \left. \frac{dp_n}{dx} \right|_{x_n} = \frac{qD_p p_{n0}}{L_p} \left[\exp\left(\frac{qV}{kT}\right) - 1 \right]. \quad (3.9)$$

Similarly, for the neutral p -region

$$n_p - n_{p0} = n_{p0} \left[\exp\left(\frac{qV}{kT}\right) - 1 \right] \exp\left(\frac{(x + x_n)}{L_n}\right), \quad (3.10)$$

and

$$J_n(-x_p) = qD_n \left. \frac{dn_p}{dx} \right|_{-x_p} = \frac{qD_n n_{p0}}{L_n} \left[\exp\left(\frac{qV}{kT}\right) - 1 \right], \quad (3.11)$$

where $L_n = \sqrt{D_n \tau_n}$ is the diffusion length of electrons. The total current is constant across the device and is the sum of Eqs. 3.9 and 3.11:

$$J = J_p(x_n) + J_n(-x_p) = J_s \left[\exp\left[\frac{qV}{kT}\right] - 1 \right]. \quad (3.12)$$

where

$$J_s = \frac{qD_p p_{n0}}{L_p} + \frac{qD_n n_{p0}}{L_n}, \quad (3.13)$$

is the saturation current density. Equation 3.12 is the *ideal diode equation*. Figure 3.4 shows the ideal current-voltage characteristic.

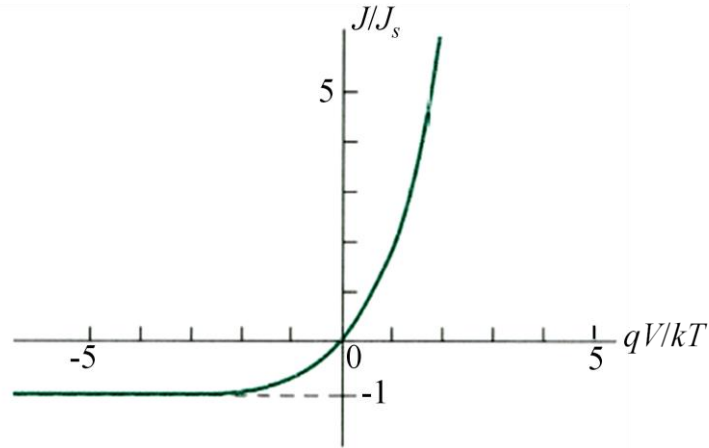


Figure 3.4: Ideal current-voltage characteristics. In forward bias, the current increases with applied voltage. In reverse bias, the current density saturates at $-J_s$. Picture reproduced from Ref [101].

The homojunction and heterojunction devices formed from combinations of n -InSe, p -InSe, p -GaSe, and n -In₂O₃ semiconductors using mechanical exfoliation of Bridgman-grown crystals and a simple mechanical contact method or thermal annealing show rectification behavior with low leakage current densities in reverse bias. The I - V curves differ from the ideal diode equation because of the generation-recombination of carriers in the depletion region.

The concentrations of both electrons and holes in the depletion region exceed their equilibrium values under forward bias, see Figure 3.3a. The carriers tend to return to their equilibrium values by recombination. However, under reverse bias carrier concentrations in the depletion region fall far below their equilibrium value (see Figure 3.3b). Therefore, electrons and holes tend to emit through band gap generation-recombination centers. The experimental results can be represented empirically by

$$J \approx \exp\left(\frac{qV}{\eta kT}\right), \quad 3.14$$

where the factor η is called the ideality factor. When the ideal diffusion current dominates $\eta = 1$. When the recombination current dominates $\eta = 2$. η takes a value between 1 and 2 when the diffusion and generation-recombination currents are comparable. In general, at low forward voltage the recombination current dominates and $\eta = 2$. At high applied voltage, the diffusion current tends to dominate and η approaches 1. At even higher voltages, the current departs from the ideal situation ($\eta = 1$) and increases more gradually with forward voltage due to high injection and series resistance effects.

The diffusion and the generation-recombination currents are strongly dependent on temperature. At a given forward bias the diffusion current increases more rapidly than the recombination current with increasing temperature. Therefore, the diode follows the ideal equation over a wide range of forward bias at high temperatures ($T > 300$ K). Under reverse bias, the diffusion current eventually dominates with increasing temperature.

3.2 *p-i-n* diode

The *p-i-n* diode has an intrinsic (*i*) region sandwiched between heavily doped *p*- and *n*-type semiconductors. In practice, the idealized *i*-region is approximated by either a high-resistivity *p*-layer or a high-resistivity *n*-layer.¹⁰² The *p-i-n* diode has two characteristics: (i) the device resistance varies approximately linearly with increasing forward bias; (ii) the diode capacitance is constant under reverse bias.¹⁰³ It has wide applications: in attenuator applications where resistance is required to be controlled by the current; as dc controlled microwave switch; as a modulating device due to its variable forward resistance characteristics; as photodetectors in fiber optic systems; as light emitting diodes (LEDs).¹⁰³

Under forward bias, holes from the *p*-type region and electrons from the *n*-type region are injected into the *i*-region. If we assume that the carrier concentration across the *i*-region is approximately constant, the diffusion current can be neglected. As the injected carrier density is much higher than the doping concentration of *i*-region, the *p-i-n* diode is generally operated in the high-injected condition, $n_n \approx p_p \gg n_i$. When the period of the varying applied signal is longer than the carrier lifetime in *i*-region, the diode follows the ideal *p-n* diode equation.

In a *p-i-n* diode, the depletion region exists almost completely within the *i*-region. This depletion region is much larger than in a *p-n* diode, and almost constant-size, independent of the reverse bias voltage. This increases the volume where electron-hole pairs can be generated by an incident photon. In my PhD project, I have studied the transport properties of *p-i-n* diodes based on GaAs/AlAs double barrier quantum wells (resonant tunneling diodes) and Ga(AsN)/AlAs superlattices. The properties of these structures are described in section 3.2.1 and 3.2.2, respectively.

3.2.1 Resonant tunneling diode

The resonant tunnelling diode (RTD) is a heterostructure device with potential applications in high speed electronics.¹⁰⁴ Typically, a RTD consists of an undoped quantum well (QW) layer sandwiched between undoped barrier layers and heavily doped emitter and collector contact regions. Classically, a particle encountering a potential barrier requires an energy greater than the height of the potential barrier, $E > V$, in order to be transmitted. For an object behaving quantum mechanically, with $E < V$, there is a finite probability that it may tunnel through the barrier. The tunnelling probability decreases exponentially with increasing barrier height and thickness, and with decreasing the incident energy.

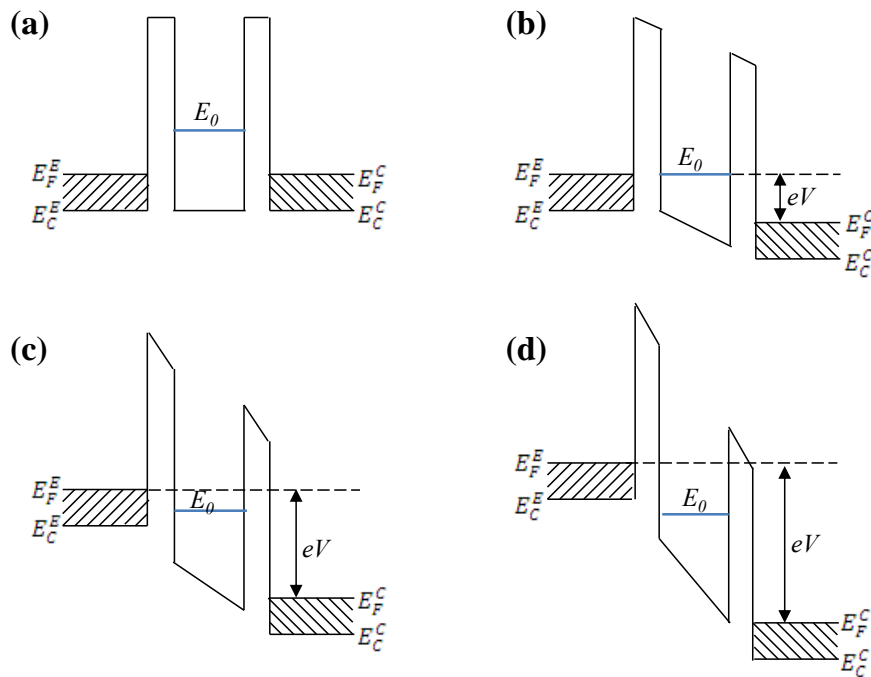


Figure 3.5: Conduction band profiles of a n - i - n RTD at four different applied biases: (a) zero bias, (b) threshold bias, (c) resonance, and (d) off-resonance. Hatched regions represent the Fermi sea in the n -type regions. E_F^E and E_F^C are the local Fermi energies in the emitter and the collector regions and eV is the difference between them. E_C^E and E_C^C are the energies of the conduction band edges in the emitter and collector. Figure reproduced from Ref [104].

Figure 3.5 shows the conduction band diagram for a *n-i-n* RTD based on an (AlGa)As/GaAs/(AlGa)As double barrier QW under an applied bias. The resonant tunneling of electrons occurs when the Fermi energy of the electrons in the emitter aligns with the quasi-bound states of electrons in the QW (E_0 is the lowest state, see Figure 3.5a). Figure 3.5b-d shows the effect of the external bias, V , on the alignment of the emitter and the quasi-bound state. A resonant current starts to flow when E_0 reaches the quasi-Fermi level, E_F^E , (Figure 3.5b) and reaches its maximum when E_0 passes through the Fermi sea in the emitter (Figure 3.5c). Figure 3.5d shows the off-resonance state when E_0 falls below the conduction band edge in the emitter.

We first consider tunneling from a 3D emitter layer into the band state of a QW. As shown in Figure 3.6a, the electrons have a plane-wave like motion only in the QW plane (i.e. along y and z). Because of energy and momentum conservation, the electronic states involved in the tunneling can be represented by the intersection of the plane $k_z = q_R$ with the Fermi sphere, where q_R is the wavenumber associated with the energy of the resonant state with respect to the conduction band edge, i.e.

$$q_R = \frac{\sqrt{2m^*(E_0 - E_C^E)}}{\hbar}. \quad (3.15)$$

The tunneling current density J is proportional to the density of states indicated by the 2D grey disk in Figure 3.6a and can be written as

$$J \propto \pi(k_F^2 - q_R^2) \propto (E_F^E - E_0). \quad (3.16)$$

As $E_F^E - E_0$ is proportional to the applied bias, J increases linearly until E_0 falls below the conduction band edge in the emitter. A triangular shaped J - V characteristic is obtained as shown in Figure 3.6 (c).

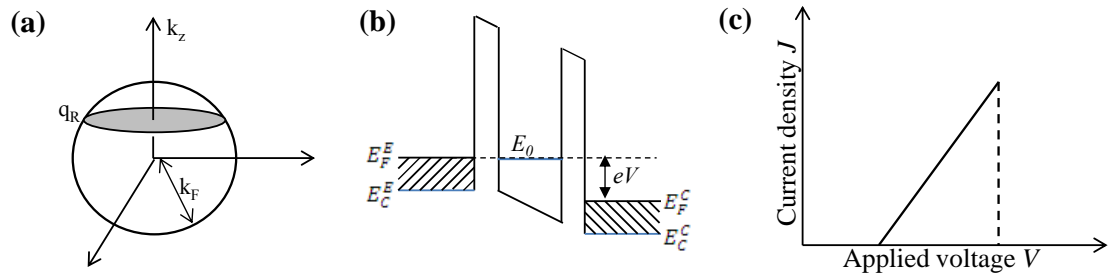


Figure 3.6: (a) A Fermi sphere of electrons in the emitter. The grey disk represents those states which meet the selection criterion to enter the QW. (b) Energy band diagram and (c) sketch of the J - V characteristics. Figure reproduced from Ref [104].

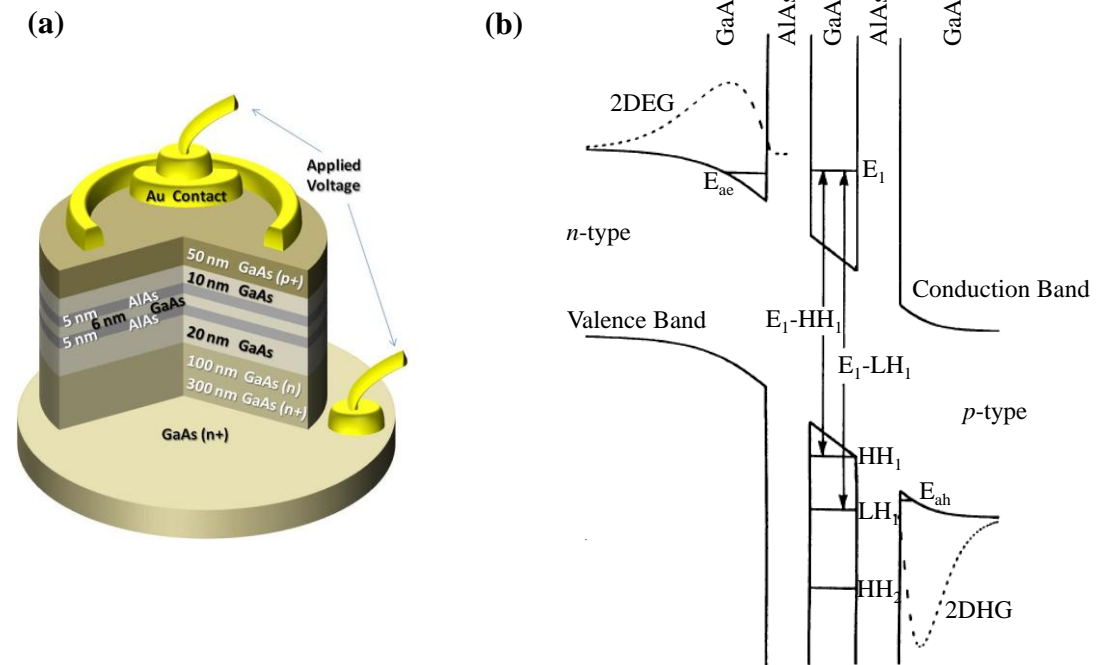


Figure 3.7: (a) Sketch of a p - i - n RTD with an AlAs/GaAs/AlAs QW double barrier. (b) Schematic band diagram of our device in forward bias (above the flat band condition). Quasi-two dimensional electron and hole accumulation layers form in the GaAs spacer layers on the n - and p -type sides of the two AlAs barriers with bound states energies E_{ae} and E_{ah} . As the voltage is increased, both electrons and holes can resonantly tunnel from the accumulation layers into the bound states of the QW (E_n , HH_n , and LH_n , where $n = 1, 2$).

Our RTD device is based on a p - i - n diode with an undoped AlAs/GaAs/AlAs double barrier QW (see Figure 3.7a). The undoped GaAs spacer layer between the

barrier and the n -doped (p -doped) GaAs layer allows a 2D electron (hole) gas to accumulate against the barriers in a triangular potential well formed under the applied bias (see Figure 3.7b). The tunneling of electrons (holes) now takes place from the accumulation layers into the QW quasi-bound states for electrons, E_n , and holes (light holes, LH_n , and heavy holes, HH_n), where $n = 1, 2$.¹⁰⁵

3.2.2 Superlattice

A superlattice (SL) consists of alternating thin (1 – 10 nm) layers of two or more different semiconductor materials.¹⁰⁶ The size of the SL unit cell is generally greater than the lattice constant of the host crystal thus reducing the boundary of the Brillouin zone and resulting in the formation of minizones and a series of energy minibands and minigaps. The band structure of the SL is dictated by the design of the SL unit cell. The extent of the Brillouin zone is given by $2\pi/(a+b)$, where a and b are the well width and barrier thickness, respectively (see Figure 3.8). The position and thickness of the energy band is influenced by the well width, barrier thickness, and the height of the barrier potential, U_b . The width and height of the barriers affects the coupling between states in adjacent wells.

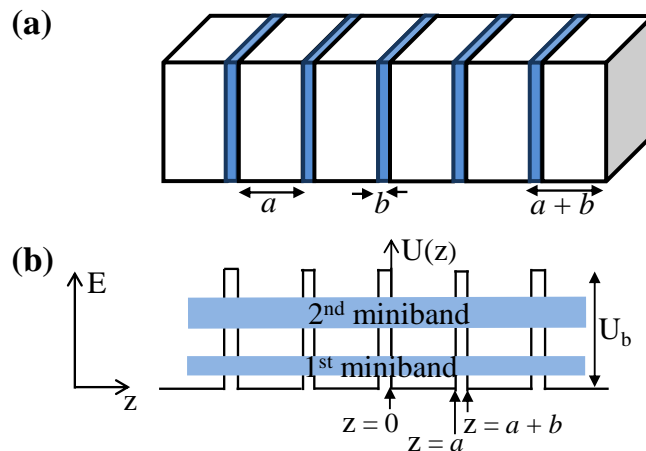


Figure 3.8: (a) Superlattice layer structure. (b) Sketch of the potential profile and energy minibands of a semiconductor superlattice.

The SL dispersion can be calculated using the Kronig-Penney model,¹⁰⁷ which is described in the following section.

3.2.2.1 Kronig-Penney model

Here we describe the electronic bound states of a Ga(AsN)/AlAs SL using the Kronig-Penney model. This model considers an electron in a periodic rectangular potential and an infinite periodic potential such that $U(z) = U(z + a + b)$, where $a + b$ is the SL period, see Figure 3.9.

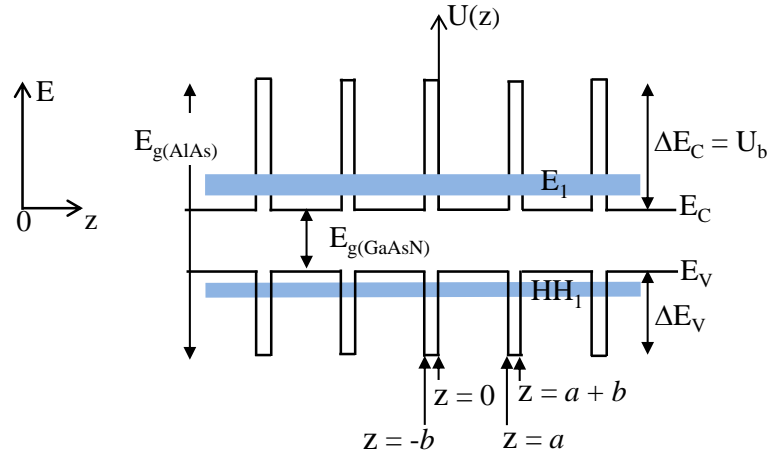


Figure 3.9: Schematic of the potential profile and energy minibands of a GaAsN/AlAs superlattice, where $\Delta E_C = [E_g(\text{AlAs}) - E_g(\text{GaAs}_{1-x}\text{N}_x)] \times 0.6$ and $\Delta E_V = [E_g(\text{AlAs}) - E_g(\text{GaAs}_{1-x}\text{N}_x)] \times 0.4$.¹⁰⁸

The barrier height of the CB is $U_b = [E_g(\text{AlAs}) - E_g(\text{GaAs}_{1-x}\text{N}_x)] \times 0.6$, where E_g is the band gap energy. Note that the barrier height U_b depends on the nitrogen content, x . The time-independent Schrödinger equation can be written as

$$-\frac{\hbar^2}{2m^*} \frac{d^2}{dz^2} \psi(z) + U(z)\psi(z) = E\psi(z), \quad (3.17)$$

where E is the energy eigenvalue and m^* is the electron effective mass.

In the region $0 < z < a$, where $U = 0$, the electron eigenfunction is a linear combination of plane waves travelling to the right and to the left

$$\psi(z) = Ae^{iKz} + Be^{-iKz}, \quad (3.18)$$

where A and B are constants. The corresponding energy is

$$E = \frac{\hbar^2 K^2}{2m_w^*}, \quad (3.19)$$

where m_w^* is the electron effective mass inside the well.

In the region $-b < z < 0$, within the barrier, we can write

$$\psi(z) = C e^{Qz} + D e^{-Qz}, \quad (B.20)$$

with

$$U_b - E = \frac{\hbar^2 Q^2}{2m_b^*}, \quad \text{for } E < U_b, \quad (B.21)$$

where m_b^* is the electron effective mass inside the barrier, and C and D are constants.

Using the boundary conditions at $z = 0$, we obtain

$$A + B = C + D \quad (3.22)$$

$$\frac{iK}{m_w^*} (A - B) = \frac{Q}{m_b^*} (C - D). \quad (3.23)$$

The Bloch theorem gives

$$\psi(z = a) = \psi(z = -b)e^{ik(a+b)}. \quad (3.24)$$

Using the boundary conditions at $z = a$ and the Bloch theorem, we obtain

$$Ae^{iKa} + Be^{-iKa} = (C e^{-Qb} + D e^{Qb})e^{ik(a+b)} \quad (3.25)$$

$$\frac{iK}{m_w^*} (Ae^{iKa} - Be^{-iKa}) = \frac{Q}{m_b^*} (C e^{-Qb} - D e^{Qb}) e^{ik(a+b)}. \quad (3.26)$$

We can write the four equations (Eqs. 3.22, 3.23, 3.25, and 3.26) in matrix format as

$$\begin{bmatrix} 1 & 1 & -1 & -1 \\ \frac{iK}{m_w^*} & -\frac{iK}{m_w^*} & -\frac{Q}{m_b^*} & \frac{Q}{m_b^*} \\ e^{iKa} & e^{-iKa} & -e^{-Qb}e^{ik(a+b)} & -e^{Qb}e^{ik(a+b)} \\ \frac{iK}{m_w^*}e^{iKa} & -\frac{iK}{m_w^*}e^{-iKa} & -\frac{Q}{m_b^*}e^{-Qb}e^{ik(a+b)} & \frac{Q}{m_b^*}e^{Qb}e^{ik(a+b)} \end{bmatrix} \begin{bmatrix} A \\ B \\ C \\ D \end{bmatrix} = \begin{bmatrix} 0 \\ 0 \\ 0 \\ 0 \end{bmatrix} \quad (3.27)$$

For a nontrivial solution, the determinant of the matrix must be zero, i.e.,

$$\begin{vmatrix} 1 & 1 & -1 & -1 \\ \frac{iK}{m_w^*} & -\frac{iK}{m_w^*} & -\frac{Q}{m_b^*} & \frac{Q}{m_b^*} \\ e^{iKa} & e^{-iKa} & -e^{-Qb}e^{ik(a+b)} & -e^{Qb}e^{ik(a+b)} \\ \frac{iK}{m_w^*}e^{iKa} & -\frac{iK}{m_w^*}e^{-iKa} & -\frac{Q}{m_b^*}e^{-Qb}e^{ik(a+b)} & \frac{Q}{m_b^*}e^{Qb}e^{ik(a+b)} \end{vmatrix} = 0 \quad (3.28)$$

Expanding Eq. 3.28 and collecting the terms with $\left(\frac{K}{m_w^*}\right)^2$, $\left(\frac{Q}{m_b^*}\right)^2$, and $\frac{KQ}{m_w^*m_b^*}$, we find

$$\frac{\left(\frac{Q}{m_b^*}\right)^2 - \left(\frac{K}{m_w^*}\right)^2}{\frac{2QK}{m_b^*m_w^*}} \sinh(Qb) \sin(Ka) + \cosh(Qb) \cos(Ka) = \cos k(a+b). \quad (3.29)$$

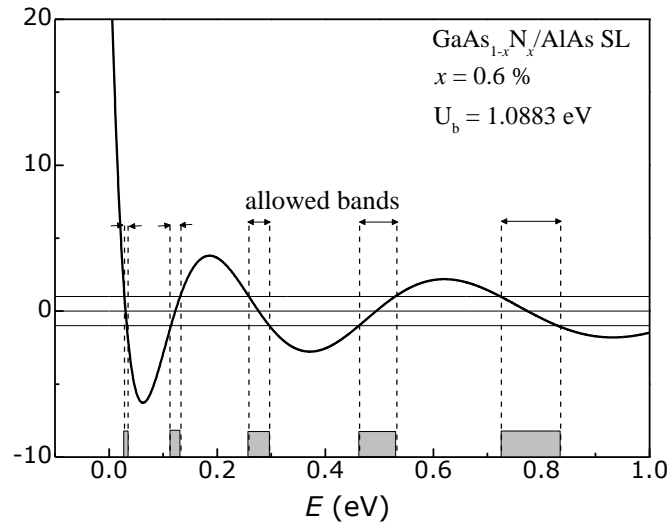


Figure 3.10: Solution of the Kronig-Penney model for a $\text{GaAs}_{1-x}\text{N}_x/\text{AlAs}$ SL with $x = 0.6\%$ at $T = 300\text{ K}$ ($m_b^* = 0.15 m_0$, $m_w^* = 0.0908 m_0$, $a = 10\text{ nm}$, $b = 1\text{ nm}$, $E_{g(\text{AlAs})} = 3.03\text{ eV}$, $E_{g(\text{GaAsN})} = 1.2993\text{ eV}$, and $U_b = 1.0883\text{ eV}$). Propagating solutions are permitted only in the shaded regions of E , where $|\cos k(a+b)| \leq 1$.

Figure 3.10 shows the dependence of the left-hand side (LHS) of Eq. 3.29 on energy, E , for a GaAs_{1-x}N_x/AlAs SL with $x = 0.6\%$. Since the Bloch wave number k is real for propagating states, we consider $|\cos k(a + b)| \leq 1$. The permitted solutions of Eq. 3.29 are shown by the shaded area, where the values of E are allowed for the LHS of Eq. 3.25 falling between +1 and -1.

Similarly, we can solve the Kronig-Penney model for the valence band to find the allowed hole energy bands. The valence band is not affected by the N. Therefore the barrier height ΔE_V does not depend on the N concentration, x . If E_1 and HH_1 are respectively, the minima of the 1st electron and heavy hole minibands, then the energy of the optical transition between these two states can be written as

$$E_{X_1} = E_g + E_1 + HH_1, \quad (3.30)$$

where E_g is the band gap of GaAs_{1-x}N_x, which depends on the N content, x , as described by the BAC model (see section 2.1.1.1). Here we consider a N-level located at 0.23 eV above the conduction band minimum of GaAs at $T = 300\text{K}$ and an interaction parameter $C_{NM} = 2.7$ eV. We have instead neglected the exciton binding energy, which represents a small correction to E_{X_1} . Figure 3.10 shows the dependence of E_g and E_{X_1} on x .

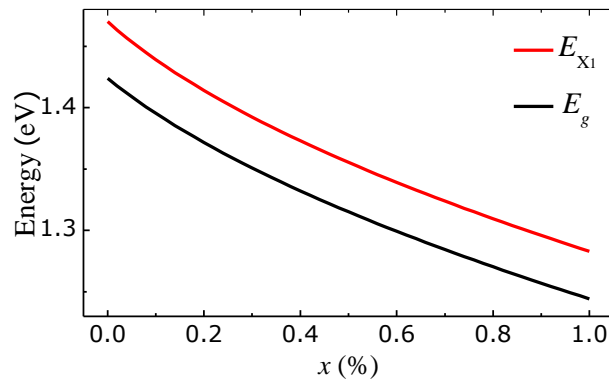


Figure 3.10: x -dependence of the energy band gap, E_g , and optical transition energy between the E_1 and HH_1 states, E_{X_1} , for a GaAs_{1-x}N_x/AlAs SL at $T = 300$ K.

Our $p-i-n$ diode has a Ga(AsN)/AlAs SL in its i -region. Under an applied forward bias, quasi-two dimensional electron and hole accumulation layers form in the undoped GaAs spacer layers on the n - and p -type sides of the barriers with bound states at energies E_{ae} and E_{ah} . Electrons can tunnel from the electron accumulation layer into the electron miniband states of the SL, E_n . Similarly, holes can tunnel from the hole accumulation layer into the hole miniband states HH_n and LH_n (where $n = 1, 2$), of the SL.

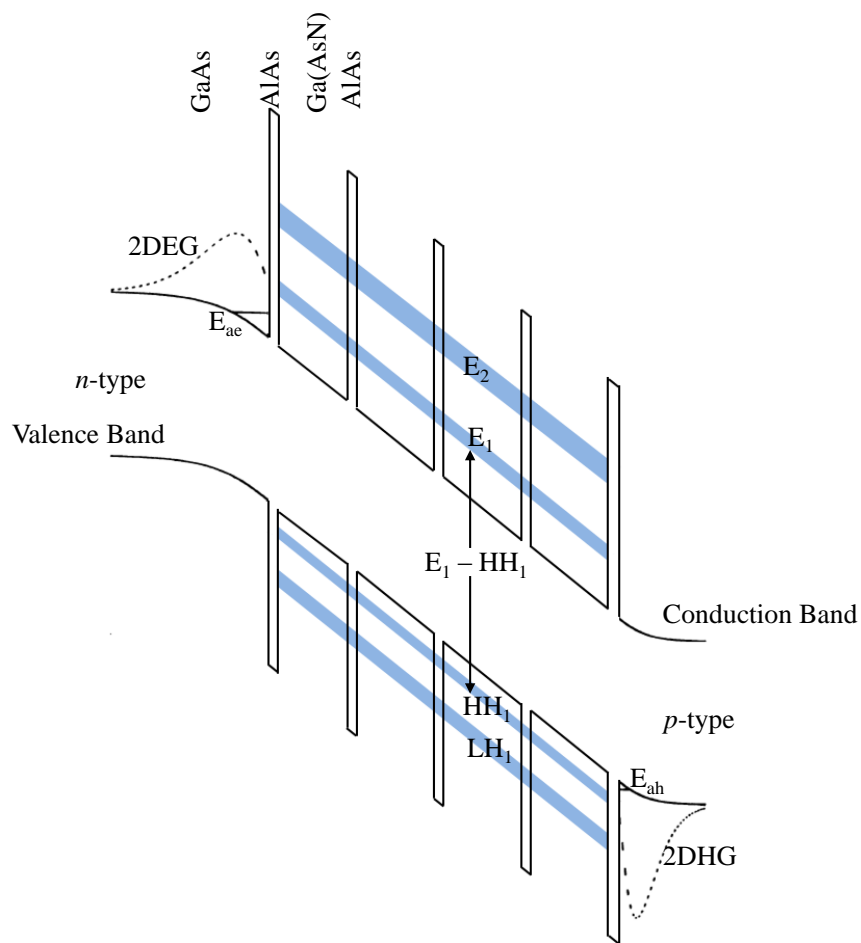


Figure 3.11: Schematic band diagram of our device in forward bias. Tunneling of electrons (holes) takes place from 2D quasi-bound states (E_{ae} and E_{ah} , respectively) into the miniband states of the SL (E_n , HH_n , and LH_n , where $n = 1, 2$).

Chapter 4

Samples and experimental setup

This chapter describes the samples, experimental equipment and techniques used to obtain the results presented in this thesis. A range of optical and electrical techniques were used in the study of III-N-V QWs, *p-i-n* diodes based on Ga(AsN)/AlAs superlattices and GaAs/AlAs QW resonant tunneling diodes, and *p-n* junctions based on 2D van der Waals crystals. The experimental setup used for topographical and compositional studies are also presented.

4.1 Sample growth and hydrogenation

4.1.1 III-N-V epilayer and QW structures

In this study, we investigate a Ga(AsN)/GaAs QW, a Ga(AsN) epilayer, an (InGa)(AsN)/GaAs QW, a Ga(PN) alloy, and a Ga(PN)/GaP multi-QW (MQW). The structural layer layout and *post-growth* hydrogenation conditions of each sample are described below. The as-grown samples were hydrogenated by ion beam irradiation using a Kaufman source¹⁰⁹ at the University of Rome by Prof. M. Capizzi and his group.

4.1.1.1 Ga(AsN)/GaAs QW

The Ga(AsN)/GaAs QW sample was grown by Dr. S. Rubini and Dr. F. Martelli (TASC-IOM-CNR, Area Science Park, Italy) by Molecular Beam Epitaxy (MBE) on a (001)-oriented GaAs substrate and has the following layer composition, in order of growth: an undoped GaAs buffer layer grown at 600 °C, a 6 nm Ga(AsN) QW with [N] = 0.9% and a 30 nm undoped GaAs cap layer both grown at 500 °C,

see Figure 4.1. The N-content was determined by high resolution x-ray diffraction (HRXRD) measurements and further supported by photoluminescence (PL) studies showing that the Ga(AsN) QW PL emission is red-shifted by 0.13 eV relative to the GaAs PL emission at $T = 300$ K.

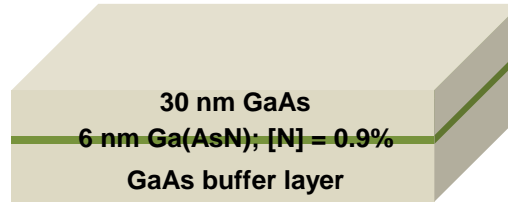


Figure 4.1: Schematic diagram of the layer structure of our Ga(AsN)/GaAs QW.

Table 4.1: H dose in Ga(AsN) QW samples V, H1, H2, H3, and H0.

<i>Sample</i>	<i>H dose (ions/cm²)</i>
V	0
H1	4×10^{16}
H2	6×10^{16}
H3	8×10^{16}
H0	2×10^{16}

The as-grown sample was hydrogenated at $T_H = 200$ °C with an ion-beam energy of 100 eV and nominal H-doses of $d_H = 4 \times 10^{16}$, 6×10^{16} and 8×10^{16} ions/cm². We refer to these hydrogenated samples as H1, H2 and H3, respectively, and the non-hydrogenated sample as V (Virgin). The areal density of H-atoms in the samples amounts to about 1% of the nominal doses quoted above, as derived from secondary ion mass spectrometry¹¹⁰ and nuclear reaction analysis⁶ on Ga(AsN) samples similar to those studied in this work. Also, an additional sample (H0) was considered. This was grown by MBE and has the same structure as sample V except for an additional Al_{0.7}Ga_{0.3}As layer grown above the GaAs buffer layer and for the N content (1%) in

the QW. This sample was hydrogenated with $d_H = 2 \times 10^{16}$ ions/cm². The nominal H dose for each sample is indicated in Table 4.1.

Figure 4.2 shows the detailed schematic diagram of a Kaufman source.¹⁰⁹ Molecular hydrogen is pumped into the ionization chamber, where it is ionized and/or dissociated into *protons* by the electrons emitted from a hot tungsten filament (cathode) towards the walls of the chamber (anode). A magnet spirals the electrons' trajectories, enhancing the cross-section for the hydrogen ionization process. Hydrogen ions (H⁺) are then accelerated by a set of grids held at high-voltage, so that an ion beam with a Gaussian profile ($\sigma \sim 25$ mm) is generated.¹⁰⁹ The ion beam enters the main chamber and impinges on the sample, which is electrically grounded. A very low pressure ($\sim 5 \times 10^{-7}$ mbar) is achieved by a turbo-molecular pump before opening the H flux, and a vacuum of $\sim 3 \times 10^{-4}$ mbar is maintained in the main chamber during the H irradiation of the sample. The heating lamp behind the sample holder provides a constant temperature to the sample. This allows us to control the hydrogen diffusion depth profile.¹⁰⁹ The H tends to accumulate on the surface, but for sufficiently high temperatures, it can also diffuse into the bulk.¹¹⁰

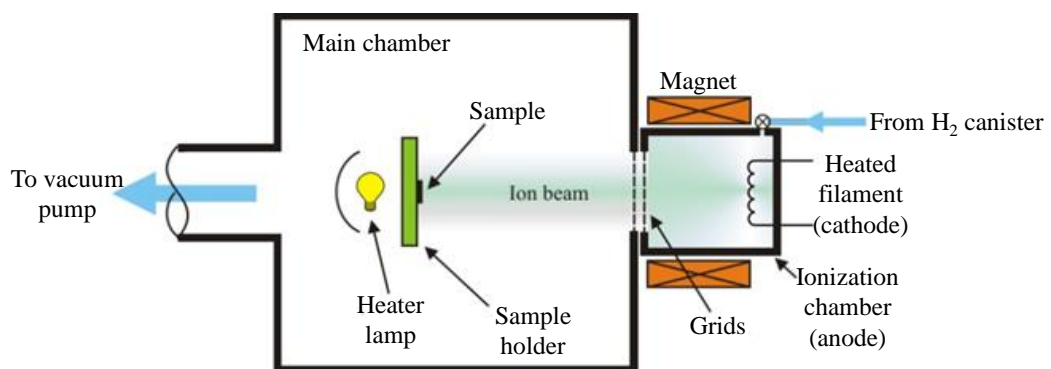


Figure 4.2: Schematic of a Kaufman source. Picture reproduced from Ref [109].

4.1.1.2 Ga(AsN) epilayer

The Ga(AsN) epilayer was grown by Dr. S. Rubini and Dr. F. Martelli (TASC-IOM-CNR, Area Science Park, Italy) by MBE on a (001)-oriented GaAs substrate and has the following layer composition, in order of growth: an undoped 500 nm thick GaAs buffer layer grown at 600 °C, a 200 nm Ga(AsN) with [N] = 0.92% and a 20 nm undoped GaAs cap layer both grown at 500 °C, see Figure 4.3. The as-grown sample was hydrogenated at $T_H = 300$ °C with an ion-beam energy of 100 eV and impinging H-dose of $d_H = 2 \times 10^{18}$ ions/cm².

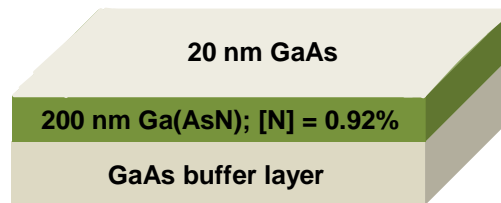


Figure 4.3: Schematic diagram of the layer structure of our Ga(AsN) epilayer.

4.1.1.3 (InGa)(AsN)/GaAs QW

The (InGa)(AsN)/GaAs QW was grown by Prof. A. Forchel (University of Wuerzburg, Germany) by MBE on a (001)-oriented GaAs substrate. It has the following layer composition, in order of growth: an undoped 500 nm thick GaAs buffer layer, a 6.8 nm (InGa)(AsN) QW with [In] = 32% and [N] = 2.7% grown at 450 °C and a 100 nm undoped GaAs cap layer (see Figure 4.4). This sample was hydrogenated at $T_H = 300$ °C with an ion-beam energy of 100 eV and impinging H-dose of $d_H = 5 \times 10^{17}$ ions/cm².

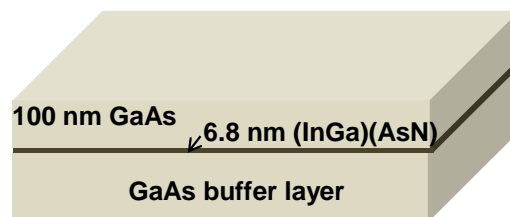


Figure 4.4: Schematic diagram of the layer structure of our (InGa)(AsN)/GaAs QW.

4.1.1.4 Ga(PN) alloy and Ga(PN)/GaP MQW

The Ga(PN) alloy and Ga(PN)/GaP MQW structures were grown by low pressure (50 mbar) MOVPE using an horizontal reactor system on a GaP substrate by Dr. W. Stolz (Philipps-University, Marburg, Germany). The Ga(PN) alloy has [N] = 0.15% and thickness of 500 nm. The MQW consists of five QWs. Each QW has a well width of 10 nm, a GaP barrier thickness of 70 nm and [N] = 1.1%; see Figure 4.5b. These samples were hydrogenated at $T_H = 300$ °C with an ion-beam energy of 100 eV and impinging H-doses of $d_H = 7 \times 10^{18}$ and 8×10^{18} ions/cm² in the Ga(PN) and Ga(PN) MQWs, respectively.

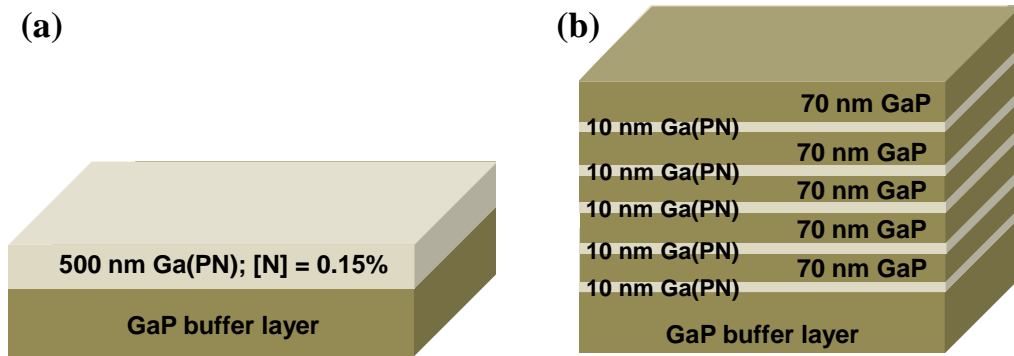


Figure 4.5: Schematic diagram of the layer structure of our (a) Ga(PN) alloy and (b) Ga(PN)/GaP MQW.

4.1.2 Superlattice *p-i-n* diode structures

Our *p-i-n* Ga(AsN)/AlAs superlattices (SLs) were grown by MBE using a N-plasma source at the University of Sheffield by Prof. M. Hopkinson. Each SL was grown on a n^+ -GaAs (001) substrate with the following order of growth layers: A 500 nm-thick n^+ -doped GaAs contact layer (Si-doped to 2×10^{18} cm⁻³), a 50 nm n -doped GaAs layer ($n = 2 \times 10^{17}$ cm⁻³), a 10 nm undoped GaAs layer, an undoped 10-period Ga(AsN)/AlAs SL (each SL unit cell consisting of a 1 nm AlAs barrier, a 1 nm GaAs layer, a 8 nm Ga(AsN) layer - with [N] = 0, 0.35, 0.6, or 0.85 % -, and a 1

nm GaAs layer), a 1 nm AlAs barrier, a 10 nm undoped GaAs layer, a 50 nm p -doped GaAs layer (Be-doped to $2 \times 10^{17} \text{ cm}^{-3}$), and finally a 500 nm p^+ -doped GaAs top contact layer ($p^+ = 2 \times 10^{18} \text{ cm}^{-3}$); see Figure 4.6. The samples were grown at 590 °C except for the SL region, which was grown at 500 °C. The nitrogen content in the Ga(AsN) layers was determined by x-ray diffraction analysis. The p - i - n structures were processed using conventional optical lithography into circular mesas of diameter $d = 200 \mu\text{m}$. A ring-shaped Au/Ge electrical contact was fabricated on the top surface of the mesa to permit hydrogen implantation and measurements of the current-voltage, I - V , characteristics, EL, and PC spectra. In this work positive bias is defined with the top p -contact layer biased positively.

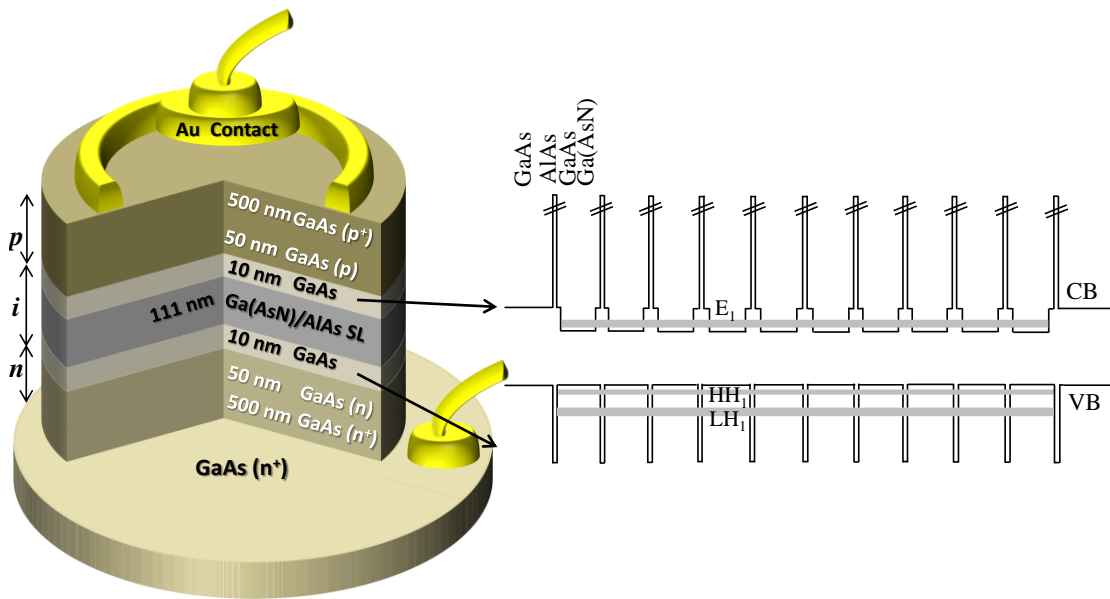


Figure 4.6: Schematic diagram of the superlattice p - i - n diode and the band structure of the Ga(AsN)/ AlAs superlattice.

The processed devices were exposed to a low-energy ($E = 100 \text{ eV}$) hydrogen-ion beam generated by a Kaufman source under different impinging nominal doses (from $d_H = 1 \times 10^{18}$ to $5 \times 10^{18} \text{ ions/cm}^2$) at various temperatures ranging from $T_H = 300 \text{ °C}$ to 340 °C at the University of Rome by Dr. G. Pettinari and Prof. M. Capizzi.

Following preliminary studies of the effects of hydrogen on the resistivity of the p -type contact layer, relatively low hydrogen doses ($d_H = 1 \times 10^{18}$ ions/ cm^2) were chosen to minimize the H-induced neutralization of the acceptors in the top p -contact GaAs layer.¹¹¹ On the other hand, these doses proved to be appropriate for the diffusion of hydrogen into the Ga(AsN)/AlAs SL.¹¹²

4.1.3 Resonant tunneling diodes

Our GaAs/AlAs QW resonant tunneling structure was grown by MBE on a (001) n^+ -GaAs substrate and has the following layer layout, in order of growth (see Figure 4.7): a 300 nm contact layer of n^+ -GaAs (Si-doped to 2×10^{18} cm^{-3}), a 100 nm buffer layer of n -GaAs ($n = 2 \times 10^{17}$ cm^{-3}), an undoped central intrinsic region comprising a 20 nm GaAs spacer layer, a 5 nm AlAs tunnel barrier, a 6 nm GaAs QW, a 5 nm AlAs tunnel barrier, and a 10 nm GaAs spacer layer, and finally, a 50 nm contact layer of p^+ -GaAs (C-doped to 1×10^{19} cm^{-3}); all layers were grown at 600 °C. The structure was processed into 200 μm and 400 μm diameter mesa diodes with a top ring-shaped Ti/Au electrical contact for optical access.

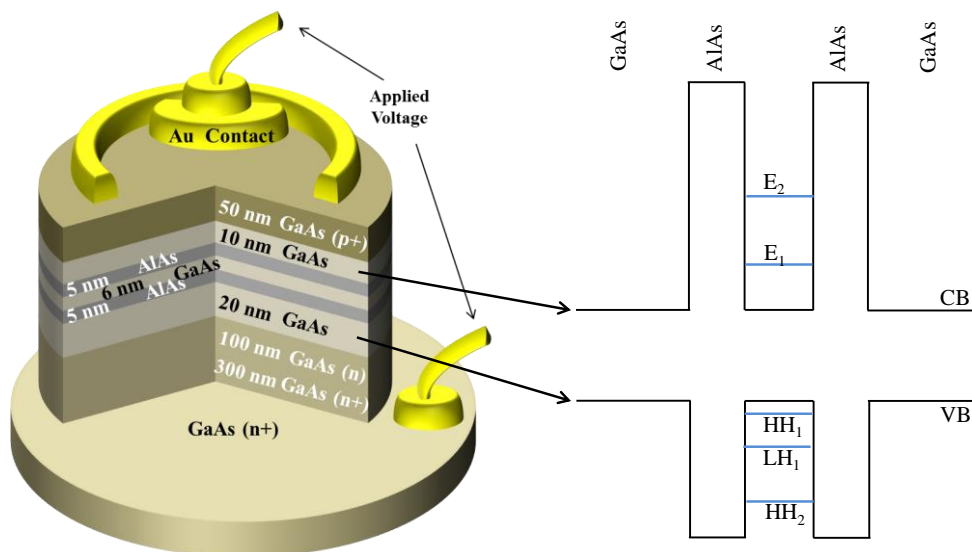


Figure 4.7: (a) Schematic diagram of the layer structure of our RTD and the band structure of the AlAs/GaAs/AlAs double barrier QW.

The processed devices were exposed to a low-energy ($E = 100$ eV) ion beam generated by a Kaufman source under different impinging H-doses (ranging from 6×10^{16} ions cm^{-2} to 1×10^{19} ions cm^{-2}) and temperatures (ranging from 20 °C to 250 °C). The samples were grown and processed at the University of Nottingham by Dr. R. P. Champion and hydrogenated at the University of Rome by Dr. G. Pettinari and Prof. M. Capizzi.

4.1.4 Mechanically-formed van der Waals junctions

Our samples are prepared from bulk Bridgman-grown crystals of rhombohedral γ -InSe and hexagonal ϵ -GaSe. For the heterojunction, we used n -InSe and p -GaSe crystals with concentrations of electrons and holes of 10^{15} cm^{-3} and 10^{13} cm^{-3} , respectively, which were determined from separate Hall effect measurements.⁹² For the homojunction, the undoped and intentionally Cd-doped InSe crystals have majority carrier concentrations of 10^{15} cm^{-3} (n -type) and 10^{13} cm^{-3} (p -type), respectively.¹¹³ Flakes between 1 μm^2 to ~ 1 cm^2 were prepared from as-grown crystals by mechanical exfoliation with adhesive tape with thickness from 1 nm to 10 μm . An individual large (~ 1 cm^2) flake of thickness of ~ 1 - 10 μm was then pressed against the van der Waals surface of another layered crystal to form a homojunction (*e.g.* n -InSe on p -InSe) or a heterojunction (*e.g.* p -GaSe on n -InSe). Indium ohmic contacts were then formed on the top and bottom layers, see Figure 4.8.

The p -InSe/ n -In₂O₃ junctions were prepared by annealing the freshly cleaved Cd-doped (10^{13} cm^{-3}) p -InSe flakes of ~ 100 μm^2 at temperature $T = 450$ °C for 96 hours. Reactive evaporation of indium in oxygen atmosphere forms a thin layer (~ 0.4 μm) of In₂O₃ which has n -type conductivity ($\sim 3 \times 10^{19}$ cm^{-3}).¹¹³⁻¹¹⁴ The long-time oxidation (96 h) at $T = 450$ °C of the InSe layer is accompanied by the formation of

an intermediate layer, $\text{In}_2(\text{SeO}_4)_3$.^{8, 115} Indium ohmic contacts were then formed on the top and bottom layers. All these samples were grown at the Institute for Problems of Materials Science, the National Academy of Sciences of Ukraine, Chernivtsi by Prof. Z. D. Kovalyuk and Mr. Z. R. Kudrynskiy. The devices were fabricated at Nottingham or Chernivtsi.

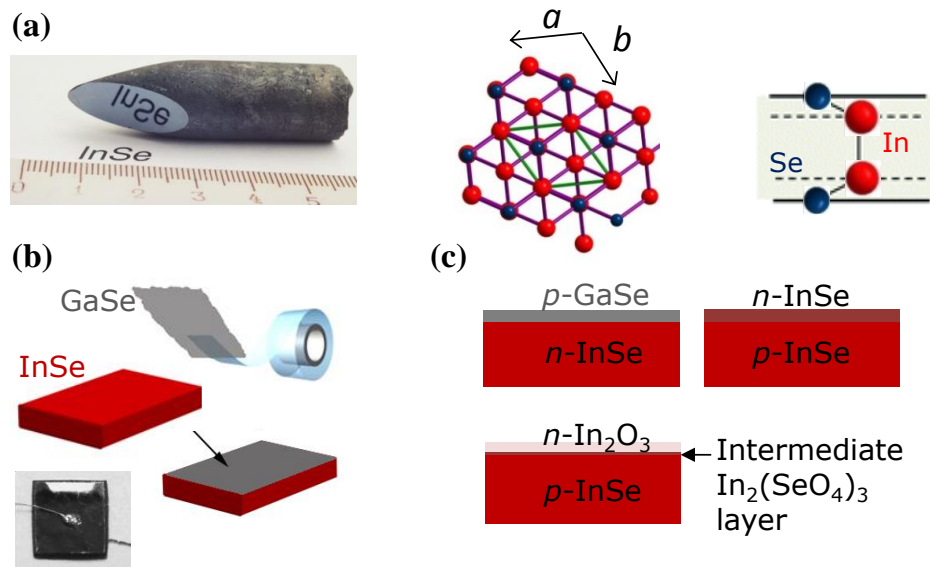


Figure 4.8: (a) Optical image of a Bridgman-grown InSe ingot and crystal structure of rhombohedral γ -InSe. (b) Exfoliation and mechanical adhesion used to fabricate junctions based on InSe and GaSe, and optical image of a junction device. (c) Schematic of our three junction devices.

4.2 Experimental techniques: transport measurements

4.2.1 Low noise current – voltage measurements

The I - V characteristics of our RTDs and p - i - n diodes were acquired using a simple circuit. The device was mounted on a sample probe designed to directly dip into a liquid helium dewer for low temperature ($T = 4.2$ K) measurements. A Keithley 2400 DC voltage source was connected in parallel with the sample probe by co-axial cables. Data acquisition was controlled by a written LabView program. The Keithley 2400 voltage source can measure currents down to 1nA. To measure current

values down to pA with low noise, a different low noise setup (I - V converter) was used.

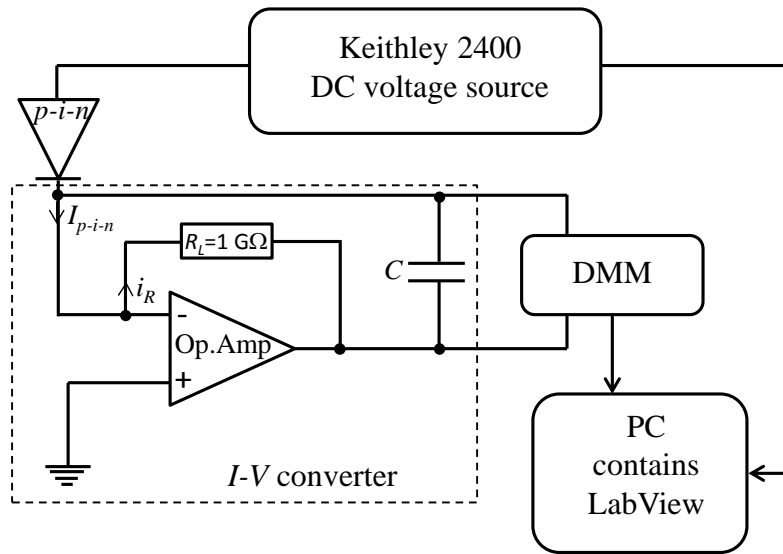


Figure 4.9: The low noise I - V measurement circuit. A virtual ground is stabilized by the operational amplifier (Op.Amp) to the p - i - n diode. The voltage drop across the load resistor, R_L , gives the current through the p - i - n diode.

Figure 4.9 shows the experimental setup for low current measurements down to sub-pA. The I - V converter has a DC biased operational amplifier (Op.Amp) with $1\text{G}\Omega$ load resistor thus creating a virtual ground for the RTD/ p - i - n diode. The ideal Op.Amp has infinity input impedance and gives zero current through it. Thus the voltage across the load resistor is $V_L = R_L i_R$, which is measured by a digital multi meter (DMM: HP3457A). A capacitor ($C = 10\ \mu\text{F}$) was also used to stabilize the voltage.

4.2.2 Capacitance – voltage measurements

The C - V characteristics of the RTDs were measured using a Hewlett-Packard model 4275A LCR meter, which covers the frequency range 10 KHz to 10 MHz. This system can measure the capacitance over the range 0.01 fF to 199.99 μF with an

accuracy of $\sim 0.1\%$. The device was mounted on a four terminal (high and low terminals for current and voltage) sample probe designed to directly dip into a liquid helium dewer for low temperature ($T = 4.2\text{ K}$) measurements. A Keithley 2400 DC voltage source was connected in parallel with the sample probe by co-axial cables. Data acquisition was controlled by a LabView program.

4.3 Experimental techniques: optical studies

4.3.1 Room temperature micro-photoluminescence/electroluminescence

The room temperature $\mu\text{PL}/\mu\text{EL}$ measurements were carried out using a LabRAM HR-UV spectrometer equipped with a confocal microscope. This system provides high wavelength resolution down to $\Delta\lambda = 10^{-2}\text{ nm}$. The schematic diagram of the system is shown in Figure 4.10. The system has four main parts, which are described below.

Optical Microscope: imaging is carried out via a standard optical microscope. This has 3 objectives that provide 10 \times , 50 \times and 100 \times magnification. The focal length (f) and numerical aperture (NA) of each objective are $f = 18, 3.6, 1.8\text{ mm}$ and $NA = 0.25, 0.55, 0.9$, respectively.

Spectrometer: the $\mu\text{PL}/\mu\text{EL}$ signal is dispersed by a grating and detected by an (InGa)As or a Si-charged coupled device (CCD) array photodiode. The (InGa)As detector covers the λ range 800 nm to 1600 nm, and the Si- CCD detector covers the near UV to the visible range ($\lambda = 350\text{ nm}$ to 800 nm). Two gratings (150 and 1200 g/mm) can be selected for measurements in different λ - range and spectral resolution.

Optics: mirrors, beam splitter and filters are used to direct the laser beam from a He-Ne laser ($\lambda = 633\text{ nm}$) or a frequency doubled Nd:YVO₄ laser ($\lambda = 532\text{ nm}$) to the sample and for collecting light from the sample to the detectors.

XY/Z motorized stage: the stage can be moved point by point with a spatial resolution of $0.1\mu\text{m}$ along the X, Y and Z direction for area (X and Y) mapping, and line (X or Y) and depth (Z) profiling of the $\mu\text{PL}/\mu\text{EL}$. Mapping of the μPL along X and Y can also be carried out by scanning the laser over the fixed stage. This can be done by a motorized mirror.

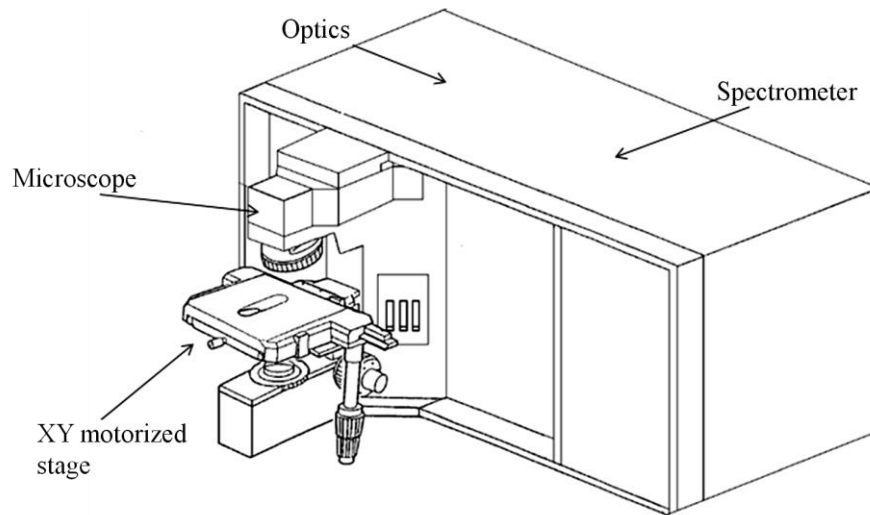


Figure 4.10: Schematic diagram of the LabRAM HR-UV Spectrometer. Diagram reproduced from Ref [116].

The schematic diagram of a confocal microscope is shown in Figure 4.11. The laser beam is focused by an objective to a small, nearly diffraction-limited spot on the sample surface. Also, the same objective collects the photo-excited light from the sample and sends it to a detector, which has an adjustable pinhole aperture. The emitted light from the spot passes through the pinhole, while the light from outside the spot or off the focal plane is blocked by the pinhole. The advantage of this confocality is a considerable reduction of the depth of focus. This allows us to separate the signal from each layer of a layered sample, thus improving the image resolution. For the μPL imaging, we can use two modes of laser scanning over the sample surface, XYZ motorized and XYZ scanlab. In the XYZ motorized mode, the

stage moves point by point with respect to the laser beam. In the second mode, the stage is fixed and the laser beam moves on the sample by a motorized mirror. We used the first mode for room temperature PL and the second mode for low temperature PL studies, in which the stage is replaced by a cold-finger cryostat (see Figure 4.13).

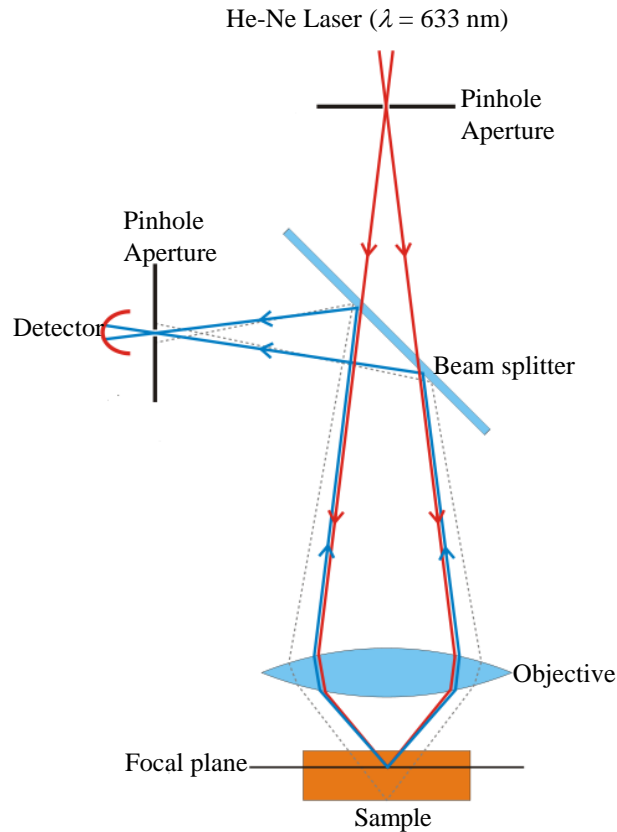


Figure 4.11: Schematic diagram of a confocal microscope.

Figure 4.12 shows the experimental setup for μPL measurement. The He-Ne laser beam was focused onto the sample by a $100\times$ objective, thus providing a laser spot with diameter $d < 1\mu\text{m}$. The size of the spot is determined by the numerical aperture (NA) of the objective $NA = n \sin\theta$, where n is the refractive index of the medium between the lens and the focal plane, and θ is the half angle between the marginal converging rays of the light cone. Using the Rayleigh criterion, the diameter of the spot can be written as $d_R = 1.22 \times \lambda/NA$. For $\lambda = 633 \text{ nm}$ and $NA =$

0.9, we find that $d_R = 0.86 \mu\text{m}$. This corresponds to the spatial resolution of our confocal microscope. The resolution can be limited by the size of the pinhole. The aperture should be small enough to ensure high spatial resolution and possibly large enough to let sufficient light into the detector.

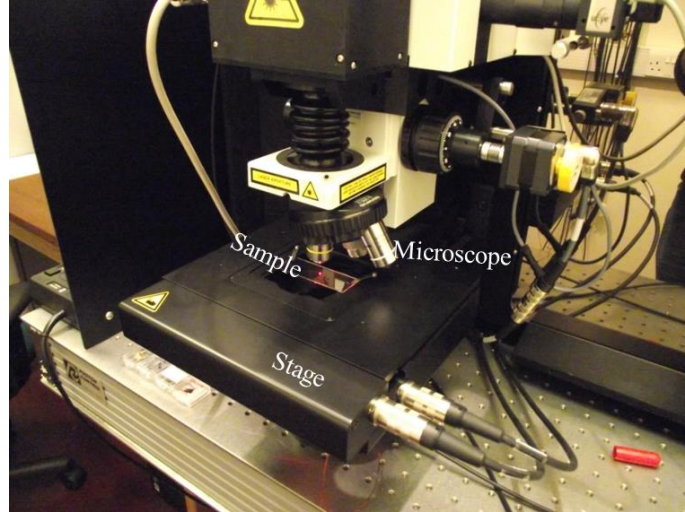


Figure 4.12: Experimental setup for μPL measurements at $T = 300 \text{ K}$. The picture shows the microscope, stage, sample and the focused laser beam.

4.3.2 Low temperature micro-photoluminescence/ electroluminescence

For low temperature ($T = 10 \text{ K}$) $\mu\text{PL}/\mu\text{EL}$ studies, we used the LabRAM HR-UV spectroscopy and a cold-finger cryostat (see Figure 4.13). The sample is mounted close to the inner surface of the optical window. The sample holder is a screw mounting arrangement and thermally isolated and tightly fixed on the vacuum housing for low drift. The distance of the sample from the surface can be adjusted from 0 to 3 mm. An external pressure regulator draws a continuous Helium flux from the Helium dewar to the cryostat through a transfer tube. A temperature meter and heater are connected to the cryostat and permit to measure and control the temperature of the cryostat and of the sample.

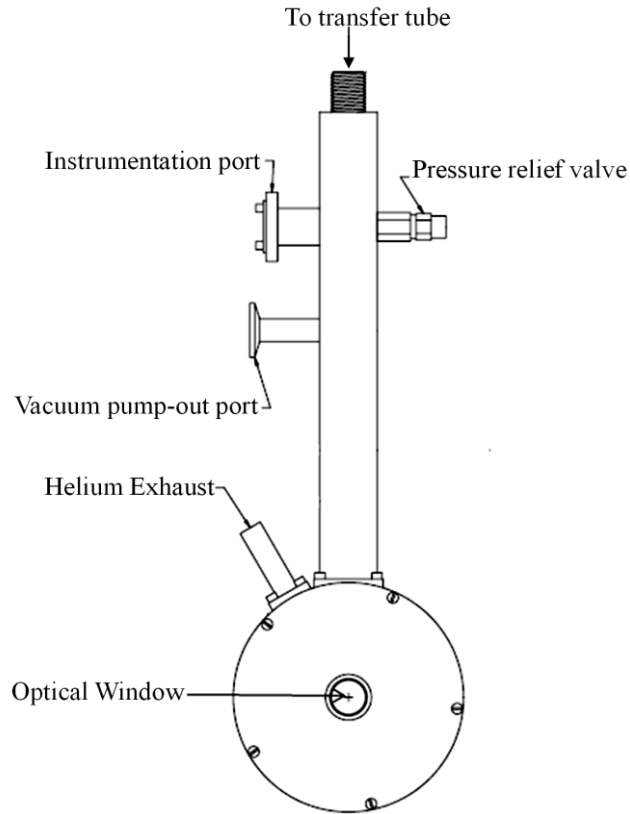


Figure 4.13: Schematic diagram of a cold-finger cryostat (model: Helitran LT-3 OM) for low temperature μ PL/ μ EL measurements. Picture reproduced from Ref [117].

4.3.3 Laser writing

For the laser writing experiments, the laser beam was focused onto the sample thus providing a laser spot with diameter of $\sim 1\mu\text{m}$. Four different lasers were used, an Ar laser ($\lambda = 515\text{ nm}$), a He-Ne laser ($\lambda = 633\text{ nm}$), a frequency doubled Nd:YVO₄ laser ($\lambda = 532\text{ nm}$) and a Ti:Sapphire laser ($\lambda = 695\text{-}830\text{ nm}$). We produced annealed spots by using various laser powers (3–120 mW) and exposure times (t_a up to 3 minutes). Figure 4.14 shows the experimental setup for the annealing with the Ar-laser. Here we used a 100 \times objective and a beam splitter was used to reflect the beam on a screen thus facilitating the visualization of the focusing conditions. A similar setup also used for laser writing with a Ti:Sapphire laser. We

also used a μ PL system equipped with a confocal microscope for laser writing with a He-Ne or a frequency doubled Nd:YVO4 laser (see Figure 4.12).

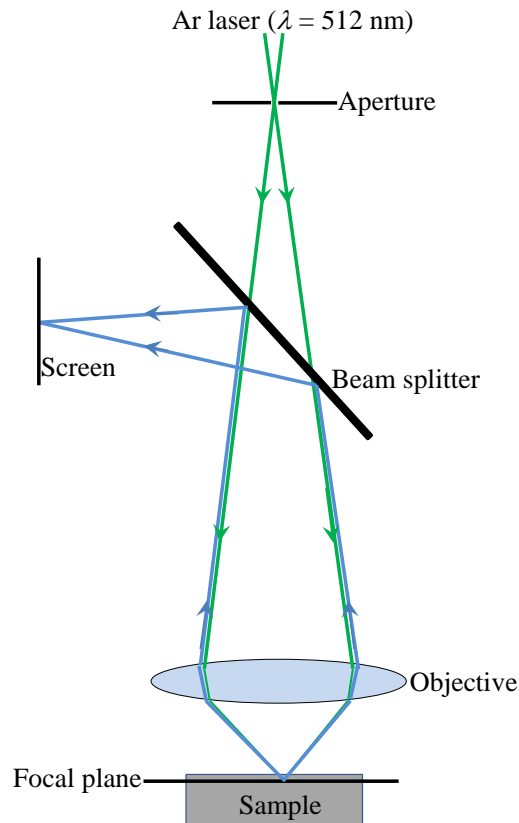


Figure 4.14: Experimental setup for laser writing with an Ar laser.

4.3.4 Photocurrent measurement

For the photocurrent (PC) measurements light from a 250 W quartz halogen lamp, dispersed through a 0.25 m monochromator (bandwidth of ~ 10 nm), and modulated with a mechanical chopper, was focused onto our *p-i-n* diodes, ($P \sim 10^{-3}$ W/cm²), see Figure 4.15. The *p-i-n* diode was biased at $V \leq 0$ V. The photocurrent signal was measured using a standard lock-in amplification technique. A Keithley 2400 DC voltage source was connected in parallel with the sample by co-axial cables. Data acquisition was controlled by a LabView program.

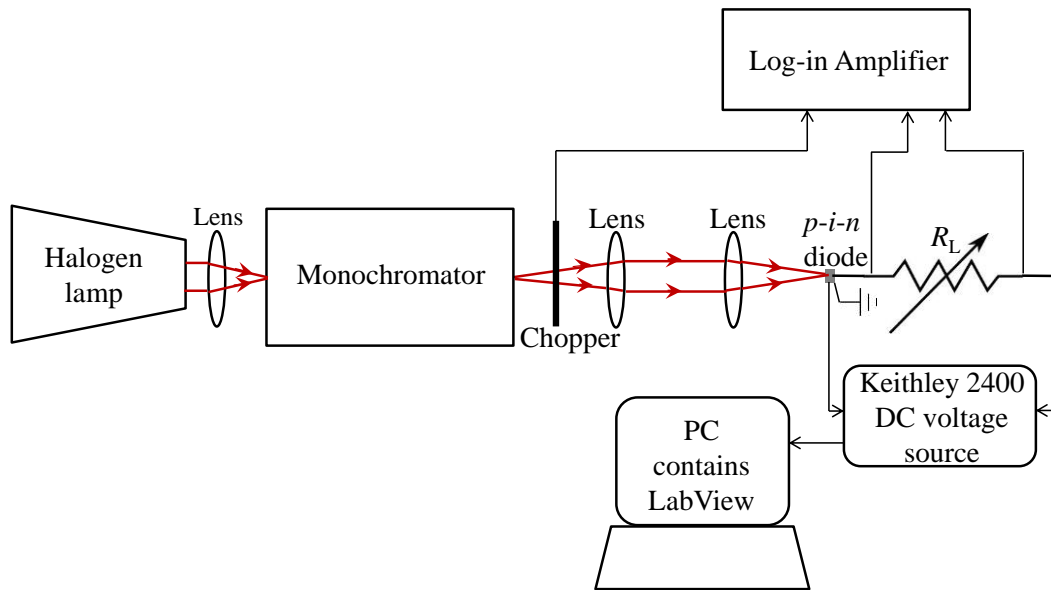


Figure 4.15: Experimental setup for photocurrent measurement. The voltage drop across the load resistor, R_L , gives the photocurrent in the $p-i-n$ diode.

4.4 Experimental techniques: topographical/compositional studies

4.4.1 Scanning electron microscopy (SEM)

We used an FEI Quanta 200 3D FIB-SEM to image the laser annealed region. The schematic diagram of the SEM is shown in Figure 4.16. A tungsten filament in the electron gun is heated by an applied voltage thus causing thermionic electron emission. The emitted electron beam is accelerated towards the anode, narrowed by a condenser lens, and focused as a very fine point on the sample by the objective lens. The focused electron beam induces emission of secondary electrons from the sample, which are collected by the electron detector for imaging and analysis. Also, photons emitted by the interaction of the focused electron beam with the sample are detected by the energy dispersive x-ray detector.

Our SEM system has a spatial resolution of 3.5 nm and 15 nm for an accelerating voltage $V = 30$ kV and 2 kV, respectively. The spatial resolution also depends on the electron spot size, which can be controlled by the condenser lens,

objective lens, position of the filament in the cathode, bias voltage and accelerating voltage. The sample topography at several points is imaged by moving the electron beam with respect to the sample. The sample can be moved with respect to the detector along the x-axis (side by side) and along the y-axis (forward and backward). It can also be tilted and rotated in the plane.

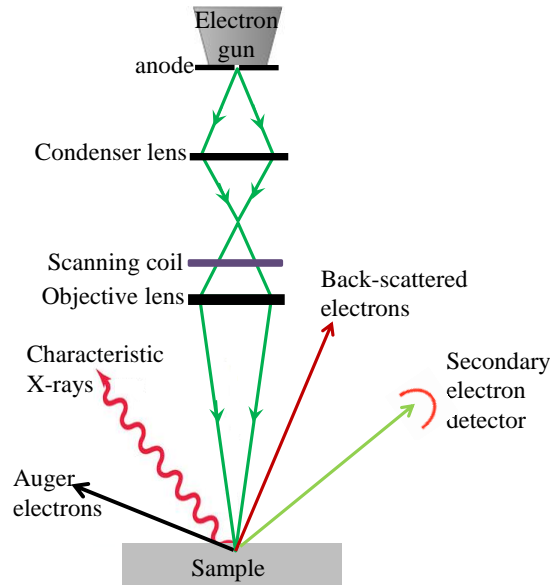


Figure 4.16: Schematic diagram of a Scanning Electron Microscopy. Picture reproduced from Ref [118].

4.4.2 Transmission electron microscopy (TEM)

The transmission electron microscope utilizes energetic electrons to provide compositional, morphologic and crystallographic information. The sample should be thin enough to be transparent to electrons. Among the different signals generated from the interaction between the electron beam and a sample (see Figure 4.17), the transmitted direct beam and the elastic and inelastically scattered electrons can be collected and analyzed. The high energy electrons, accelerated by several hundred kV potential, have a much smaller wavelength than the typical interatomic spacing. Thus TEM provides accurate information about the material under study.¹¹⁹

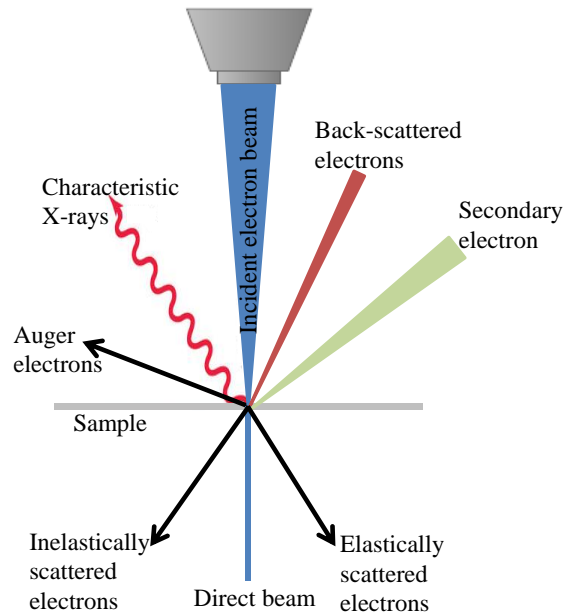


Figure 4.17: Signals generated from the interaction between a high energy electron beam and a very thin, electron transparent sample. Picture reproduced from Ref [119].

For the transmission electron microscopy (TEM), high-resolution TEM (HRTEM) and energy-dispersive X-rays (EDX) studies, we used a JEOL 2100F FEG-TEM equipped with an Oxford Instruments INCA EDX system. In the HRTEM technique, the image is formed by the interference of multiple beams so that the phase and amplitude of the diffracted beams contribute to the contrast in the image.¹¹⁹

4.4.3 Atomic force microscopy (AFM)

We used a MFP-3D AFM system to probe the surface topographical map of our samples. The AFM has a sub-angstrom resolution in the Z direction (depth) and nanometer resolution in the XY plane. The AFM consists of a low spring constant cantilever with a sharp tip, an IR-laser and a deflection sensor, which is a four-

quadrant-photodiode. A schematic diagram of an AFM is shown in Figure 4.18. The sharp tip of the cantilever is very close to the sample surface and during the scanning it reacts in response to the short range repulsive force (~ 10 nN) between the tip and the sample surface. A focused laser beam on the backside of the cantilever is reflected onto a split photodiode, which measures the deflection or oscillation amplitude. Detected changes in the cantilever deflection or oscillation are corrected to a constant value by triggering the cantilever in the Z direction through a feedback controlled piezo. The feedback voltage correlates to a voltage-distance calibration factor, thus determining the height at a given XY coordinate. The AFM image displays the surface in all three dimensions without the limit of optical diffraction present in the optical microscopes. To resolve atomic-scale structures, we operated the AFM in the contact mode. In the contact mode, the cantilever tip is scanned over the sample surface in order to keep constant the short range repulsive force between the surface and the AFM tip.¹²¹

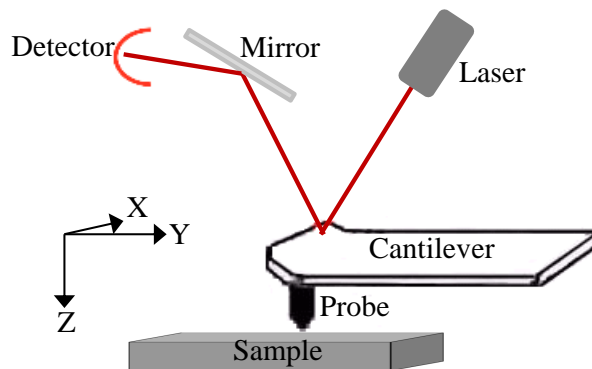


Figure 4.18: Schematic diagram of an Atomic Force Microscopy. Picture reproduced from Ref [120].

Chapter 5

Band-gap profiling by laser writing of H- containing III-N-Vs

This chapter describes how a focused laser beam can be used to control the electronic activity of N and H atoms in III-N-V quantum wells (QWs). Our micro-photoluminescence (μ PL) spectroscopy and mapping, and scanning electron microscopy (SEM) probe the effects of laser-induced modification of the N-H bonds on the physical properties of III-N-V alloys. Also, we use a conventional thermal annealing technique to probe the thermal stability of the laser annealed spots. Description of samples and the *post-growth* hydrogen irradiation conditions were given in section 4.1.1. Laser writing and PL mappings were performed by myself at the University of Nottingham. SEM and AFM imaging of the laser annealed areas were performed in collaboration with Dr. M. W. Fay and Dr. L. Turyanska respectively, at the Nottingham Nanotechnology and Nanoscience Centre, University of Nottingham. The results of this study were published in *Physical Review B* **86**, 155307 (2012).

5.1 Introduction

Hydrogen atoms are highly mobile and reactive elements that bind to several atomic species, they can passivate both deep and shallow crystal defects and impurities in semiconductors⁹ or act as dopants in narrow band gap semiconductors.¹²² The combination of hydrogenation and laser excitation of a semiconductor can also provide a successful tool for tuning electronic properties. In Ref. [123], we describe how a focused laser beam can be used to dissociate N-H complexes in hydrogenated Ga(AsN), thus modifying locally the electronic activity

of the N-atoms and the band gap energy. This recent finding has raised questions of fundamental interest, i.e. whether the physical process that drives the laser-induced modification of the N-H bonds in the III-V host crystal is a “thermal” or a “photonic” mechanism and whether this can be used to learn about the physics of H-related defects in III-N-Vs; also, despite this laser-assisted band gap engineering technique was successfully applied to Ga(AsN), its applicability to other technologically important III-N-V alloys^{1, 41, 124-125} has not yet been examined. These issues are not only of broad fundamental interest in the context of our understanding of the electronic properties of this class of alloys and H-related defects, but also relevant to the development of a versatile and reliable top-down nanofabrication approach and exploitation of III-N-Vs in future nanotechnologies. In this chapter, I demonstrate that the dissociation of the N-H complex in hydrogenated III-N-Vs can be laser-activated at temperatures that are significantly smaller than those (> 200 °C) required for thermal dissociation due to a resonant photon absorption by the N-H complex.

5.2 Room temperature photoluminescence studies

The room temperature photoluminescence (PL) spectra of our three hydrogenated Ga(AsN) QW samples (H1, H2, and H3 with H dose of $d_H = 4 \times 10^{16}$ ions/cm², 6×10^{16} ions/cm², and 8×10^{16} ions/cm², respectively) and the Virgin ‘V’ (non-hydrogenated) sample are shown in Figure 5.1a. Following the hydrogenation, hydrogen neutralizes the electronic activity of nitrogen through the formation of N-2H complexes thus causing a blue shift of the QW PL emission towards the PL emission energy of GaAs.¹⁵ One can notice that the blue shift increases with increasing the hydrogen dose and that in samples H1 and H2 the amount of diffused

hydrogen in the Ga(AsN) QW is not sufficient to neutralize all the N-atoms. However, in sample H3 the Ga(AsN) QW peak is fully quenched by H.

The concentration of electrically active N atoms in the Ga(AsN) QW of each sample was determined from the peak energy of the QW PL emission, E_{QW} , as shown in Figure 5.1b. Our model of E_{QW} includes the N-content, x , dependence of the band gap energy and of the electron effective mass, which we estimate using a two-level band-anticrossing model with a N-level located at 0.23 eV above the conduction band minimum of GaAs at $T = 300$ K and an interaction parameter $C_{NM} = 2.7$ eV.¹²⁶ We have instead neglected the exciton binding energy, which represents a small correction to the calculated energies. Details of the calculation are in the Appendix B. As shown in Figure 5.1b, we estimate that the electrically active N content in samples V, H1, H2, and H3 is equal to 0.95%, 0.37%, 0.35% and 0%, respectively. The high resolution x-ray diffraction (HRXRD) measurements indicate that the nominal concentration of N content in the V-sample is equal to 0.9%, in agreement with our estimate of x .

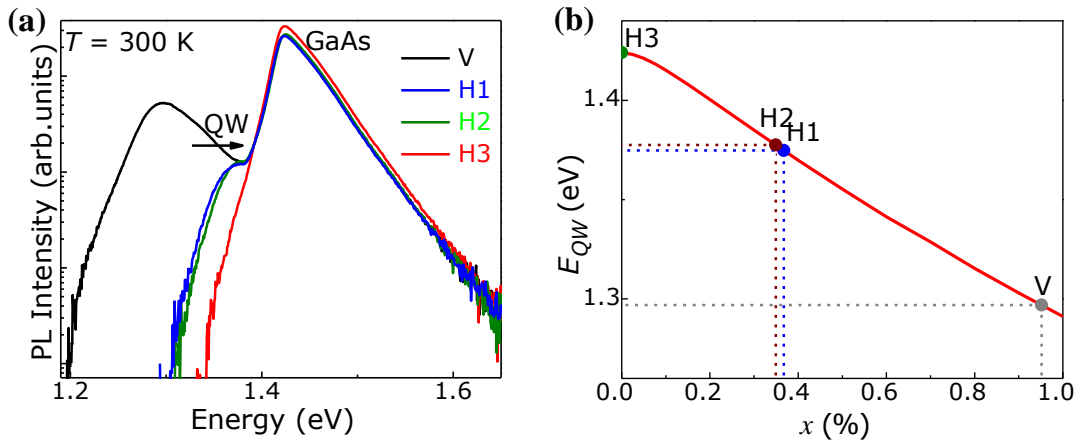


Figure 5.1: (a) μ PL spectra of samples V, H1, H2, and H3 at $T = 300$ K ($P = 1.2$ mW, $\lambda = 633$ nm). (b) Dependence of the peak energy of the QW PL emission, E_{QW} , on N-content, x , as derived from the band anti-crossing model.

5.3 Laser writing and band gap profiling of Ga(AsN)

In this section we show how the neutralization of the electronic activity of N by H as described in the previous section can be reversed locally using a focused laser beam, which acts to dissociate the N-H complexes. For the laser annealing experiments, we used a focused laser beam ($d \sim 1 \mu\text{m}$) of wavelength $\lambda = 515 \text{ nm}$, power P_a in the range 10-120 mW, and exposure time $t_a = 15 \text{ s}$. A series of light emitting regions were produced at various laser powers at room temperature ($T = 300 \text{ K}$). Images of the sample topography were acquired by atomic force microscopy (AFM) and by scanning electron microscopy (SEM). For the secondary electron imaging, an FEI Quanta 200 3D SEM equipped with an Everhart Thornley detector was used. This was operated at 30 kV for topographical sensitivity and at 1 kV (with a nominal current of 0.11 nA) to obtain dopant contrast sensitivity. Samples were plasma cleaned in a Fischione Model 1020 plasma cleaner immediately prior to analysis, and images were acquired from single pass scans at 30 μs dwell to reduce surface contamination contributions.

Figure 5.2a shows the room temperature ($T = 300 \text{ K}$) μPL spectra and μPL map of one of the hydrogenated Ga(AsN) samples (H2) after exposure for a time $t_a = 15 \text{ s}$ to a focused laser beam with diameter $d < 1 \mu\text{m}$, $\lambda = 515 \text{ nm}$ and $P_a = 10 \text{ mW}$. The μPL spectra were acquired at low laser power within and around the laser annealed spot. It can be seen that the QW PL emission is peaked at lower energies in proximity of the spot center (see the μPL spectra at positions A, B, C, and D in Figure 5.2a). The μPL map in the spectral range of the QW emission shows a light emitting region with an approximately Gaussian form of its intensity and a full-width at half-maximum (FWHM) of $0.95 \mu\text{m}$ that corresponds closely to the laser spot diameter. With increasing laser power the light emitting areas increase in size showing spot-

like (Figure 5.2a-b) or ring-like (Figure 5.2c) patterns, whose origin will be discussed later.

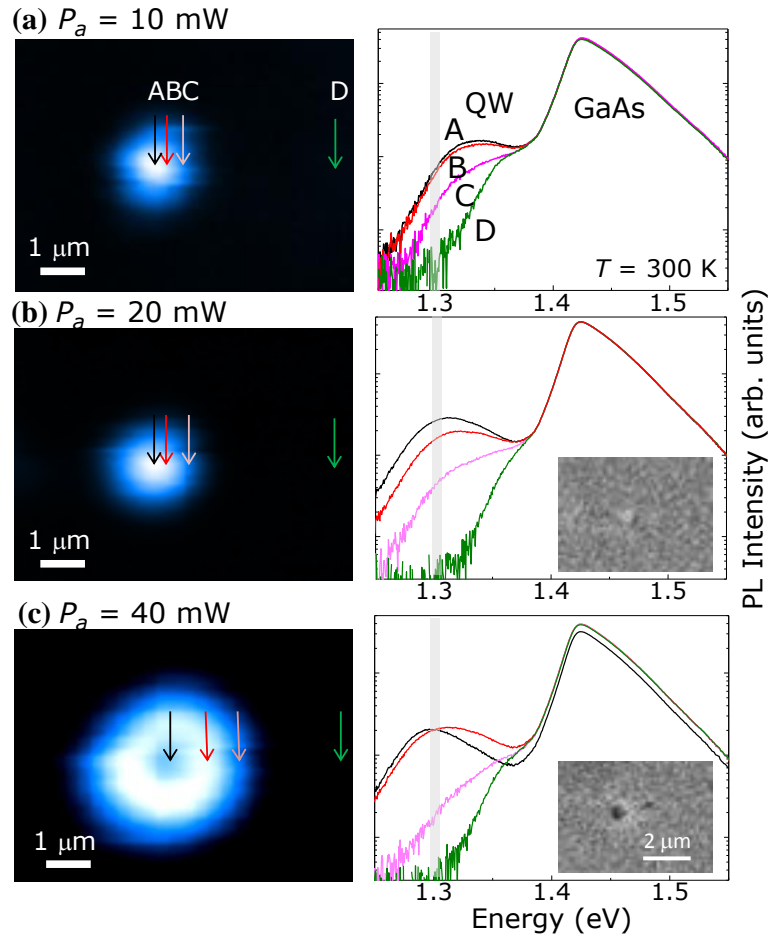


Figure 5.2. μ PL map at $T = 300$ K of an hydrogenated Ga(AsN) QW sample (H2) following exposure for a time $t_a = 15$ s to a focused laser beam with $\lambda = 515$ nm and (a) $P_a = 10$ mW, (b) 20 mW and (c) 40 mW. The μ PL spectra at positions A, B, C, and D are shown at each power on the right. The μ PL maps are obtained by plotting the μ PL intensity around $E = 1.30$ eV corresponding to the peak energy of the QW emission in the Virgin sample, V, (see grey area in the μ PL spectra) and were acquired with $P = 1.2$ mW and $\lambda = 633$ nm. Insets in (b) and (c) are 1kV SEM images of the laser annealed spots.

The incorporation of hydrogen in Ga(AsN) leads to the formation of several complexes.¹⁵ Di-hydrogen complexes are responsible for the neutralization of the electronic activity of nitrogen, that causes the band gap and lattice constant of the N-

free GaAs to be recovered.¹⁵ In our experiment, this neutralization effect is reversed locally using a focused laser beam, which acts to dissociate the complex, thus restoring the electronic activity of nitrogen.¹²³ We use the peak energy of the QW PL emission at different positions in each μ PL map (Figure 5.2a-c) to probe the spatial distribution of active-N, x_{eff} , and hence the percentage variation in the concentration of di-hydrogen N-H complexes, Δn_{N-H} . This is expressed as

$$|\Delta n_{N-H}| = (x_{eff} - x_0)/(x - x_0),$$

where x is the N concentration in the Virgin sample and x_0 is the concentration of N-atoms outside the laser treated area of the hydrogenated sample. The values of Δn_{N-H} at various laser powers and positions X in the QW plane are plotted in Figure 5.3a. It can be clearly seen that with increasing P_a : i) the minimum in the Δn_{N-H} profile becomes deeper; ii) all N-H complexes in the Ga(AsN) QW can be dissociated at laser powers $P_a \sim 40$ mW corresponding to $|\Delta n_{N-H}| \sim 100\%$; and iii) the FWHM, d_{N-H} , of the $\Delta n_{N-H}(X)$ curve increases above a minimum value corresponding to the diffraction limited size of the laser spot diameter. The dependence of Δn_{N-H} at $X = 0$, $|\Delta n_{N-H}|_{max}$, on P_a is plotted in Figure 5.3b for laser wavelengths $\lambda = 515$ and 633 nm. The dissociation of the N-H complex has a non-linear dependence on the laser power, whose origin will be discussed later.

To examine the contribution of thermal and photonic effects in the laser-induced ionization of the N-H complex and corresponding Δn_{N-H} profiles, we first model the spatial gradient of the lattice temperature, T_a , induced by the focused laser beam on the sample surface. Figure 5.3c shows the X -dependence of T_a at various laser powers calculated by using the T -dependent thermal conductivity¹²⁷ and absorption coefficients of GaAs at $\lambda = 515$ nm and $T = 300$ K.¹²⁸ Details of the calculation are in the Appendix C. For $P_a < 40$ mW, the calculated temperatures are

well below those required ($T_a > 250$ °C) for thermal dissociation of N-H complexes and out-gassing of H from the sample, as measured in our high temperature furnace experiments with T up to 450 °C and as also found in the literature.^{7, 15} Thus, under these laser exposure conditions, laser-heating cannot be responsible for the dissociation of the N-H bonds. This is also supported by our laser writing experiments at liquid Helium temperatures ($T = 4.2$ K) and laser exposure conditions ($P_a < 40$ mW) that correspond to calculated temperatures $T_a < 10$ K, see Figure 5.4.

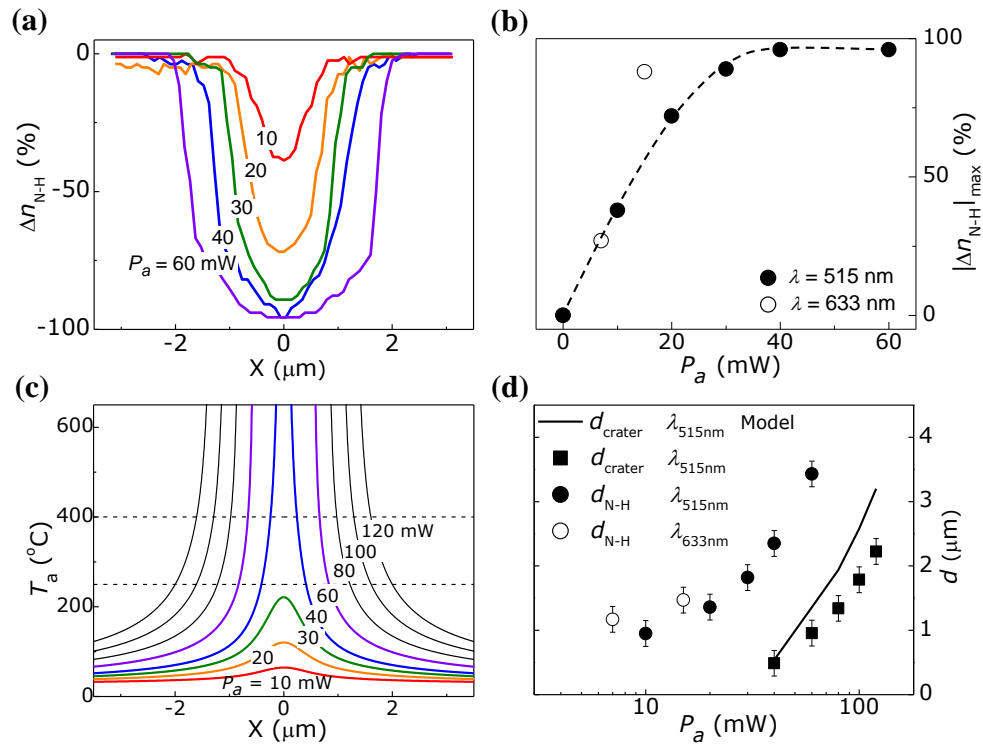


Figure 5.3. (a) Dependence of Δn_{N-H} on X at various P_a ($\lambda = 515$ nm, $t_a = 15$ s) in the hydrogenated Ga(AsN) QW (sample H2). (b) Dependence of $|\Delta n_{N-H}|_{\text{max}}$ on P_a ($\lambda = 515$ nm, $t_a = 15$ s and $\lambda = 633$ nm, $t_a = 20$ s). The dashed line is a guide to the eye. (c) Calculated T_a (X) curves at various P_a ($\lambda = 515$ nm, $t_a = 15$ s, beam waist 0.4 μm). Horizontal dashed lines highlight temperatures required for H-outgassing ($T_a > 250$ °C) and As-desorption ($T_a > 400$ °C). (d) Dependence of the full widths at half maximum of the Δn_{N-H} profile, d_{N-H} , on P_a at $\lambda = 515$ and 633 nm. The squares and line describe the P_a -dependence of d_{crater} (the diameter of the damaged surface area of the sample) as derived from the SEM study and our estimate based on the As-desorption model, respectively.

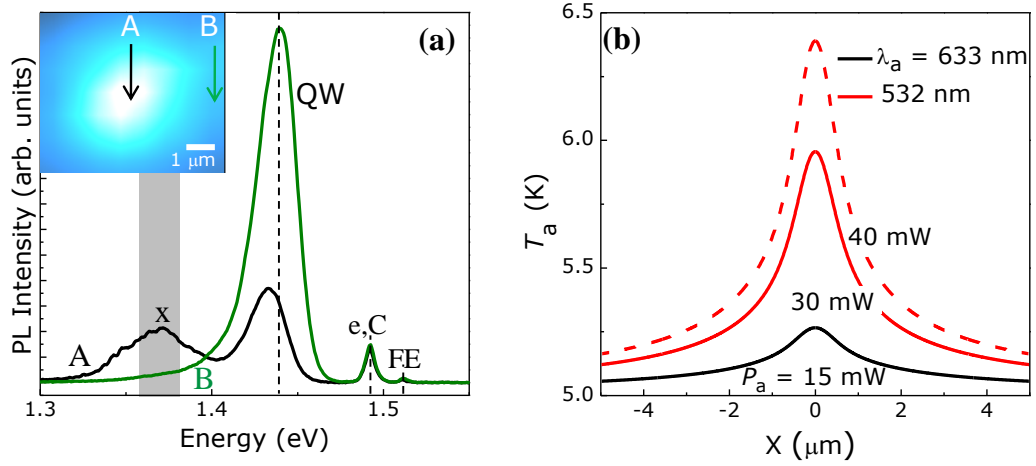


Figure 5.4. (a) μ PL map at $T = 5$ K of an hydrogenated Ga(AsN) QW sample (H2) following exposure for a time $t_a = 15$ s to a focused laser beam with $\lambda = 633$ nm and $P_a = 15$ mW at $T = 5$ K. The μ PL map is obtained by plotting the μ PL intensity around $E = 1.37$ eV. Following the laser writing at $T = 5$ K, a new emission appears on the lower energy side ($E = 1.37$ eV) of the QW emission ($E_{QW} = 1.44$ eV), labeled X. Laser writing activates the electronic activity of nitrogen, thus red shifting the QW PL emission and inducing a new recombination (band X) associated with N-related states. However, this laser power is not sufficient to reactivate all the passivated nitrogen. (b) Calculated $T_a(X)$ curves at various laser writing conditions ($P_a = 15$ mW and $\lambda = 633$ nm, $P_a = 30$ -40 mW and $\lambda = 532$ nm, $t_a = 15$ s, beam waist $0.5 \mu\text{m}$).

In contrast, we find that for laser exposure at $P_a \geq 40$ mW at $T = 300$ K, the lattice temperature increases very steeply in the center of the laser spot. This thermal runaway effect is caused by the low thermal conductivity of GaAs at high temperatures. Note that the temperature can rise up to values that can exceed those required for H-outgassing ($T_a > 250$ °C), As-desorption ($T_a > 400$ °C)¹²⁹ and melting of GaAs ($T_a > 1200$ °C). Thus, at high laser powers ($P_a \geq 40$ mW), the high temperatures ($T_a \geq 250$ °C) induced around the laser spot can cause thermal dissociation of the complex, diffusion and outgassing of H. This results into a broadening of the $\Delta n_{\text{N-H}}$ profile to full widths at half maximum, $d_{\text{N-H}}$, that exceed the

diffraction limited size of the laser beam (Figure 5.3d) and into an irreversible damage of the sample surface, see darker spot in the SEM and μ PL maps of Figure 5.2c. The measured values of d_{crater} , i.e. the diameter of the laser-induced surface damage revealed by SEM, increases with increasing P_a in qualitative agreement with the estimated width of the laser annealed region at temperatures $T_a > 400$ °C, see Figure 5.3d. No topographic changes can instead be revealed in samples laser annealed at lower powers ($P_a < 40$ mW). For these laser exposure conditions, AFM images show an atomically flat surface, whereas the SEM reveals only a weak contrast variation, which we attribute to the laser-induced change of the N-H complex concentration,¹³⁰ see Figure 5.5. The AFM image reveals that the surface between the craters is not damaged. The white horizontal lines and spots may due to dust particles on the surface. The vertical lines may due instead to the cracks produced by surface polishing.

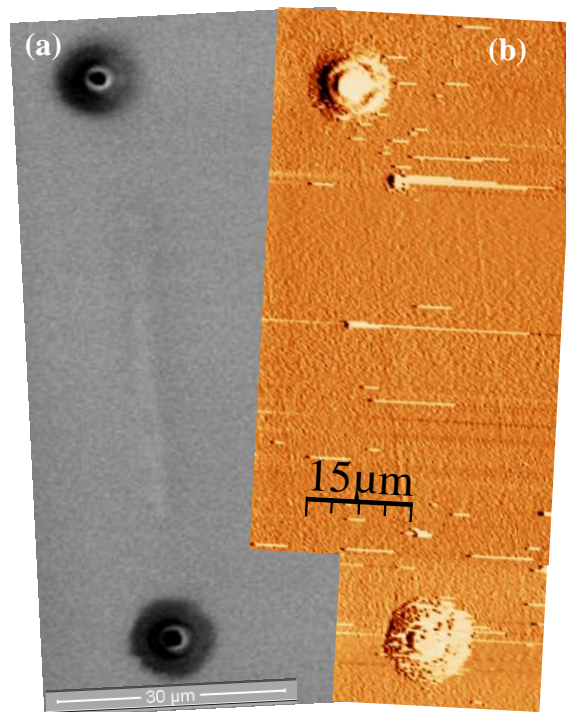


Figure 5.5: Image of a laser annealed line ($P_a = 20$ mW) on sample H0 ($d_{\text{H}} = 2 \times 10^{16}$ ions/cm²) by (a) SEM and (b) AFM.

5.4 Laser writing and photonic effects in Ga(AsN)

Two main processes can be envisaged to explain the laser-assisted dissociation of the N-H complex without invoking thermal effects: the photogenerated electron-hole pairs recombine non-radiatively and release their energy to the complex; or the complex directly absorbs the incoming photons and breaks-up if the photon energy is equal or larger than its dissociation energy. We examine the plausibility of these effects by studying the dependence of $|\Delta n_{\text{N-H}}|$ on the laser power density, p_a , and photon wavelength, λ (Figure 5.6). For the λ -dependence of the laser writing experiments, we used an Ar-laser ($\lambda = 515$ nm), a Ti:Sapphire laser ($\lambda = 695$ -830 nm), a He-Ne laser ($\lambda = 633$ nm) or a frequency-doubled Nd:YVO₄ laser ($\lambda = 532$ nm), exposure powers P_a up to 120 mW and times $t_a = 20$ s. Here the photon wavelength is tuned over a range of energies $h\nu = 1.49 - 2.41$ eV ($\lambda = 830 - 515$ nm), below and above the dissociation energy $E_A = 1.77 - 1.89$ eV ($\lambda = 700 - 656$ nm) of the N-H complexes responsible for the band gap increase in Ga(AsN).⁷ For each λ and p_a , we mapped the $\Delta n_{\text{N-H}}$ profile and estimated the value of $\Delta n_{\text{N-H}}$ at the center of each laser spot, $|\Delta n_{\text{N-H}}|_{\text{max}}$. From Figure 5.6, it can be seen that at each power the value of $|\Delta n_{\text{N-H}}|_{\text{max}}$ tends to peak at $h\nu = 1.76$ eV ($\lambda \sim 700$ nm), close to the reported values of E_A .⁷ Photoluminescence excitation measurements of both hydrogenated and untreated samples exclude the presence of specific resonances in the density of states of the crystal at the energy mentioned above. Thus data in Figure 5.6 suggest a resonant photon absorption by the N-H complex itself accompanied by its dissociation. Perhaps surprisingly, the phenomenon is also observed under laser photon energies that are significantly smaller than E_A . To explain this result, we envisage that the photogenerated electron-hole pairs can act to screen the N-H chemical bond, effectively reducing the dissociation energy of the complex. Similar

mechanisms were invoked to explain the light enhanced H-diffusion in amorphous Si¹³¹ and the photo-induced reactivation of neutralized donors in Si-doped GaAs.¹³² Data in Figure 5.6 also reveal a weak enhancement of $|\Delta n_{N-H}|_{\max}$ at photon excitation energies of $h\nu = 1.5\text{-}1.6$ eV, lower than the main peak. We tentatively attribute this feature to a lower energy bound for the dissociation of the di-hydrogen – nitrogen complex (N-H₂) by the formation of closely related complex states with a lower activation energy $E_A^* = E_A - 0.2$ eV.⁷¹

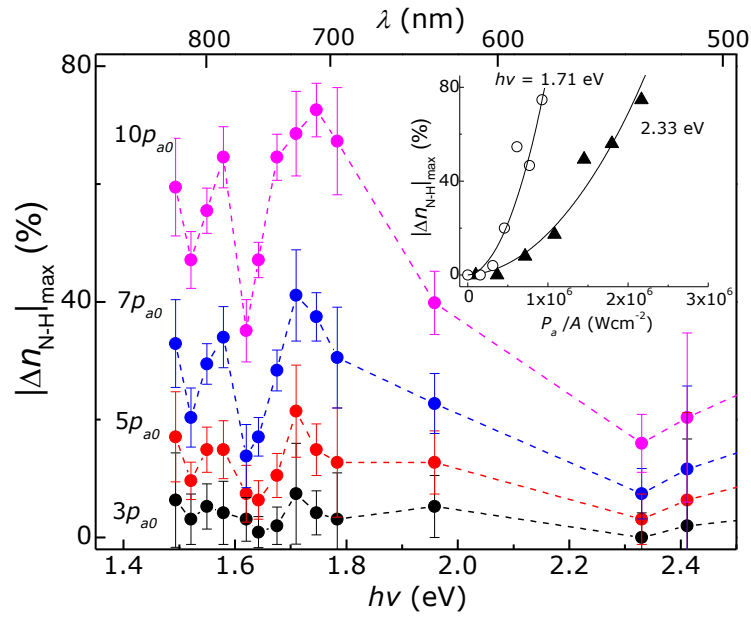


Figure 5.6. Dependence of the value of the $|\Delta n_{N-H}(X)|$ profile at the centre ($X = 0$) of the laser spot, $|\Delta n_{N-H}|_{\max}$, on the photon energy, $h\nu$, and laser wavelength, λ , at various power densities, p_a , and $t_a = 20$ s ($p_{a0} = 10^5$ Wcm⁻²). The inset shows the dependence of $|\Delta n_{N-H}|_{\max}$ on p_a at $\lambda = 725$ nm and 532 nm.

Plots of $|\Delta n_{N-H}|$ versus the laser power density indicate that at all laser wavelengths, the values of $|\Delta n_{N-H}|$ exhibit a non-linear dependence on power density, p_a (inset of Figure 5.6). This behavior could be consistent with a multi-photon absorption process, i.e. two photons are required to break the di-hydrogen – nitrogen complex (N-H₂) to fully restore the electronic activity of the N-atoms; also, this

could indicate a non-linear dependence of the screening action by the photogenerated carriers on the laser power. Theoretical models are required to assess these peculiar aspects of the N-H complex dissociation by photon excitation.

5.5 In-plane band gap profiling of Ga(AsN)

The dominant photonic nature of the laser-induced dissociation of the N-H complex at low laser powers implies that the size of the laser annealed spot is mainly limited by light diffraction, i.e. it is set by the laser spot diameter $d = 1.22\lambda/\text{NA}$, where $\text{NA} = 0.8$ (0.9) is the numerical aperture of our $\times 100$ objectives. For $\lambda = 515$ nm and 633 nm, this gives $d \sim 0.7$ - 0.8 μm and 0.9 - 1 μm , respectively, in good agreement with the measured $\Delta n_{\text{N-H}}(\text{X})$ profiles. Thus direct laser writing can provide a versatile tool for *in situ* in-plane band-gap engineering. Potential profiles of different shapes can be created and controlled with submicron spatial resolution and high energy accuracy (~ 1 meV) by adjusting the laser power and/or exposure time.

Figure 5.7a illustrates examples of spatial modulation of the Ga(AsN) QW PL peak energy, E_{QW} , obtained by scanning a laser beam over the surface of sample H2: triangular and step-like in-plane potential wells of given energy depth and spatial width are patterned in the XY plane of the QW. The specific annealing conditions used to create two of the potential profiles are illustrated in Figure 5.7b. Figure 5.7c shows different shaped light emitting areas produced by a focused laser beam ($\lambda = 532$ nm, $P_a = 20$ mW, and $t_a = 20$ s) on a hydrogenated Ga(AsN) epilayer with N-content, $x = 0.92\%$ at $T = 300$ K. Thermal annealing studies in a high temperature furnace show that the light emitting areas created by laser are stable up to temperatures $T_a \sim 200$ °C and that they can be erased at $T_a > 250$ °C due to the thermal dissociation of the N-H complexes and H-outgassing from the whole sample

(see Figure 5.7d). Thus the local dehydrogenation effect achieved by laser writing corresponds to temperatures that are considerable smaller than those required for thermal dissociation ($T_a > 200$ °C); this effect is erasable and the electronic properties of the Virgin (non-hydrogenated) QW can be fully restored by thermal annealing at $T_a > 200$ °C. The same sample can be re-hydrogenated making any nanoscale in-plane band gap profile rewritable.

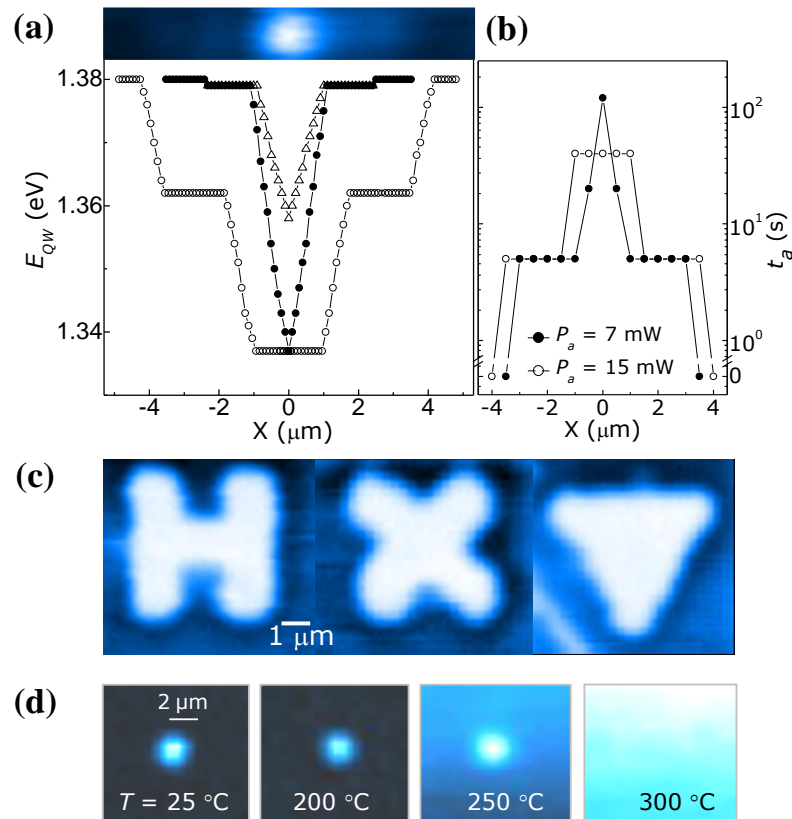


Figure 5.7. (a) Profiles of the QW PL peak energy, E_{QW} , created by laser writing in the hydrogenated Ga(AsN) QW (sample H2). The top figure is the μPL map corresponding to the triangular potential well (see triangles in the main Figure). (b) Annealing times and powers used for different profiles (triangular profile: full symbols; step-like profile: empty symbols). (c) μPL map of H, X and ∇ - shaped light emitting areas produced by a focused laser beam ($\lambda = 532$ nm, $P_a = 20$ mW, and $t_a = 20$ s) on a hydrogenated Ga(AsN) epilayer with N-content, $x = 0.92\%$. (d) Light emitting spots in sample H1 created by laser writing ($P_a = 20$ mW, $\lambda = 515$ nm and $t_a = 15$ s) and mapped following a 1-hour thermal annealing step for increasing temperatures $T_a = 200$ °C, 250 °C, and 300 °C.

5.6 Hydrogen containing (InGa)(AsN) and Ga(PN)

The laser-induced reversibility of hydrogen irradiation effects in other dilute nitride materials, such as (InGa)(AsN) and Ga(PN), were also investigated. Our experiments in the hydrogenated (InGa)(AsN) and Ga(PN) samples reveal effects that are qualitatively similar to those described for Ga(AsN), thus indicating a universal behaviour of hydrogenated dilute nitride alloys.

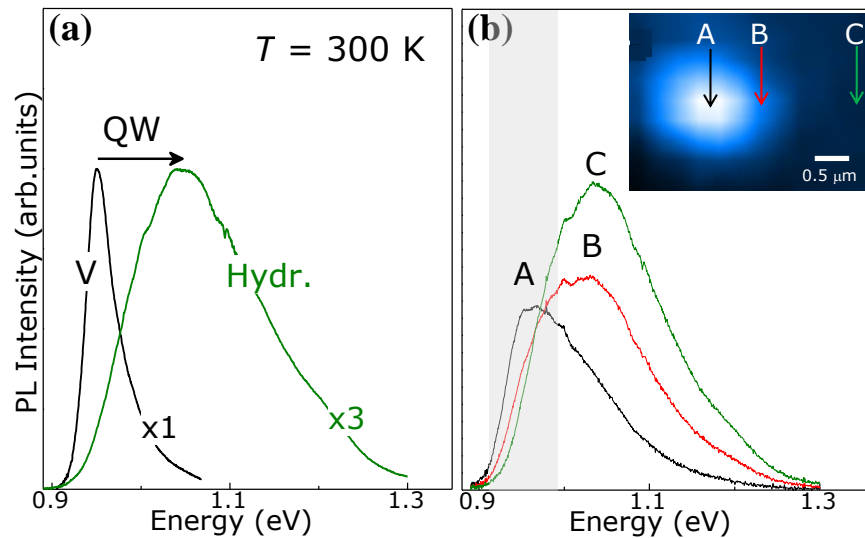


Figure 5.8. (a) μ PL spectra of the as-grown, V, and hydrogenated, Hydr., (InGa)(AsN) QW samples at $T = 300$ K. (b) μ PL map and μ PL spectra at positions A, B and C of an hydrogenated (InGa)(AsN) QW following laser writing at $T = 300$ K ($t_a = 20$ s, $P_a = 7$ mW, $\lambda = 532$ nm). The μ PL maps are obtained by plotting the μ PL intensity around $E = 0.9$ - 1 eV, corresponding to the energy range of the QW emission in the as-grown sample (see shaded area) and were acquired at low laser powers ($\lambda = 633$ nm, $P = 0.1$ mW, $T = 300$ K).

The incorporation of hydrogen ($d_H = 5 \times 10^{17}$ ions/cm² at $T_H = 300$ °C) in (InGa)(AsN) QW ([In] = 32% and [N] = 2.7%) neutralizes the electronic activity of nitrogen, thus causing a blue shift (~ 100 meV) of the QW PL emission, see Figure 5.8a. The PL linewidth broadens and the intensity drops upon hydrogenation indicating an increase of microscopic disorders and non-radiative centers. Figure 5.8b

shows the μ PL spectra of the hydrogenated (Hydr.) sample measured at low power (0.1 mW) after sample exposure to a focussed laser beam ($d < 1 \mu\text{m}$) of wavelength $\lambda = 532 \text{ nm}$ and power $P_a = 7 \text{ mW}$ for a time $t_a = 20 \text{ s}$. The laser exposure dissociates the N-H complexes thus red shifting the PL emission towards the emission of the as-grown (V) sample. It can be seen that the PL emission is peaked at lower energies in proximity of the spot centre.

Figure 5.9a shows the μ PL spectra of an as-grown and a hydrogenated Ga(PN) multi-quantum well (MQW) samples at $T = 10 \text{ K}$. Following the hydrogenation ($d_H = 8 \times 10^{18} \text{ ions/cm}^2$ at $T_H = 300 \text{ }^\circ\text{C}$) the PL emission blue shifts by $\sim 90 \text{ meV}$. The μ PL spectra and μ PL map for the Ga(PN) MQW following laser exposure to a focused laser beam with $\lambda = 532 \text{ nm}$ are shown in Figure 5.9b. It can be seen that the PL emission is peaked at lower energies in proximity of the spot centre. The increase of PL intensity induced by laser becomes more pronounced in the bulk Ga(PN) sample (inset of Figure 5.9b). The hydrogenated ($d_H = 7 \times 10^{18} \text{ ions/cm}^2$ at $T_H = 300 \text{ }^\circ\text{C}$) Ga(PN) bulk sample contains only a small concentration of N ($x = 0.15\%$) and the H-atoms act to fully neutralize the electronic activity of N, thus leading to a weak PL emission similar to that of Ga(PN) in the limit of very diluted N concentration ($x < 0.01\%$), where the recombination of excitons bound to single N-atoms dominates the spectrum (see inset of Figure 5.9b). Following the laser exposure, strong narrow emission lines can be clearly seen in the spectrum and are associated with carrier recombination from N-related complexes.¹³³⁻¹³⁴ Importantly, the N-H dissociation can be activated in our samples for laser photon wavelengths above ($\lambda = 532 \text{ nm}$) and below ($\lambda = 633 \text{ nm}$) the band gap absorption wavelength of GaP ($\lambda = 550 \text{ nm}$). This is in line with a direct photon absorption by the N-H complex, rather than a thermal effect.

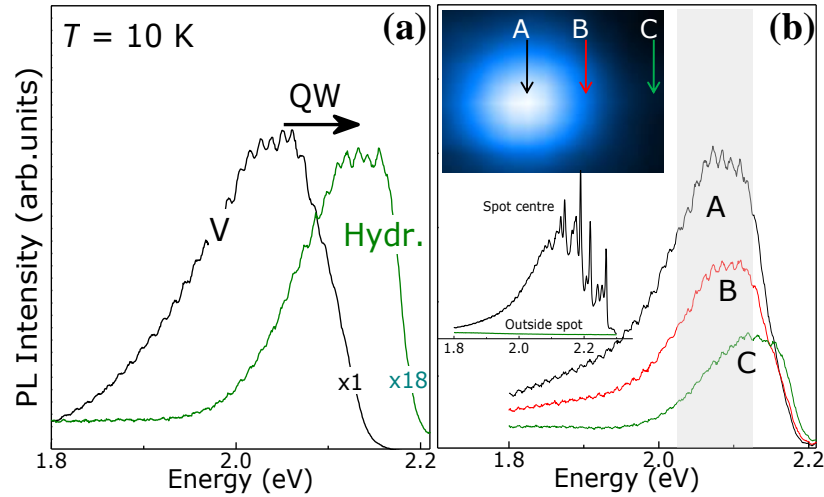


Figure 5.9. (a) μ PL spectra of the as-grown, V, and hydrogenated, Hydr., Ga(PN) MQW samples at $T = 10$ K. (b) μ PL map and μ PL spectra at positions A, B and C of an hydrogenated Ga(PN) MQW following laser writing at $T = 300$ K ($t_a = 20$ s, $P_a = 22$ mW, $\lambda = 532$ nm). The μ PL maps are obtained by plotting the μ PL intensity around $E = 2.0 - 2.15$ eV corresponding to the energy range of the MQW emission in the as-grown sample (see shaded area) and were acquired at low laser powers ($\lambda = 532$ nm, $P = 0.9$ mW, $T = 10$ K). The inset shows the μ PL spectra at $T = 20$ K of the Ga(PN) bulk sample inside and outside a typical laser spot created with $\lambda = 532$ nm.

5.7 Summary

In this work, we have shown that the laser-induced modification of the N-H bonds by micro-photoluminescence (μ PL) spectroscopy and mapping, and scanning electron microscopy. We demonstrated that the laser-assisted dissociation of the N-H complex in hydrogenated Ga(AsN) is enhanced at characteristic laser photon wavelengths ($\lambda \sim 700$ nm) corresponding to a resonant photon absorption by the N-H complex assisted by the photogenerated carriers. This is a local process that can be activated at temperatures that are significantly smaller than those (> 200 °C) required for thermal dissociation and provides a means of patterning with submicron spatial resolution in-plane band gap profiles of different shapes. Nanoscale light emitting spots in the visible and near infrared region are laser-activated in all the III-N-V

alloys (i.e. Ga(AsN), (InGa)(AsN) and Ga(PN)) investigated in this work. Since this direct laser writing technique does not require lithography and etching, it offers a promising route to cost-effective, large-volume and fast nanofabrication methods. The results are therefore of general interest and relevant to our current understanding of the physics and applications of N-H defects in III-Vs.

Chapter 6

Tunable spectral response by hydrogen irradiation of Ga(AsN) superlattice diodes

This chapter demonstrates how the spectral response of a Ga(AsN)/AlAs superlattice (SL) *p-i-n* diode can be tuned by *post-growth* hydrogen irradiation and thermal annealing. Our electroluminescence spectroscopy and photocurrent measurement probe the controlled diffusion of hydrogen and thermal dissociation of the N-H complexes of the SL. A focused laser beam is also used to diffuse hydrogen from the *p*-type GaAs layer towards the SL, thus creating a preferential path for the injection of carriers and activating a nanoscale light emitting region. The sample layer layout and *post-growth* H-irradiation conditions were described in section 4.1.2. The optical and electrical studies were performed by myself at the University of Nottingham. These results were published in *Applied Physics Letters* **104**, 242110 (2014).

6.1 Introduction

The nitrogen-induced band gap reduction in III-V semiconductor compounds^{41, 126} is a remarkable physical phenomenon in condensed matter physics and makes dilute nitride III-N-V alloys promising candidates for several applications, including nanophotonics¹⁶ and photovoltaics.¹ Of particular interest is the combined effect of nitrogen and hydrogen atoms on the electronic properties of a III-V compound. Hydrogenation combined with lithography and masking of an optically active dilute nitride III-N-V alloy has been used to fabricate ordered arrays of zero-dimensional nanostructures and site-controlled single photon emitters;^{16, 73} also, in the previous

chapter, I have shown how hydrogenation and laser writing of a III-N-V alloy provide a versatile top-down approach to a spatial profiling of the band gap energy.^{123, 135} In Chapter 5, the passivation of N by H and the dissociation of N-H complexes have been examined in III-N-V epilayers and quantum wells grown just below (< 100 nm) the surface. However, it was not implemented and demonstrated in a device structure where the active region is *deep* below the surface and embedded between doped contact layers. In this chapter, I demonstrate that the spectral response of a Ga(AsN)/AlAs superlattice (SL) *p-i-n* diode can be tuned by *post-growth* hydrogen irradiation and thermal annealing.

6.2 Room temperature electrical and optical studies

Our *p-i-n* diodes are based on Ga(AsN)/AlAs superlattices (SLs) with N-content, $x = 0\%$, 0.35% , 0.6% and 0.85% . Room temperature ($T = 300$ K) forward bias *I-V* characteristics show diode like behavior with an abrupt increase in the current for a bias voltage $V_d > 0.7$ V, see Figure 6.1a. One can notice that the V_d decreases monotonically with increasing N-content. This behavior is attributed to the presence of N that reduces the energy of the lowest conduction miniband thus reducing the bias required for injection of electrons into the SL from the *n*-type GaAs contact layer.¹²⁶ The room temperature EL measurements also show that the EL emission from the SL, X_1 , red shifts with increasing N-content, x , due to the band bowing effect (see Figure 6.1b-c). For $x = 0\%$, the EL spectrum shows a strong broad GaAs emission, EL_{GaAs} , from the depleted region on each side of the SL (see Figure 6.2a) and a very weak SL band emission, X_1 . However, for $x > 0\%$, the EL spectrum is dominated by the emission from the SL. In all our samples, the EL intensity increases with increasing current. One can notice that the overall EL

intensity decreases with increasing x (see Figure 6.1b-c). This is attributed to the reduced transmission of electrons in the SL that results from the increase of the electron effective mass and hybridization between the highly localized N level and the conduction band states of GaAs.¹³⁶

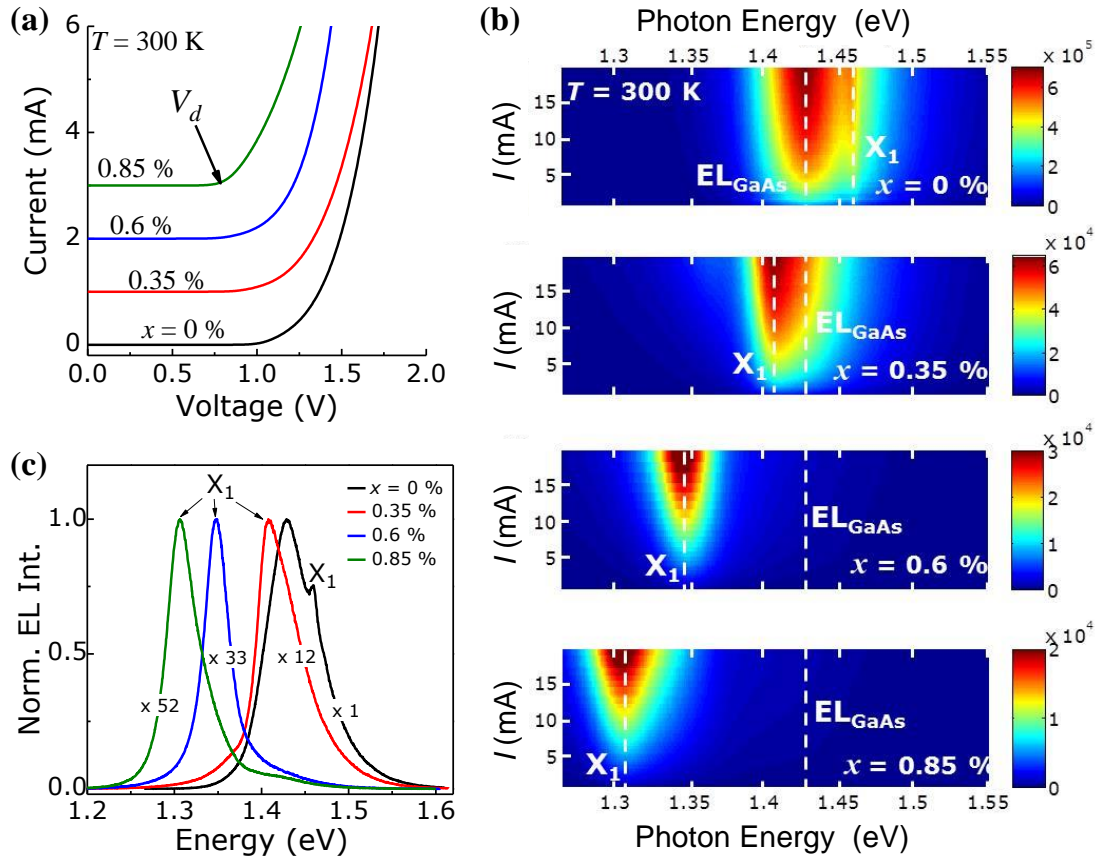


Figure 6.1: (a) Forward bias I - V characteristics at $T = 300$ K. For clarity, the curves are offset along the vertical axis. (b) Colour maps of the EL emission intensity vs current and photon energy at $T = 300$ K. (c) EL spectra at $I = 8$ mA and $T = 300$ K for our Ga(AsN)/AlAs SLs.

Figure 6.2b shows the room temperature ($T = 300$ K) PC spectrum at $V = 0$ V of a Ga(AsN)/AlAs SL diode with $x = 0.85\%$; see top black curve in the figure. The spectrum shows a broad excitonic absorption band, X₁, centred at ~ 1.32 eV. This is attributed to the lowest energy interband optical transition from the hole to the electron energy minibands of the SL. Following H-irradiation of the diode ($d_H =$

1×10^{18} ions/cm² at $T_H = 300$ °C), the intensity of the X₁-band decreases by a factor of 10 while a stronger PC absorption is observed at $h\nu > 1.4$ eV, with a feature centered at ~ 1.45 eV (see red dashed curve in the figure), close to the energy of the X₁ band in the control sample, *i.e.* an as grown GaAs/AlAs SL; see bottom black curve in the figure. The H-induced change of the PC spectrum was observed in all our SLs. As illustrated in Figure 6.2c, the peak energy of the X₁-band in the Virgin samples is well described by a Kronig-Penney model of the SL.¹³⁷ Following the hydrogenation, the photocurrent spectra of all samples show very similar shape with the peak energy of the X₁-band corresponding to that of the as grown GaAs/AlAs SL.

Our Kronig-Penney model includes the x -dependence of the band gap energy and of the electron effective mass for bulk Ga(AsN), which we estimate using a two-level band-anticrossing model with a N-level located at 0.23 eV above the conduction band minimum of GaAs at $T = 300$ K and an interaction parameter $C_{NM} = 2.7$ eV.¹²⁶ We have instead neglected the exciton binding energy, which represents a small correction to the calculated energies, and the effect of strain on valence band and the heavy hole effective mass, which we have assumed equal to that in GaAs ($m_{hh}^* = 0.34 m_0$, where m_0 is the electron mass in vacuum).⁹³ For the GaAs/AlAs interface, we have also used conduction and valence band offsets of $\Delta E_c = 0.96$ eV and $\Delta E_v = 0.64$ eV, respectively.¹⁰⁸ Details of the calculation are in section 3.2.2.1.

Our data suggest that hydrogen is incorporated well below the top GaAs p -type contact layer (> 500 nm) into the intrinsic SL region of the diode where it neutralizes the electronic activity of nitrogen atoms thus restoring the pristine properties of the GaAs/AlAs SL. It is important to point out, however, that this effect is likely to be non-uniform across the 10-period SL (total length 111 nm, see Figure 6.2a) where both nitrogen and nitrogen-induced crystal defects act to slow down the diffusion of

hydrogen into the deepest wells of the SL. Indeed, in the hydrogenated samples we observe a residual, weak low-energy PC absorption at the energy of the X_1 -band of the Virgin sample; see for example the feature at ~ 1.32 eV on the PC spectrum of the hydrogenated Ga(AsN)/AlAs SL in Figure 6.2b. Post-growth hydrogenation also induces a general increase in the intensity of the EL and PL emission (by a factor of > 2) thus indicating that hydrogen has also a beneficial effect on the optical quality of the Ga(AsN)/AlAs SL by passivating non-radiative recombination centers.

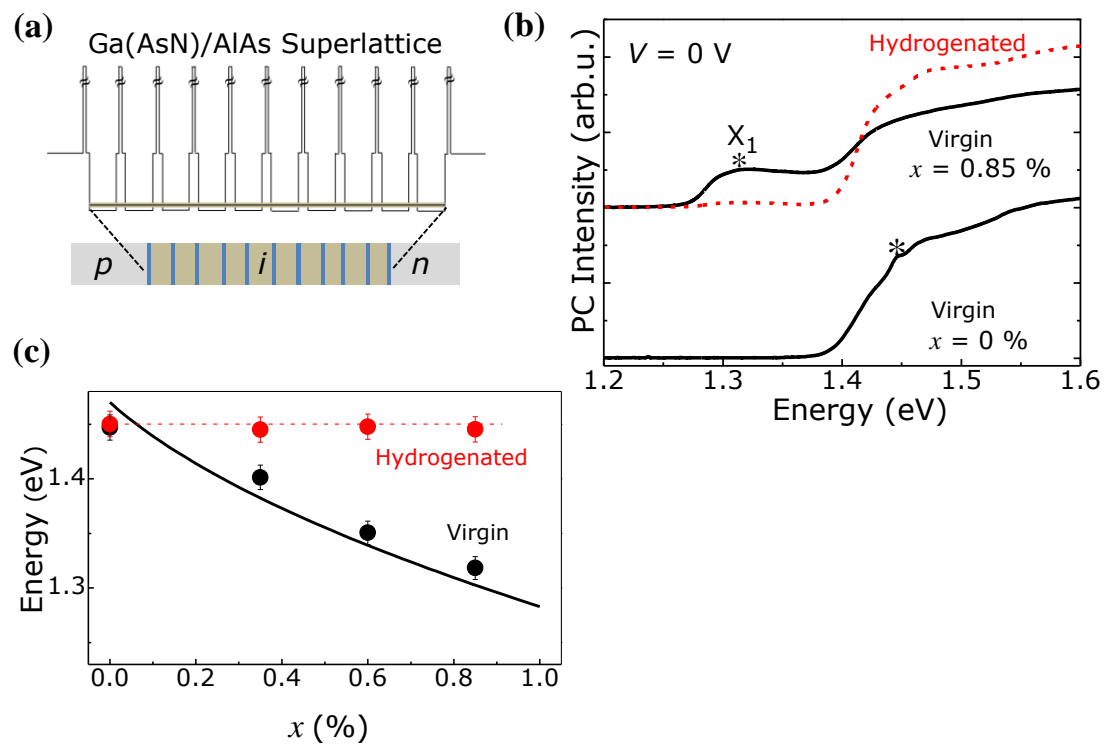


Figure 6.2. (a) Conduction band profile for a $p-i-n$ diode based on a Ga(AsN)/AlAs SL with $x = 0.85\%$ at $T = 300$ K. (b) PC spectra of the Virgin ($x = 0$ and 0.85%) and hydrogenated ($x = 0.85\%$, $d_H = 1 \times 10^{18}$ ions/cm 2 ; $T_H = 300$ °C) Ga(AsN)/AlAs SLs at $T = 300$ K and $V = 0$ V. The excitonic PC peak, X_1 , is indicated with an asterisk. For clarity, the PC spectra are offset along the vertical axis. (c) Measured (full dots) and calculated (continuous line) values of the energy of the X_1 -band in the Virgin and hydrogenated SLs versus N-content, x . The horizontal dotted line is a guide to the eye.

6.3 Low temperature optical studies

Figure 6.3a shows the low temperature ($T = 4.2$ K) PC absorption spectrum at $V = 0$ V of the Ga(AsN)/AlAs SL with $x = 0.6\%$. The spectrum shows a broad excitonic absorption band, X_1 , centred at ~ 1.44 eV. Following the hydrogenation ($d_H = 1 \times 10^{18}$ ions/cm² at $T_H = 300$ °C), the intensity of the X_1 -band decreases by a factor of 2 while a strong PC absorption is observed at $h\nu > 1.5$ eV, with a feature centred at ~ 1.56 eV, close to the energy of the X_1 -band in the control sample, *i.e.* an as grown GaAs/AlAs SL. Following the H-irradiation, the photocurrent spectra of all samples show very similar shape with the peak energy of the X_1 -band corresponding to that of the as grown GaAs/AlAs SL.

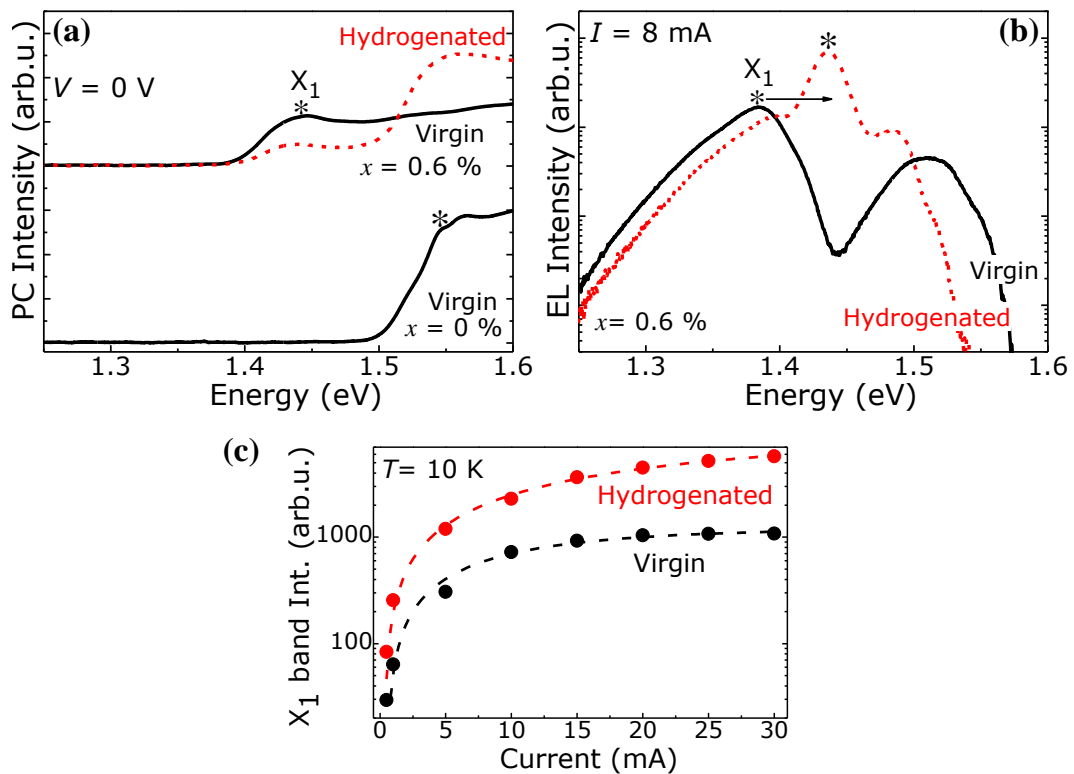


Figure 6.3: (a) PC spectra of the Virgin ($x = 0$ and 0.6%) and hydrogenated ($x = 0.6\%$, $d_H = 1 \times 10^{18}$ ions/cm²; $T_H = 300$ °C) Ga(AsN)/AlAs SLs at $T = 4.2$ K and $V = 0$ V. The excitonic PC peak, X_1 , is indicated with an asterisk. For clarity, the PC spectra are offset along the vertical axis. (b) EL spectra at $I = 8$ mA and (c) dependence of the peak EL intensity of the X_1 -band on current for the Virgin and hydrogenated Ga(AsN)/AlAs SLs with $x = 0.6\%$ at $T = 10$ K.

The low temperature ($T = 10$ K) EL spectrum also show that the overall EL emission intensity increases by tenfold thus indicating an improvement of the quantum efficiency by hydrogen incorporation, see Figure 6.3b. The blue shift of the SL band emission, X_1 , by 51 meV at $I = 8$ mA and $T = 10$ K, also suggests a possible neutralization of the N-electronic activity by hydrogen. The current dependence of the X_1 -band emission intensity for the Virgin and hydrogenated SLs with $x = 0.6\%$ is shown in Figure 6.3c. The difference in the intensity of the X_1 -band emissions between the hydrogenated and the Virgin sample considerably increases with increasing current.

6.4 Controlled thermal dissociation of N-H complexes

The incorporation of H into the SL and the H-induced neutralization of the nitrogen electronic activity provide us with a platform for the spectral tuning of the SL by the controlled thermal dissociation of the N-H complexes. This is shown in Figure 6.4a, where we plot a series of PC spectra for a hydrogenated ($d_H = 1 \times 10^{18}$ ions/cm²) Ga(AsN)/AlAs SL with $x = 0.85\%$, each spectrum measured after 1-hour step thermal annealing treatments at increasing temperatures T_a . It can be seen that an increasing T_a from 523 K to 603 K (250 °C to 330 °C) induces a systematic red-shift of the X_1 -band. This is paralleled by a corresponding red-shift of the room temperature EL emission from the SL (Figure 6.4b). The energy of the emitting and absorbing regions of the SL diode can also be tuned by the annealing time t_a for a given temperature T_a . Figure 6.5a-b shows the PC and EL spectra before and after each thermal annealing at $T_a = 573$ K (300 °C) for a hydrogenated ($d_H = 3 \times 10^{18}$ ions/cm²) Ga(AsN)/AlAs SL with $x = 0.6\%$. With increasing t_a , the peak energy of the X_1 -band shifts to lower energies towards the value it has in the Virgin sample.

The thermal annealing promotes also a deeper penetration of hydrogen across the SL, thus leading to narrower spectral features in EL and PC (see Figure 6.4). Since the EL intensity is not significantly changed by the thermal annealing, the beneficial effect of hydrogen in passivating crystal defects is also preserved, thus indicating that the activation energy for breaking the N-H complex is smaller than that required to reactivate non-radiative recombination centers.

We use the peak energy position of the X_1 -band in PC spectra and the Kronig-Penney model of the SL to estimate the concentration of N-H complexes at each annealing temperature and time. This is expressed as

$$n_{\text{N-H}}(T_a, t_a) = x - x_{\text{eff}}(T_a, t_a), \quad (6.1)$$

where x is the N concentration in the Virgin sample and $x_{\text{eff}}(T_a, t_a)$ is the concentration of N-atoms not neutralized by H in the hydrogenated sample. As shown in Figure 6.4c and 6.5c, the estimated value of $n_{\text{N-H}}(T_a, t_a)$ decreases with increasing T_a (Figure 6.4c) or t_a (Figure 6.5c).

If we assume that the N-H complex dissociate irreversibly during the thermal annealing, then the rate of change of $n_{\text{N-H}}$ can be expressed as¹³⁸

$$\frac{dn_{\text{N-H}}}{dt} = -Kn_{\text{N-H}}, \quad (6.2)$$

where $K = v \exp\left(-\frac{E_a}{k_B T_a}\right)$, E_a is the activation energy for the dissociation of the N-H complexes, and v is the attempt frequency for bond breaking. Thus in steady state $n_{\text{N-H}}(T_a, t_a)$ is given by¹³⁹

$$n_{\text{N-H}}(T_a, t_a) = n_0 \exp\left[-t_a v \exp\left(-\frac{E_a}{k_B T_a}\right)\right], \quad (6.3)$$

where n_0 is the concentration of N-H bonds in the SL previous to the thermal annealing.

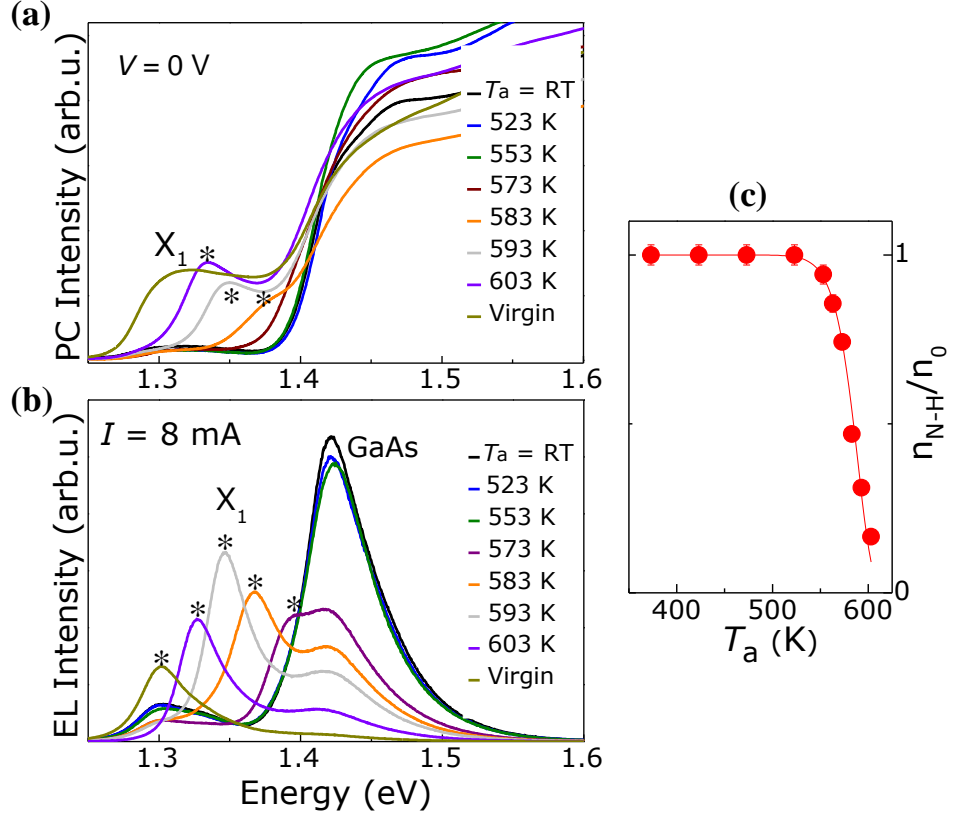


Figure 6.4. PC spectra at $V = 0$ V (a) and EL spectra at $I = 8$ mA (b) for a hydrogenated ($d_H = 1 \times 10^{18}$ ions/cm²; $T_H = 300$ °C) Ga(AsN)/AlAs SL with $x = 0.85\%$ ($T = 300$ K). Spectra were measured following a 1-hour thermal annealing step for increasing temperatures T_a . (c) Dependence of n_{N-H}/n_0 on T_a . The continuous line is a guide to the eye.

As shown in Figure 6.5c, the measured value of $n_{N-H}(T_a, t_a)/n_0$ decreases with increasing t_a , but tends to saturate to a constant value of 0.12 at large t_a , thus suggesting the existence of a small concentration of H-related complexes that does not dissociate due to a higher activation energy. Hence to fit the data of n_{N-H}/n_0 versus t_a , we use equation (6.3) by taking into account an additional constant term. Using for the attempt frequency ν the value of 3 THz from Ref. [7], we find that $E_a = 1.86 \pm 0.02$ eV. This value agrees very well with the activation energy for the N-H complex dissociation ($E_a = 1.89 \pm 0.02$ eV) previously obtained for Ga(AsN).⁷ An

activation energy of 2.04 ± 0.02 eV is obtained, instead, by assuming for the attempt frequency the value (93 THz) of the N-H vibrational mode in Ga(AsN).¹⁴⁰

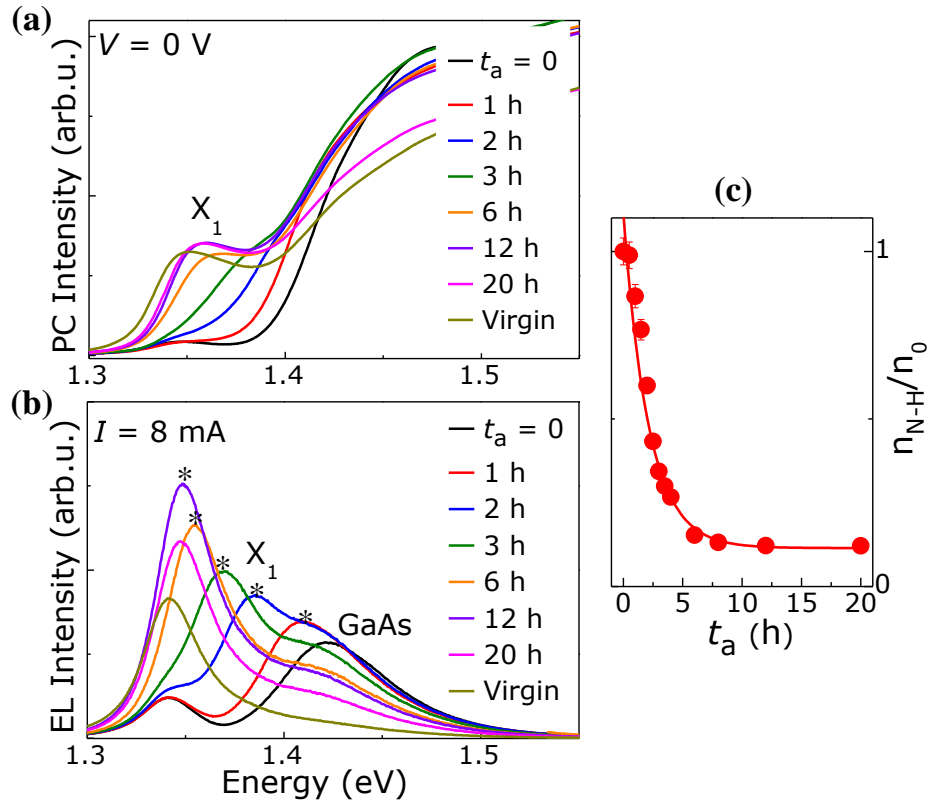


Figure 6.5. PC spectra at $V = 0$ V (a) and EL spectra at $I = 8$ mA (b) for a hydrogenated ($d_H = 3 \times 10^{18}$ ions/cm²; $T_H = 300$ °C) Ga(AsN)/AlAs SL with $x = 0.6\%$ ($T = 300$ K). Spectra were measured following a thermal annealing at $T_a = 573$ K (300 °C) at different times t_a . (c) Dependence of n_{N-H}/n_0 on t_a . The continuous line is the fit to the data by equation (6.3) modified by a constant and with $\nu = 3$ THz.

6.5 Photo-stimulated diffusion of hydrogen

The *post-growth* hydrogenation and thermal annealing of a diode therefore provides an effective route for controlling the light absorption and emission of the SL. Additional versatility is enabled by the photo-stimulated diffusion of H in the *p*-type layer with a focused laser beam. A laser writing technique was used before to control the diffusion of mobile interstitial manganese (Mn_i) donor ions out of the ferromagnetic semiconductor (GaMn)As towards the underlying layers of a quantum

well (QW) heterostructure.¹⁴¹ By annealing a sub-micron spot with a focussed laser beam it was possible to modify the local electrostatic potential in the QW plane and create a preferential path for charged carriers thus producing a nanoscale light emitting region.¹⁴¹ Here we show that a similar result can be obtained by using atomic hydrogen, which can occupy different lattice sites and exist in different charged states in GaAs.⁵⁵

Figure 6.6a shows the μ EL spectrum of the hydrogenated ($d_H = 1 \times 10^{18}$ ions/cm²) Ga(AsN)/AlAs SL with $x = 0.6\%$, measured at $V = 1.55$ V ($I = 8$ mA) and $T = 10$ K inside and outside an area exposed to a focused laser beam ($d \sim 1$ μ m) of wavelength $\lambda = 532$ nm for a time $t_a = 20$ s and power $P_a = 40$ mW. It can be seen that the effect of the laser exposure is to increase the EL intensity of the X_1 -band by more than a factor of 10. A typical laser exposed spot can be also resolved in the μ EL map in Figure 6.6b. The EL intensity distribution inside the spot has an approximately Gaussian form with a full width at half maximum that corresponds closely to the size of the laser spot diameter (~ 1 μ m). Similar μ EL spectra and maps were observed in several hydrogenated samples under similar laser exposure conditions. Since the intensity of the μ PL of the laser exposed spot is not significantly changed, we suggest that the focussed laser beam acts to promote the diffusion of the hydrogen atoms from the p -type GaAs layer towards the SL thus creating a preferential path for the injection of the charged carriers into the SL region. The bright light emitting spot of the diode can be observed for temperatures up to $T \sim 200$ K (Figure 6.6b). The temperature dependence of the ratio of the EL intensities within (I_i) and outside (I_o) the laser annealed spot (Figure 6.6c) shows a thermally activated behavior described by $I_i/I_o \sim \exp(-E_a/k_B T)$, where $E_a = 21$ meV is a characteristic activation energy. Most likely, the injection of carriers into the SL

takes place through states dripping from the conduction and valence band into the energy gap because of the deformation, chemical, and charge effects arising from the H interaction with the GaAs lattice.⁵⁵

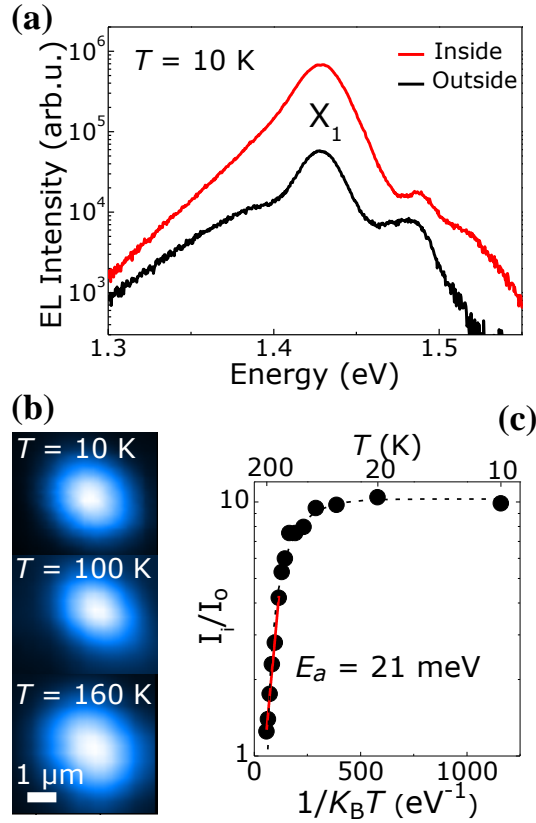


Figure 6.6. (a) μ EL spectra inside and outside a spot exposed to a focused laser beam ($\lambda = 532$ nm, $P_a = 40$ mW and $t_a = 20$ s) for a hydrogenated ($d_H = 1 \times 10^{18}$ ions/cm²; $T_H = 300$ °C) Ga(AsN)/AlAs SL with $x = 0.6\%$ ($I = 8$ mA and $T = 10$ K). (b) μ EL maps at $T = 10$ K, 100 K and 160 K of the laser annealed spot. (c) Temperature dependence of the ratio, I_i/I_o , of the EL intensities within and outside the light emitting spot. The continuous line is a fit to the data using $I_i/I_o \sim \exp(-E_a/k_B T)$, where $E_a = 21$ meV.

Since hydrogen diffuses from the Be-doped GaAs p -type contact layer, the complex responsible for such states could be due to H atoms in bond center position between a Be-atom and a nearest neighbor As atom.¹⁴² For a bond center position of hydrogen, two energy levels due to the neutral and positive charged state of H were

predicted to arise at about 30 and 34 meV below the conduction band edge, whilst two additional levels were found to be above (+5 and +30 meV) the top of the valence band.⁵⁵ The binding energy of these H-induced states is close to the activation energy estimated from the temperature dependence study of the μ EL (Figure 6.6c). With increasing temperature the emission from the diode becomes more uniform, thus suggesting the thermal ionization of these H-induced localized states and the injection of carriers into the SL through non resonant injection paths. Also, the created bright light emitting spots are visible at low temperatures ($T \leq 200$ K) even after many thermal cycles, thus indicating a stable modification of the diode properties by the laser-driven formation of H-induced localized states.

The X_1 -band peak energy at the centre of the light emitting spot shows a non-monotonic (red-blue-red) shift with increasing temperature, see Figure 6.7a. The S-like shape temperature dependence of the X_1 -band peak energy is attributed to the compositional alloy disorder or strain modulation and carrier thermal distribution effects. At low temperature, when excitons have not sufficient thermal energy, $k_B T$, to overcome potential energy barriers, they get trapped in local energy minima.¹⁴³⁻¹⁴⁴ This phenomenon called exciton freeze-out is illustrated in Figure 6.7b; see top feature. With increasing temperature the excitons gain enough energy to overcome potential barriers and diffuse to neighbouring lower energy states. This migration could explain the red shift of the X_1 -band emission in the temperature range 10 K to 50 K. When the excitons gain adequate thermal energy to be excited to higher energy states (see the bottom feature in the figure), the X_1 -band emission blue shifts ($50 \text{ K} < T < 90 \text{ K}$). At about 90 K, the excitons become delocalized, and the energy of the X_1 -band emission tends to decrease with increasing temperature due to the band gap reduction.¹⁴⁴ The later effect is described by the Varshni equation

$$E_{g(T)} = E_{g(T=0\text{ K})} - \frac{\alpha T^2}{T + \beta}, \quad (6.4)$$

where $E_{g(T=0\text{ K})}$ is the band gap energy at $T = 0\text{ K}$, and α and β are fitting parameters.¹⁴⁴ The energy blue shift of the EL emission in the T -range 50 K to 90 K ($\sim 5\text{ meV}$) is comparable with the reported value (~ 5 to 10 meV) for Ga(AsN) epilayers with $x = 1\%$.¹⁴⁵

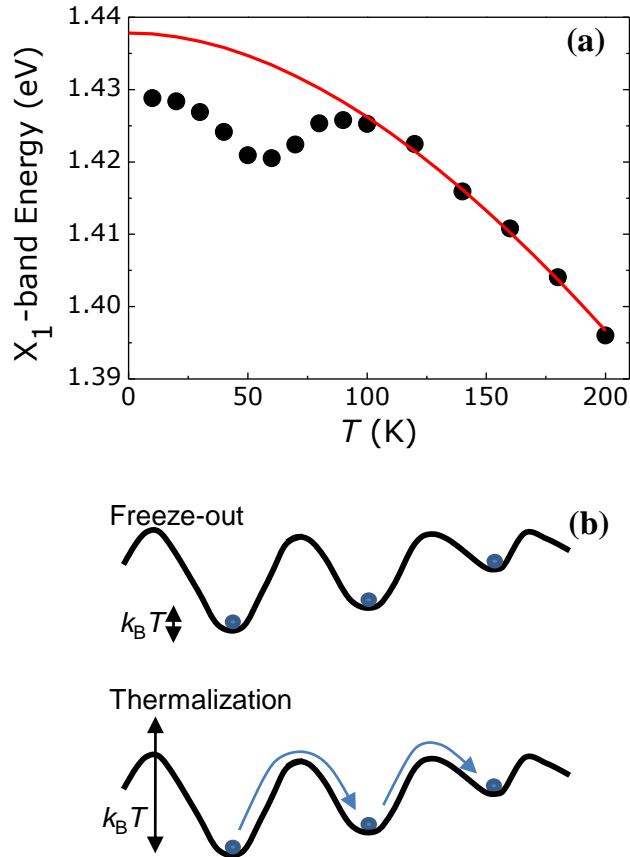


Figure 6.7. (a) Dependence of the X₁-band peak energy at the centre of a spot exposed to a focused laser beam ($\lambda = 532\text{ nm}$, $P_a = 40\text{ mW}$ and $t_a = 20\text{ s}$) for a hydrogenated ($d_H = 1 \times 10^{18}\text{ ions/cm}^2$; $T_H = 300\text{ }^\circ\text{C}$) Ga(AsN)/AlAs SL with $x = 0.6\%$ ($I = 8\text{ mA}$). Solid line is a fit to the data by Varshni law with $E_{g(T=0\text{ K})} = 1.438\text{ eV}$, $\alpha = 8.9 \times 10^{-4}\text{ eV/K}$ and $\beta = 667\text{ K}$ (b) Schematic diagram of exciton freeze-out (top feature) and thermal redistribution (bottom feature) in a disordered potential.

6.6 Summary

We have modified the electronic properties of *p-i-n* diodes based on Ga(AsN)/AlAs SLs by *post-growth* hydrogen irradiation. Hydrogen was successfully incorporated into the superlattice where it neutralizes the electronic activity of nitrogen by forming N-H complexes. We exploited the controlled thermal dissociation of the complexes to tune the energy of the SL photocurrent absorption and electroluminescence emission. A focused laser beam was also used to diffuse hydrogen from the *p*-type GaAs layer towards the SL. Near band-edge states created by this process provide preferential channels for the electrical injection of carriers into the SL and activate nanoscale light emitting regions. This method could be used for fabricating planar diode arrays¹⁴⁶ with distinct optical active regions, all integrated onto a single substrate.

Chapter 7

A movable resonant tunneling light emitting diode

In this chapter, we describe the realization of a movable micrometer-size light emitting area in a resonant tunneling LED (RT-LED) containing a GaAs/AlAs quantum well (QW). Our electroluminescence (EL) spectroscopy and mapping, I - V and C - V characteristics probe the hydrogen induced modification of the optical and electrical properties of the RT-LED. The sample layer layout and *post-growth* hydrogenation conditions were described in section 4.1.3. The optical and electrical studies were performed by myself and the theoretical modelling was done in collaboration with Dr. O. Makarovsky and Dr. G. Pettinari at the University of Nottingham. These results were published in *Applied Physics Letters* **103**, 241105 (2013).

7.1 Introduction

The ability to spatially localize^{141, 147–151} and move^{152–154} on a micrometer scale the emitting region in a light emitting diode (LED) is relevant for several applications including Lab-On-a-Chip experiments, bio-imaging, high-resolution micro-displays, optoelectronic integrated circuits, etc. A movable micrometer-size light emitting area has been achieved, recently, in organic LEDs (OLEDs) and transistors (OLETs).^{152–154} However, low quantum efficiencies and low carrier mobilities, typical of organic materials, often make necessary high applied voltages to generate spatially controlled light.^{152, 154} Temporal instabilities, low control on spatial profiles, and light quenching have also been observed.^{153–155} These drawbacks could be overcome in an inorganic LED, where the spatial control on a micrometer

scale of the light emitting area is therefore highly desirable. So far, micrometer- and nanometer-size light emitting areas have been created in inorganic LEDs by different approaches, including lithographic^{147–150} and laser-writing^{141,151} techniques. However, these approaches do not provide a means of moving spatially the light emitting area created. In this chapter, I demonstrate the realization of a bias controlled, micrometer-size movable light emitting area in an inorganic resonant tunneling LED (RT-LED) containing a GaAs/AlAs quantum well (QW).

7.2 Effect of hydrogen on transport properties

Following *post-growth* hydrogen implantation of the diode by a Kaufman source, we are able to modify the resistivity of the *p*-type GaAs layer exposed to hydrogen without affecting the *I-V* curve, which preserves its main resonant features. Resistance and capacitance measurements indicate that the *p*-type resistivity increases by increasing the implanted hydrogen dose and/or the hydrogenation temperature. In particular, the capacitance decreases by a factor of two upon an hydrogen treatment at $T_H = 250$ °C with a total H-impinging dose of $d_H = 1 \times 10^{19}$ ions/cm², see Figure 7.1a. We know that hydrogen cannot diffuse through the Ti/Au metal contact, thus the hydrogen is implanted only in the region which is not protected by the metal contact (see the inset of Figure 7.1b). For the hydrogenated mesa the effective capacitance can be described in terms of two parallel capacitors C_1 and C_2 each with an area equal to the area of the device beneath the contact, $A/2$, and that outside, $A/2$, respectively. Thus we estimate that the depletion region D in the hydrogenated mesa can be expressed in terms of the capacitance of the hydrogenated and Virgin mesas according to

$$D = \frac{A\epsilon_0\epsilon_r}{(2C_{Hydr} - C_{Virgin})}, \quad (7.1)$$

were ϵ_r is the relative permittivity of GaAs ($\epsilon_r = 12.85$)¹²⁸ and A is the area of the mesa. As can be seen in Figure 7.1, the capacitance measurements indicate a significant increase of the depletion region width, D , following the hydrogenation ($d_H = 1 \times 10^{19}$ ions/cm² and $T_H = 250$ °C).

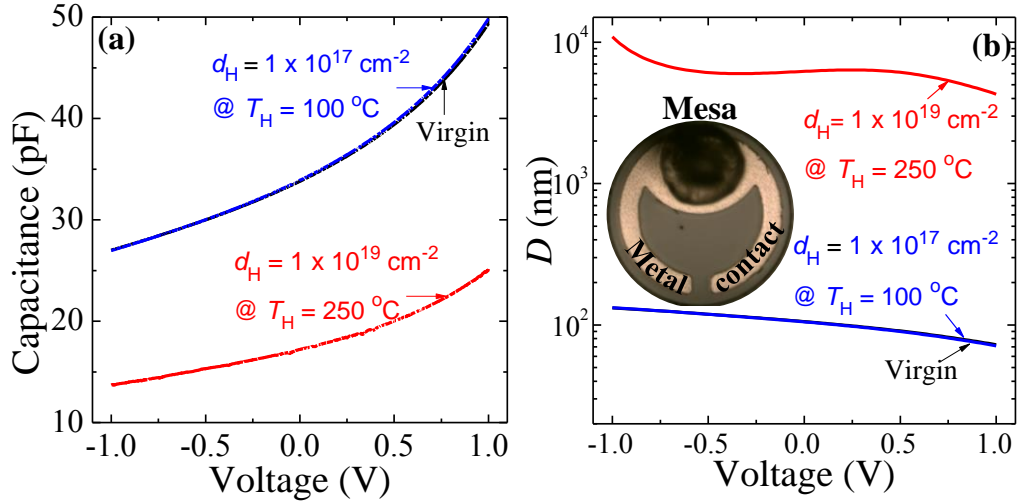


Figure 7.1: Applied bias dependence of the (a) capacitance and (b) depletion region, D , of an RT-LED for different hydrogenation conditions ($d_H = 1 \times 10^{17}$ ions/cm² and $T_H = 100$ °C, $d_H = 1 \times 10^{19}$ ions/cm² and $T_H = 250$ °C). The inset shows the optical image of a 200 μm diameter mesa RT-LED.

7.3 Electroluminescence studies

Following the hydrogen treatment of the RT-LED (at $T_H = 250$ °C with $d_H = 1 \times 10^{19}$ ions/cm²), the low-temperature ($T = 9$ K) electroluminescence (EL) spectra exhibit a new emission, labeled as γ , at energies lower than those of the free exciton [FE, $E_{FE} \sim 1.515$ eV] and electron-carbon [(e,C), $E_{(e,C)} \sim 1.494$ eV] recombination in the GaAs contact and spacer layers; see Figure 7.2a-b. The γ -band can be clearly seen for $V < 1.45$ V. Under these bias conditions, the QW EL emission is not excited whilst the intensity of the FE and (e,C) recombinations in GaAs is relatively weak being generated by up-conversion mechanisms (Figure 7.2c). With increasing V , the emission energy of the γ -band blue-shifts up to saturate ($E_\gamma \sim 1.475$ eV) for biases

greater than the bias for flat-band conditions ($V_{\text{FB}} \sim 1.5$ V). The strong bias dependence of the γ -band emission energy is likely to be due to a band filling effect.

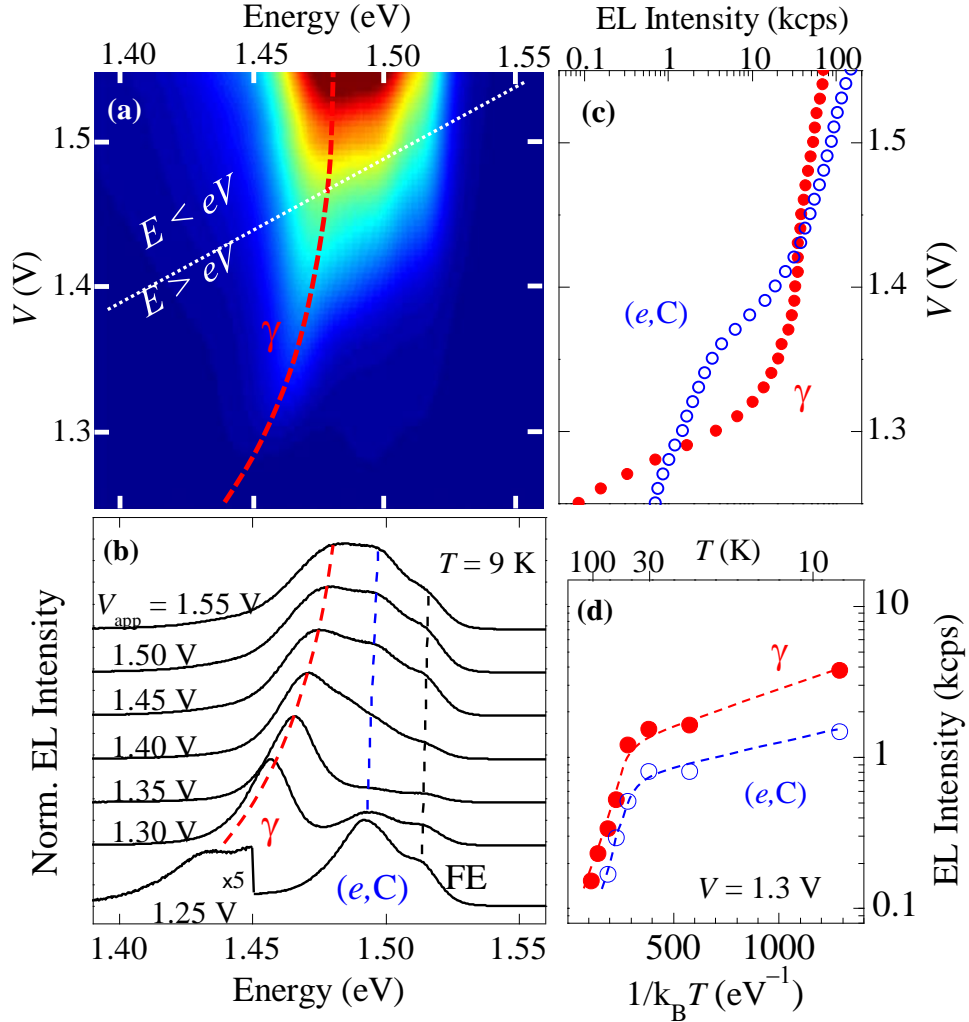


Figure 7.2: Hydrogen incorporation detected by electroluminescence. (a) Color map of the electroluminescence (EL) intensity versus applied voltage (V) and photon energy (E) recorded at $T = 9$ K on the hydrogenated ($d_{\text{H}} = 1 \times 10^{19}$ ions/cm 2 and $T_{\text{H}} = 250$ °C) sample. The white dotted line represents the condition $E = eV$. For $V < E/e$ the EL is generated by up-conversion. (b) Peak-normalized EL spectra for representative values of the applied bias at $T = 9$ K. The EL intensities of the γ -band (full points) and of the (e,C) recombination (circles) are shown in panel (c) as a function of the applied voltage at $T = 9$ K and in panel (d) as a function of temperature at $V = 1.3$ V. Dashed lines are guides to the eye.

A similar γ -band, peaked at ~ 1.455 eV, has been previously reported by M. Capizzi et al.,⁵⁶ by photoluminescence experiments in hydrogenated GaAs and attributed to a transition between localized states in the conduction and valence band associated with the local distortion of the lattice bonds when H binds to impurities (*e.g.*, C, Si, or Zn), defects, and lattice atoms. Thus, the appearance of the γ -band emission in our RT-LED devices treated with hydrogen provides independent optical evidence that under specific conditions, hydrogen is incorporated in the C-doped *p*-type GaAs contact layer where it can form C–H complexes. With increasing temperature, the γ -band loses intensity with a dependence similar to that of the (*e*,C) recombination (Figure 7.2d), as also found by Capizzi and co-workers.⁵⁶

7.4 Movable LED

In this section we show the realization of a bias-controlled movable light emitting area by *post-growth* H-irradiation of a RT-LED, see Figure 7.3. The low temperature ($T = 4.2$ K) current-voltage, *I-V*, characteristics of the untreated (Virgin) device is shown in Figure 7.3a. The *I-V* curve is dominated by a strong resonance due to tunneling of electrons into the lowest conduction subband (E1) of the QW and by much weaker resonances associated with tunneling of holes into the heavy-hole (HH1 and HH2) and light-hole (LH1) valence subbands of the QW (Figure 7.3a), as observed before in similar RT-LEDs.^{105, 156} Following the hydrogenation, the *I-V* preserves its main resonant features. In contrast, the resistivity of the *p*-contact layer increases by up to a factor of $\geq 10^4$ for $T_H = 250$ °C and $d_H = 1 \times 10^{19}$ ions/cm². These hydrogenation conditions also lead to a pronounced change in the spatial profile of the QW EL intensity in the hydrogenated devices.

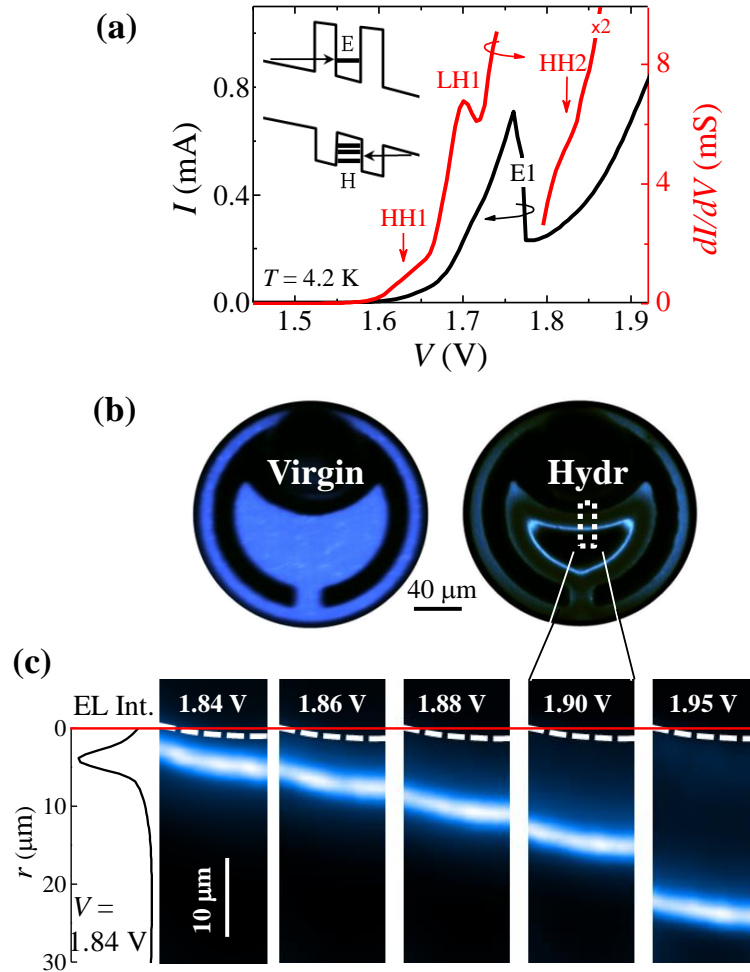


Figure 7.3: A movable light emitting area by *post-growth* hydrogenation of a resonant tunneling light emitting diode (RT-LED). (a) Current-voltage I - V characteristics of a Virgin 200 μm diameter mesa RT-LED at $T = 4.2$ K. This is dominated by a strong resonance due to tunneling of electrons into the E1 QW subband and by much weaker resonances –observed in the conductance dI/dV – due to tunneling of holes into the HH1, LH1, and HH2 QW subbands; see inset for a sketch of the carrier injection into the QW. (b) Digital camera images of the EL emission intensity (at $T = 9$ K and $V = 1.9$ V) before (Virgin) and after (Hydr) *post-growth* hydrogen incorporation. The images were acquired with a 800 nm short-pass filter to remove the contribution from the GaAs-related emission [(Multimedia view) [URL: <http://dx.doi.org/10.1063/1.4844975.1>]]. (c) Normalized EL maps for increasing values of the applied voltage, as obtained by plotting the EL intensity (at $T = 9$ K) around the QW emission energy ($E = 1.63$ eV). The dashed lines in the EL maps indicate the metal contact edge. The EL spatial profile is also shown for $V = 1.84$ V.

As shown in Figure 7.3b, before hydrogen incorporation, the QW EL intensity is uniform across the mesa diode, while after hydrogenation it is localized along a *ring*. The light emitting area has a Lorentzian spatial profile with a full-width at half-maximum (w) of $3.3 \pm 0.1 \mu\text{m}$ and moves linearly with increasing the applied voltage (Figure 7.3c).

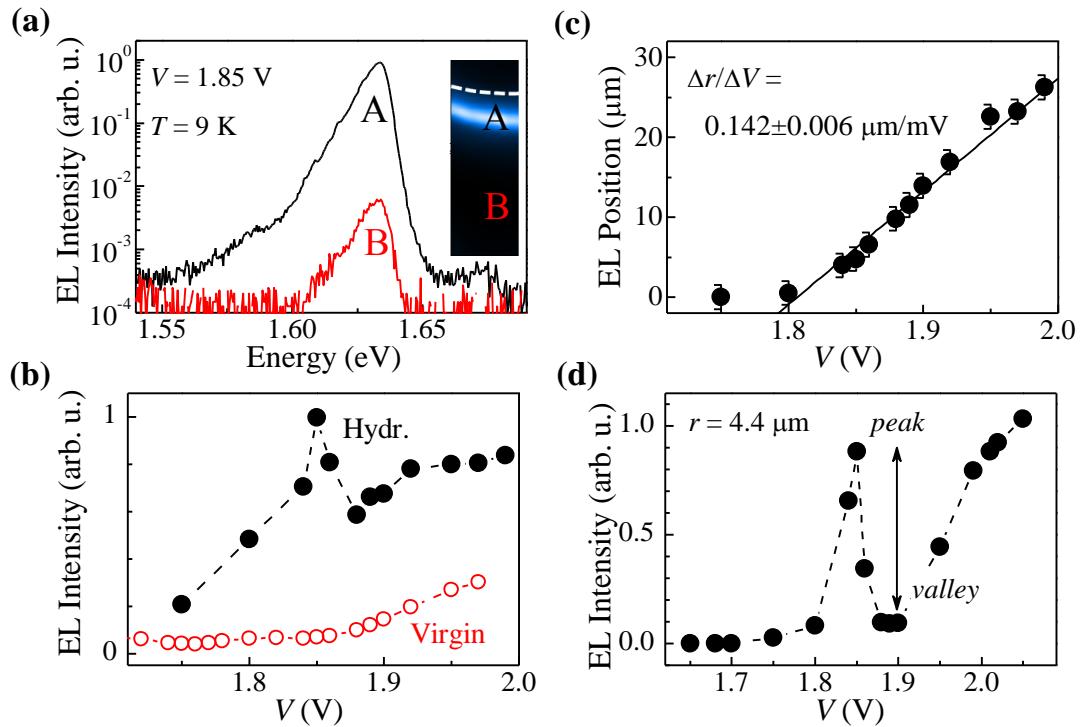


Figure 7.4: Properties of the movable RT-LED. (a) QW EL spectrum on the ring (position A in the EL map) and outside the ring (position B in the EL map) at a given applied voltage ($V = 1.85 \text{ V}$). (b) Comparison of the bias dependence of the QW EL intensity in the hydrogenated sample (at the ring) and in the Virgin sample (at the mesa center). In the Virgin sample the spatial inhomogeneity of the EL intensity is less than 4% and is independent on the applied voltage. (c) Position of the QW EL emission versus the applied voltage V : the light emitting area shifts linearly from the contact edge towards the mesa center. The continuous line is a linear fit to the data at $V \geq 1.8 \text{ V}$. (d) At a given position ($r = 4.4 \mu\text{m}$), the QW EL intensity versus the applied voltage shows a large peak-to-valley ratio (~ 10), much larger than the peak-to-valley ratio (~ 3) of the E1 peak in the current-voltage I - V characteristics (see Figure 7.3a).

We now consider in detail the characteristics of the movable RT-LEDs; see Figure 7.4. The QW EL intensity is significantly larger on the ring than outside the ring (Figure 7.4a) for each applied bias and position of the ring; the QW EL intensity on the ring is much stronger than that on the Virgin sample and is resonantly enhanced at a characteristic bias of $V \sim 1.85$ V (Figure 7.4b); also, with increasing voltage, its position r —measured radially from the metal contact edge on the mesa—shifts linearly from the contact towards the center of the mesa at a rate of $0.142 \mu\text{m mV}^{-1}$ and with a shift of up to $\sim 30 \mu\text{m}$ for a bias increment of 0.2 V (Figure 7.4c). Similar data were obtained in other mesa diodes.

7.5 Simultaneous resonant injection of electrons and holes

The non-uniform spatial profile of the EL intensity in the hydrogenated RT-LEDs indicates that the injection of carriers into the QW is non-uniform across the mesa. To interpret this finding, we first note that hydrogen is implanted in regions of the diode that are not protected by the metal contact. These are the regions providing optical access to the diode and where hydrogen tends to passivate the C-dopants in the p -type GaAs contact layer by forming C–H complexes.¹⁵⁷⁻¹⁵⁸ The H-induced C-dopant passivation results into an increase of the resistivity in the hydrogenated area and causes a lateral voltage drop from the metal contact edge ($r = 0$) towards the center of the mesa. Thus the resonant injection of electrons and holes into the QW subbands occurs at different positions for each applied bias; see Figure 7.5a.

To model the spatial dependence of the electron and hole injection into the QW, we consider the alignment of the Fermi energy in the n - and p -type GaAs contact layers with the electron and hole QW subbands, respectively. The hydrogen-induced passivation of C-dopants on the p -type layer results in an increase of the depletion region width, which is wider in the center of the mesa than beneath the

metal contact, where the p -type layer –not exposed to hydrogen– retains locally its pristine characteristic (see Figure 7.1b). To account for the lateral voltage drop across the mesa, we consider a simple model that neglects charge accumulation effects and assume a linear variation with r of the depletion width on the p -type side (*i.e.*, of the tunneling distance for holes, $D_h = D_h^0 + \alpha r$, where α is a constant) and a constant depletion region on the n -type side of the structure (*i.e.*, of the tunneling distance for electrons, $D_e = D_e^0$); see Figure 7.5b. The values of D_e and D_h at the contact edge, D_e^0 and D_h^0 , are assumed equal to the distances of the n - and p -type GaAs layers from the center of the QW (see inset in Figure 7.5b).

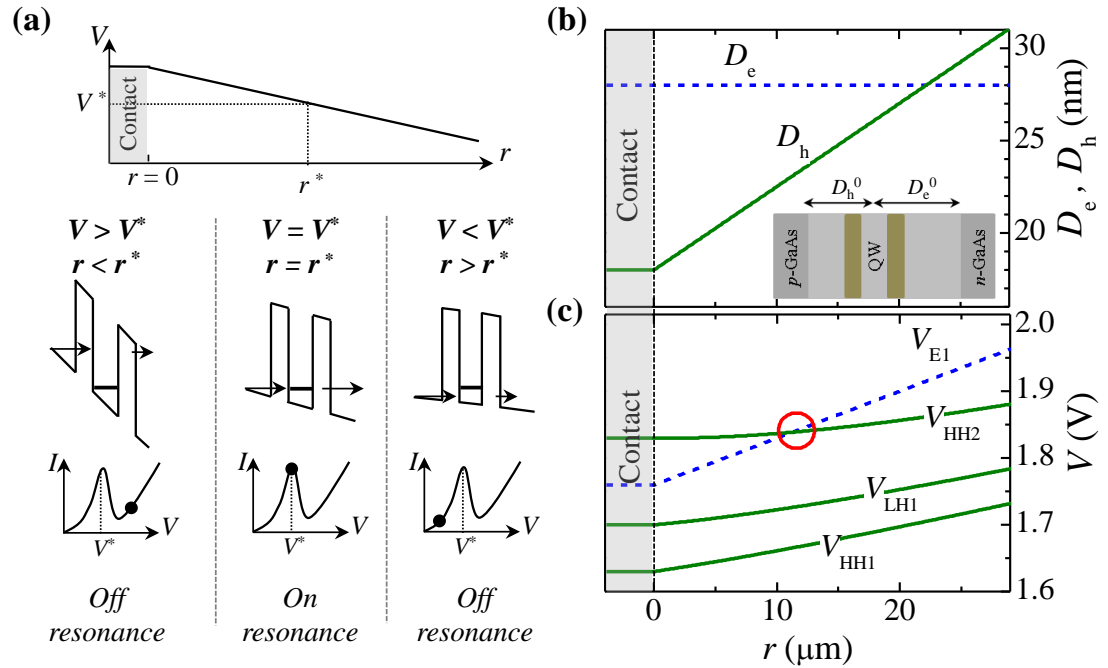


Figure 7.5: Modeling of the movable RT-LED. (a) Sketch of the spatial voltage drop along the mesa – r being the radial distance from the metal contact edge– induced by the hydrogen passivation of C-dopants in the p -type GaAs contact layer. This causes a spatial variation of the injection of carriers into the QW, with resonant injection occurring at a given position r^* . (b) Dependence on r of the electron (D_e) and hole (D_h) tunneling distances and (c) of the tunneling voltages for the resonant injection of electrons (V_{E1}) and holes (V_{HH1} , V_{LH1} , and V_{HH2}) into the subbands of the QW. The simultaneous resonant injection of electrons and holes into the QW is highlighted by a red circle.

The spatial variation of D_e and D_h across the mesa results in a spatial change of the voltages, ΔV_e and ΔV_h , dropped between the n - and p -type GaAs layers and the center of the QW, respectively. This is described by the electrostatic leverage factors for the conduction [$f_e = \Delta V_e/V = D_e/(D_e + D_h)$] and valence [$f_h = \Delta V_h/V = D_h/(D_e + D_h)$] bands. Using f_e and f_h , we can write simple expressions for the voltage required for the resonant injection of electrons [$V_{E1} = V_{FB}^0 + (V_{E1}^0 - V_{FB}^0)f_e^0/f_e + \beta r$] and holes [$V_H = V_{FB}^0 + (V_H^0 - V_{FB}^0)f_h^0/f_h + \beta r$] into the E1 and hole (H = HH1, LH1, HH2) subbands of the QW, respectively. Here $V_{FB}^0 = 1.51$ V is the bias required to reach flat bands at $r = 0$ and β is a constant accounting for the linear voltage drop across the mesa caused by the spread resistance on the p -type contact layer.

As shown in Figure 7.5c, for each applied bias V , the resonant tunneling of electrons and holes into the QW subbands occurs at different positions r . In particular, the voltage for tunneling of holes into the HH2 subband (V_{HH2}) crosses the voltage for electron tunneling into the E1 subband (V_{E1}); see red circle in the figure. The crossing point corresponds to the *simultaneous resonant injection* of electrons and holes in the QW. By using $\alpha = 0.45$ nm μm^{-1} and $\beta = 4.6$ mV μm^{-1} , the model indicates that an applied voltage $V \sim 1.84$ V is required to achieve simultaneous electron and holes resonant injection into the QW, thus accounting for the measured resonant enhancement of the QW EL intensity at $V = 1.85$ V, see Figure 7.4b. The calculated position at which the simultaneous resonant injection occurs ($r = 11.5$ μm) differs from the experimental value ($r = 4.4$ μm) by an amount that corresponds to the extrapolated value of the ring position ($r = -6.6$ μm , see Figure 7.4c) at the E1 tunneling voltage ($V_{E1}^0 = 1.76$ V). This offset is likely to originate from an additional contact voltage drop, from the experimental uncertainty in defining the contact edge position starting from the EL maps, and/or from the hydrogen diffusion beneath the

contact, all factors which have not been included in the model. Moreover, as the simultaneous resonant injection of carriers into the QW is satisfied under more stringent conditions than single charge resonant tunneling, the QW EL intensity versus the applied voltage is characterized by a peak-to-valley ratio (~ 10 , see Figure 7.4d) significantly larger than that (~ 3) observed under non-resonant conditions and of the peak-to-valley ratio (~ 3) for the E1 resonance in I - V (Figure 7.3a). The model also indicates that the measured linear spatial shift of the EL emission with the bias is dominated by the electron injection, *i.e.*, it follows the calculated r -dependence of V_{E1} , $[dV_{E1}(r)/dr]^{-1} = [\beta + \alpha(V_{E1}^0 - V_{FB}^0)/(D_e^0 + D_h^0)]^{-1} = 0.142 \mu\text{m mV}^{-1}$.

7.6 Simulation of the EL spatial map

The spatial distribution of the EL intensity is simulated using a simple model, which describes the EL in terms of the product of the electron (I_e) and hole (I_h) tunneling currents, as derived by fitting their contribution to the measured I - V characteristics of the Virgin sample (Figure 7.6a), and by assuming a linear drop of the applied voltage with the distance r from the metal contact edge. Thus, the voltage dependence of the tunneling currents is converted into a spatial dependence; see Figure 7.6b. At a given V , the EL (*i.e.*, $I_e \times I_h$) is peaked at the position where electrons tunnel resonantly into the E1 QW subband (Figure 7.6b). The two-dimensional spatial map of the EL intensity is obtained by projecting the spatial dependence of $I_e \times I_h$ in a plane (Figure 7.6c). As shown in Figure 7.6d-e, the simulations reproduce the formation of the ring and its shift with increasing V . Also, they indicate that the bias at which the *ring* forms at a given position corresponds to the condition for the resonant injection of electrons into the E1 subband of the QW at that position.

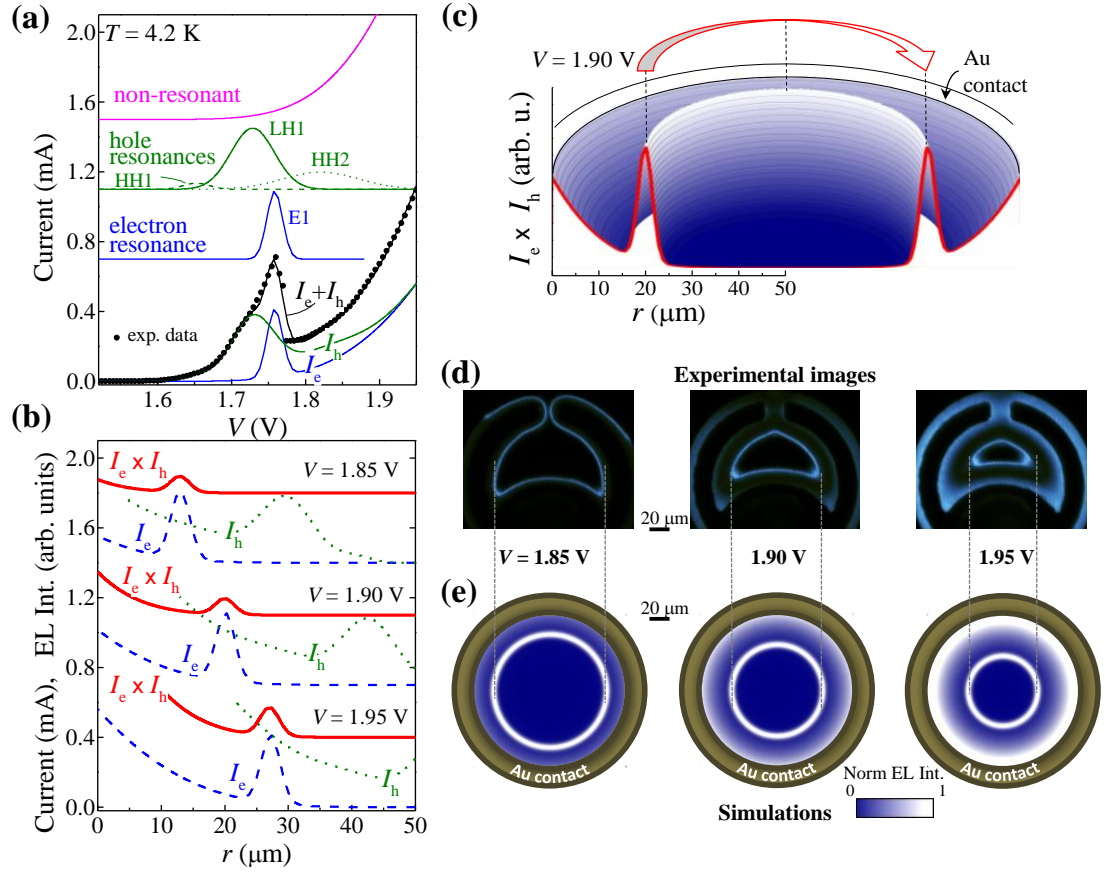


Figure 7.6. Simulation of the EL spatial map. (a) Experimental I - V characteristics at $T = 4.2$ K (full points) together with its electron (I_e) and hole (I_h) tunneling current components (bottommost solid lines), as obtained by a fitting procedure. For clarity, the different components to the fitting currents are shifted along the vertical axis. I_e (I_h) is obtained by adding the E1 (HH1, LH1, and HH2) resonant component(s) to half of the non-resonant component of I . The dependence of I_e , I_h , and EL intensity (*i.e.*, $I_e \times I_h$) on the distance r from the metal contact edge is shown in (b) for different values of V (vertically shifted for clarity). The two-dimensional spatial map of the EL intensity is obtained by projecting $I_e \times I_h$ into a circular space (c). The distance between the metal contact edge and the mesa center corresponds to the experimental value ($50 \mu\text{m}$). (d-e) Comparison between experimental EL maps (d) and simulated ones (e) for different values of the applied voltage.

The above approach simulates the condition of a perfectly circular metal contact, thus resulting in a difference in shape between the simulated light emitting area (circular) and the experimental one (given by the crescent-shaped metal

contact); see Figures 7.6d-e. Also, the simulations hold under the condition that the ring is large enough to neglect the interaction between currents flowing from opposite points of the mesa. These results in a deviation of the simulated ring size from the experimental one at large applied biases, $V > 1.95$ V (Figure 7.6d-e). We note that the ring formation and its evolution with increasing V do not depend on the specific assumption on the EL intensity, namely, the EL being proportional to $I_e \times I_h$, $I_e + I_h$, or I_e . Finally, similar results have been obtained by fitting the I - V characteristics of the hydrogenated sample, being the latter similar to the I - V of the Virgin sample except for a larger non-resonant component of the current.

7.7 Temperature dependent study

The effects described above are observed for temperatures up to $T = 100$ K. With increasing T , the ring becomes gradually less bright and broadens; see Figure 7.7. Also, the relative intensity of the QW emission with respect to that from the GaAs layer increases by more than a factor of 10 due to the thermal ionization of holes bound to C-acceptors. Indeed, the GaAs-related emission is dominated by the recombination of electrons with holes bound to neutral C-acceptors in the intrinsic and p -type contact layers. At $T = 80$ K the ring intensity is still 1/3 of the low temperature value, $w = 6.1 \pm 0.4$ μm , and the QW/GaAs EL intensity ratio is higher than a factor of 20. Thus this movable LED could also be used at liquid-nitrogen temperatures. As the temperature stability of the ring formation relies on the robustness of the resonant injection of carriers into the QW and on carrier thermal escape mechanisms, we envisage that optimization of the layer layout and/or the employment of a multi-barrier structure could make possible room temperature operation.¹⁵⁹⁻¹⁶⁰

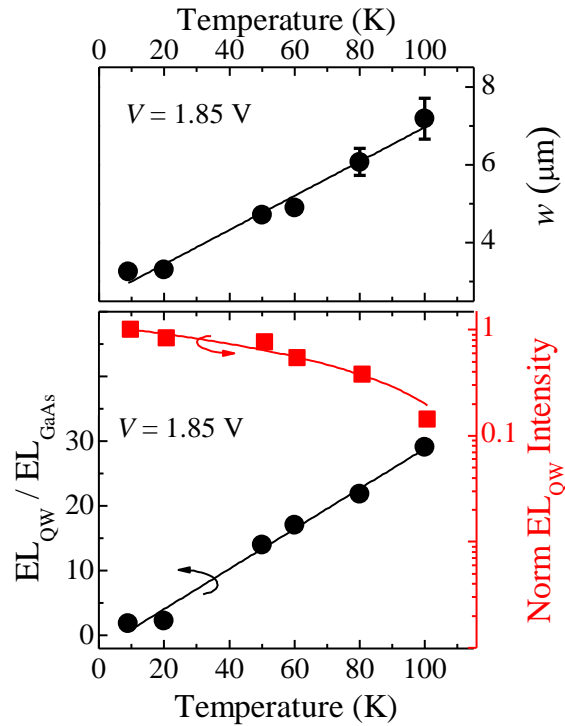


Figure 7.7: Temperature dependence studies of the movable RT-LED. Dependence on T of the width (w) and EL intensity (EL_{QW}) of the QW emission on the ring, and of the ratio between the QW and the GaAs-related EL intensities (EL_{QW}/EL_{GaAs}) at $V = 1.85$ V. Solid lines are linear fits to the data.

7.8 Summary

In this chapter, I have reported on the fabrication of a movable micrometer-size light emitting area in a solid state GaAs/AlAs-based RT-LED. Our approach exploits the resonant injection of charge carriers into the quantum states of the QW and the control of this process by *post-growth* hydrogen implantation. We have showed that the position of the QW electroluminescence (EL) can be spatially shifted by the applied voltage and that the bias condition for the resonant injection of electrons and holes into the bound states of the QW changes across the mesa. In turn, this can lead to simultaneous resonant tunneling of electrons and holes at specific positions of the mesa diode, thus leading to a tenfold increase of the local EL intensity. As several innovative device concepts in emerging nanotechnologies exploit the quantum

tunneling of charge carriers into a quantum state, our approach could be extended to other applications of resonant tunneling that span from optoelectronic integrated circuits^{104, 161} to electrically pumped quantum devices.¹⁶²⁻¹⁶³

Chapter 8

Room temperature electroluminescence from mechanically formed van der Waals III-VI p - n junctions

In this chapter we report on the electrical and optical properties of homojunction and heterojunction devices formed from combinations of n -InSe, p -InSe, p -GaSe, and n -In₂O₃ semiconductors. Using mechanical exfoliation of Bridgman-grown crystals and a simple mechanical contact method or thermal annealing to fabricate the junctions, we demonstrate room temperature electroluminescence and investigate the nature and bias dependence of the electroluminescence emissions. The samples structure was described in section 4.1.4. The electroluminescence (EL) measurements and current-voltage (I - V) characteristics were performed by myself, and the Raman spectrum was measured by Mr. G. W. Mudd at the University of Nottingham. The photoconductivity measurements were performed by Mr. Z. Kudrynskyi at the Institute for Problems of Materials Science, the National Academy of Sciences of Ukraine, Chernivtsi. The XTEM and EXD studies were performed at the Nottingham Nanotechnology and Nanoscience Centre, University of Nottingham by Dr. M. W. Fay. These results were published in *Advanced Optical Materials* **2**, 1064 (2014).

8.1 Introduction

Over recent years there has been a resurgence of interest in exfoliable layered crystals¹⁶⁴ following their integration into graphene-based devices.^{78, 81, 165-167} These materials are often referred to as van der Waals (vdW) solids due to the weak interlayer coupling. Large band gap insulators such as hexagonal boron nitride have

been exploited as tunnel barriers,⁸¹ substrates for graphene,¹⁶⁷ and as quasi-epitaxial protective layers,^{8, 166} while metal chalcogenides such MoS₂ and WSe₂ are attracting increasing interest as optoelectronic materials.^{78, 168-171} It is now established that these compounds have a thickness-dependent electronic band structure, including a transition from indirect- to direct-band gap for single monolayers, a property that has stimulated recent studies of photoconductivity and photovoltaic effects.¹⁶⁸⁻¹⁷¹ By exploiting the ease with which atomically thin layers of these materials can be produced by mechanical exfoliation, it is now possible to assemble van der Waals heterostructures layer by layer, with properties that are quite distinct from those of the bulk starting materials. Among the vdW crystals, the III-VI layered semiconductors, such as GaSe and InSe, provide an important class of direct-band gap semiconductors.^{23-24, 32, 96, 99, 172} Recent work has included the exfoliation²³ and growth by a vapour phase technique⁹⁹ of thin films of GaSe, the demonstration of strong quantum confinement effects in InSe,^{24, 32} whose direct-band gap can be tuned in the near infrared spectral range when the crystals are exfoliated into nanometer-thick flakes,²⁴ and the direct-indirect band gap crossover occurring in the single monolayer limit.⁹⁶ These properties differ from those of other vdW crystals (*e.g.* MoS₂, WS₂...), which become direct only as single monolayers.¹⁷³⁻¹⁷⁴ In this chapter, I demonstrate room temperature electroluminescence from van der Waals semiconductor junctions with atomically flat interfaces, which are fabricated by exfoliation and direct mechanical adhesion or thermal annealing of III-VI layered crystals.

8.2 Structural and compositional studies

As illustrated in Figure 8.1a-b for a p -GaSe/ n -InSe heterojunction, cross-sectional images acquired using transmission electron microscopy (XTEM) and high-resolution TEM (HRTEM) show an abrupt interface between the layers; also, elemental mapping using energy-dispersive x-ray (EDX) spectroscopy reveals a well-defined, abrupt transition going from the InSe to the GaSe layer along the c -axis (Figure 8.1c); also, the Fourier analysis of the HRTEM images indicate that the layers are generally misaligned in the plane perpendicular to the c -axis (see Figure 8.2). These structural and compositional studies provide evidence for the weak interface interaction between the different layered crystals, which form an abrupt junction despite the large lattice mismatch, *i.e.* $\varepsilon = [a_{\text{InSe}} - a_{\text{GaSe}}] / a_{\text{InSe}} \approx 6\%$, between InSe and GaSe, and the simple mechanical contact method used to form the junction.

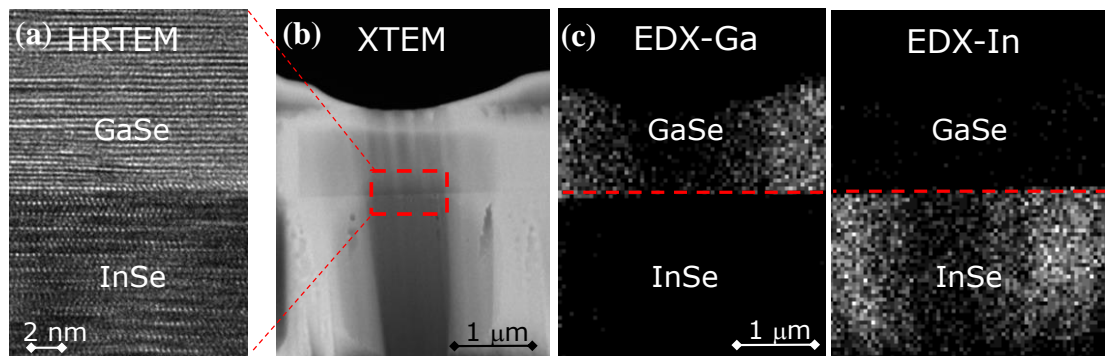


Figure 8.1: (a) HRTEM, (b) XTEM image and (c) EDX maps of a cross-sectional area of a p -GaSe/ n -InSe junction revealing an atomically, abrupt interface between the GaSe and InSe layers. The rectangle in part (b) corresponds to the thinnest cross-sectional part of the sample, from where the HRTEM image in part (a) is acquired. The red lines in the EDX maps in part (c) show the position of the GaSe/InSe interface as determined from the composition of Ga- and In-atoms along the junction.

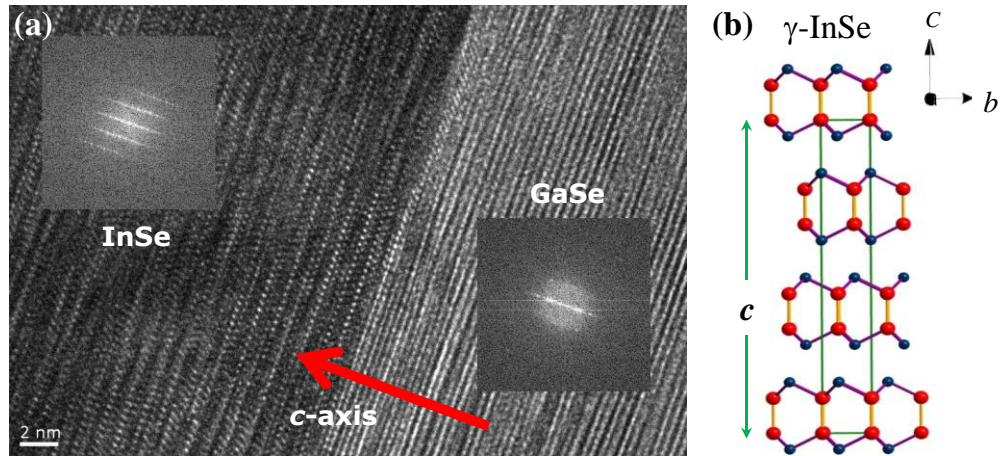


Figure 8.2: (a) HRTEM image of the InSe-GaSe interface region and corresponding FFT analysis of two areas of the image (insets). Similar FFT images were obtained from other areas close to the interface. The images indicate that the layers are aligned along the vertical c -axis (red arrow) and form an abrupt interface; also, the layers tend to be misaligned in the plane perpendicular to the c -axis. (b) Crystal structure of rhombohedral γ -InSe.

8.3 Room temperature I - V characteristics and photoresponse

The room temperature current-voltage characteristics, I - V , of the InSe homojunctions fabricated using the van der Waals mechanical contact technique show rectification with low leakage current densities in reverse bias, see Figure 8.3a.

The I - V curve departs from a simple ideal diode equation

$$I = I_s \left[\exp\left(\frac{eV}{K_B T}\right) - 1 \right], \quad (8.1)$$

where I_s is the dark saturation current, indicating a contribution of recombination on defect-related states at the junction. Similar diode characteristics were also measured in the heterojunctions, see Figure 8.4a and 8.5a. The p -InSe/ n -In₂O₃ heterojunction shows a considerably higher current in both forward and reverse bias with respect to the other two junctions. This could be due to the thermal annealing inducing defects

at the interface. The I - V curves tend to vary from sample to sample but all show clear rectification at room temperature.

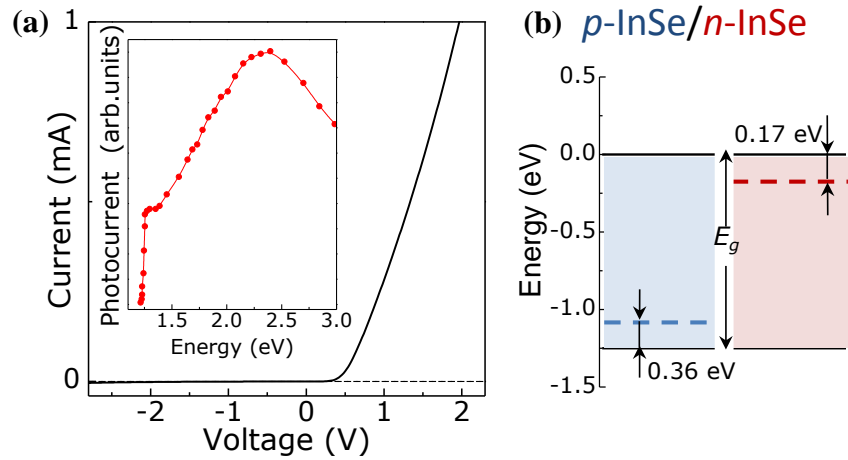


Figure 8.3: (a) Current-voltage characteristics at $T = 300\text{K}$ and (inset) photoconductivity spectrum at $V = 0\text{V}$. (b) Band diagrams for isolated p - and n -type InSe layers. Continuous lines indicate the band edges of the conduction and valence bands; dashed lines correspond to the Fermi levels estimated from the measured carrier density.

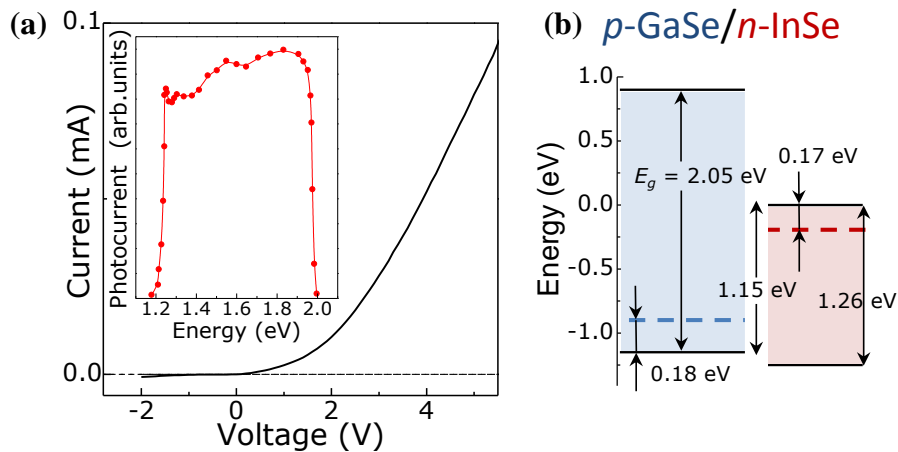


Figure 8.4: (a) Current-voltage characteristics at $T = 300\text{K}$ and (inset) photoconductivity spectrum at $V = 0\text{V}$. (b) Band diagrams for isolated p -type GaSe and n -type InSe layers. Continuous lines indicate the band edges of the conduction and valence bands; dashed lines correspond to the Fermi levels estimated from the measured carrier density.

The band diagrams for isolated *n*- and *p*-type materials are shown in Figure 8.3a to 8.5a. The Fermi level positions in the *n*- and *p*-type materials were determined using equation (8.2)

$$|E_{C(V)} - E_F| = k_B T \ln \left[\frac{N_{C(V)}}{N_{n(p)}} \right], \quad (8.2)$$

where $E_{C(V)}$ is the bottom of the conduction band (top of the valence band), E_F is the Fermi energy, $N_{n(p)}$ is the majority carrier concentration,¹⁰⁸ and $N_{C(V)}$ is the effective density of states in the corresponding bands given by

$$N_{C(V)} = 2 \left(\frac{m_{e(h)}^* k_B T}{2\pi\hbar^2} \right)^{3/2}, \quad (8.3)$$

where $m_{e(h)}^*$ is the electron (hole) effective mass. We have used the electron affinity, χ , of InSe, GaSe and In₂O₃ to be equal to 4.5 eV, 3.6 eV, and 3.7 eV, respectively.¹¹⁴

¹⁷⁵ For the *p*-GaSe/*n*-InSe heterojunction, we used *n*-InSe and *p*-GaSe crystals with room temperature concentrations of electrons and holes of 10¹⁵ cm⁻³ and 10¹³ cm⁻³, respectively.⁹² For the *n*-InSe/*p*-InSe homojunction, the undoped and intentionally Cd-doped InSe crystals have majority carrier concentrations of 10¹⁵ cm⁻³ (*n*-type) and 10¹³ cm⁻³ (*p*-type), respectively.¹¹³ For the *p*-InSe/*n*-In₂O₃ heterojunction, the Cd-doped InSe crystals have a hole concentrations of 10¹³ cm⁻³ and *n*-In₂O₃ has an electron concentration of $\sim 3 \times 10^{19}$ cm⁻³.¹¹³⁻¹¹⁴ We have used the electron effective mass, m_e^* , of InSe and In₂O₃ to be equal to 0.08 m_0 and 0.3 m_0 , respectively, and the hole effective mass, m_h^* , of InSe and GaSe to be equal to 0.17 m_0 and 0.2 m_0 , respectively.^{93, 176}

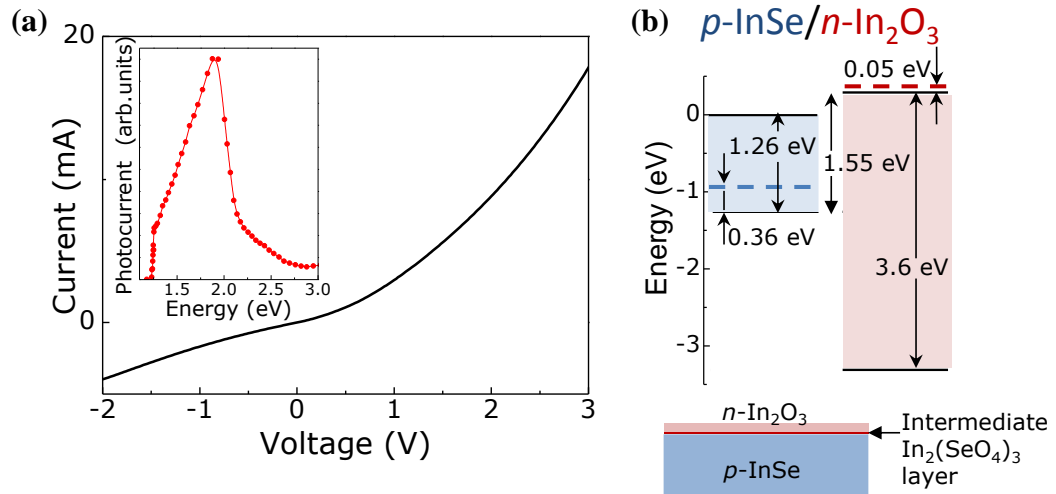


Figure 8.5: (a) Current-voltage characteristics at $T = 300\text{K}$ and (inset) photoconductivity spectrum at $V = 0\text{ V}$. (b) Band diagrams for isolated p -type InSe and n -type In₂O₃ layers (top) and the schematic diagram of the p - n junction (bottom). Continuous lines indicate the band edges of the conduction and valence bands; dashed lines correspond to the Fermi levels estimated from the measured carrier density and from Ref [114]. The estimated Fermi level of In₂O₃ is located at 0.05 eV above the conduction band edge.

Plots of the room temperature photocurrent versus the photon energy are shown in the insets of Figure 8.3a to 8.5a indicating a broad-band spectral sensitivity. For the photocurrent spectrum of the n -InSe/ p -InSe homojunction (see inset of Figure 8.3a), the absorption edge is at a photon energy ($h\nu \sim 1.25\text{ eV}$) corresponding to the calculated excitonic absorption in bulk InSe, which is $h\nu = E_g - E_b = 1.249\text{ eV}$, where $E_g = 1.264\text{ eV}$ and $E_b = 0.015\text{ eV}$ are the direct-band gap energy and exciton binding energy in bulk InSe at $T = 300\text{ K}$, respectively.^{24, 93, 98, 175} A high energy cut-off of the photoresponse is at $h\nu \sim 2.2\text{ eV}$: since the absorption coefficient of InSe increases with energy ($\alpha > 10^4\text{ cm}^{-1}$ for $h\nu > 2.2\text{ eV}$),⁹⁸ the high energy incident photons are mostly absorbed near the surface ($< 1\text{ }\mu\text{m}$) where the recombination time is short and photocarriers recombine before being collected at the p - n junction, which

is $> 1 \mu\text{m}$ below the *n*-InSe top-layer. The heterojunctions exhibit a similar behavior except that in this case the sharp cut-off is at $h\nu \sim 2 \text{ eV}$ (see inset of Figures 8.4a and 8.5a) due to the photon absorption in the top *p*-type GaSe layer, whose band gap energy is $E_g = 2.05 \text{ eV}$ at $T = 300 \text{ K}$ ⁹⁸ or in the *n*-In₂O₃ oxide layer, whose absorption band edge can be tuned by the oxidation time and temperature.⁸ In₂O₃ has a band gap energy of $E_g = 3.6 \text{ eV}$ at $T = 300 \text{ K}$.¹¹⁴ The long-time oxidation (96 h) of InSe substrates at temperature $T = 450 \text{ }^\circ\text{C}$ is accompanied by the formation of a new oxide phase, In₂(SeO₄)₃, with a band gap $E_g = 2.15 \text{ eV}$ at $T = 300 \text{ K}$.^{8, 115} The formation of this layer between InSe and In₂O₃ manifests through the appearance of the high energy cut-off of the photoresponse at $h\nu \sim 2 \text{ eV}$,¹⁷⁷ see Figure 8.5a. Since all our junctions are based on InSe flakes with thickness $t > 1 \mu\text{m}$, quantum confinement effects are not significant. Layers of InSe with thickness $t < 20 \text{ nm}$ would be required to observe a measurable increase of the direct band gap with decreasing t .²⁴

For white light excitation with incident power of 100 mW/cm^2 , the *n*-InSe/*p*-InSe diodes and *p*-InSe/*n*-In₂O₃ diodes produce an open-circuit voltage of $V_{oc} \sim 0.6 \text{ V}$ and a short-circuit current density of $J_{sc} \sim 0.7 \text{ mA/cm}^2$ and 30 mA/cm^2 , respectively. A larger photoresponse ($V_{oc} \sim 0.6 \text{ V}$ and $J_{sc} \sim 7.5 \text{ mA/cm}^2$) is also observed in the *p*-GaSe/*n*-InSe heterojunction. In particular, the larger band-gap top GaSe layer acts as a transparent window for the transmission of light. For an ideal junction, using the band diagrams of the isolated layers^{114, 175} and taking into account the energy position of the Fermi-levels (Figure 8.3b, 8.4b, and 8.5b), we estimate that $V_{oc} = 0.7 \text{ V}$ (*n*-InSe/*p*-InSe homojunction), $V_{oc} = 0.8 \text{ V}$ (*p*-GaSe/*n*-InSe heterojunction), and $V_{oc} = 1.24 \text{ V}$ (*p*-InSe/*n*-In₂O₃ heterojunction) close to the measured values of V_{oc} . The experimental V_{oc} -values can vary slightly in different junctions, thus indicating a possible contribution of crystal defects and impurities to

the band alignment. In summary, these diodes exhibit sensitivity to light in the near infrared and visible range of the electromagnetic spectrum at a level that is comparable or better than that reported in the current literature for photodetectors based on van der Waals crystals, such as MoS₂ and WS₂, which require exfoliation into single layers to become direct-band gap semiconductors, or gating to behave as *p*- or *n*-type semiconductors.¹⁶⁸⁻¹⁷¹

8.4 Room temperature electroluminescence

We now examine the EL properties of these junctions. In the homojunction, the EL peak is centred at $h\nu \sim 1.23$ eV, at lower energy with respect to the photoluminescence (PL) emission, Figure 8.6a. Also, the EL spectrum reveals a weak inflection point at the energy of the PL peak energy, thus suggesting that the red-shifted EL spectrum arises from the re-absorption of photons in the *n*-type InSe top-layer. To confirm this attribution, we have used the energy dependence of the absorption coefficient, $\alpha(h\nu)$, of InSe as derived from the measured PC spectrum and the value of $\alpha = 10^3$ cm⁻¹ at the energy of the free exciton absorption at $T = 300$ K.⁹⁸ Hence we have derived: *i*) the emission spectrum, $I_0(h\nu)$, using the relation

$$I_0(h\nu) = \alpha(h\nu) \exp\left(-\frac{h\nu}{k_B T}\right), \quad (8.4)$$

and *ii*) the effect on this spectrum of the re-absorption of photons through an InSe layer of thickness t , *i.e.*

$$I_t(h\nu) = I_0(h\nu) \exp[-\alpha(h\nu)t]. \quad (8.5)$$

As shown in Figure 8.6a, with increasing t the emission spectrum tends to red-shift relative to the absorption peak; in particular, its energy peak position reproduces the measured EL emission peak energy for $t \sim 15$ μm .

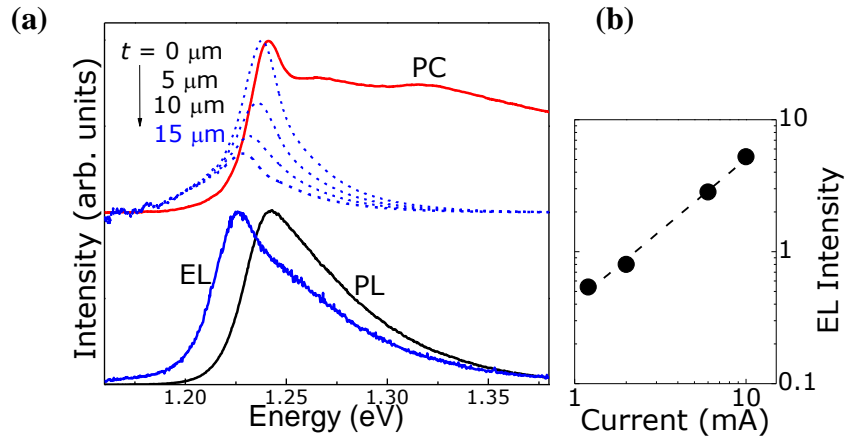


Figure 8.6: (a) Normalized EL (blue line, $\times 4$; $I = 10$ mA) and PL (black line; $P = 0.1$ mW) spectra of an n -InSe/ p -InSe homojunction at $T = 300$ K. The EL emission is compared with the emission spectra (dashed lines) derived from the measured PC spectrum (red line) by taking into account the absorption of photons through an InSe layer of thickness t . (b) Dependence of the EL integrated intensity on the current.

We note that the spectral position of the EL band does not change with increasing current, whereas its intensity scales linearly as expected for a free exciton recombination, rather than for carrier recombination from localized states (see Figure 8.6b). Thus in the InSe-based homojunctions, holes and electrons are injected from the p -type and n -type InSe, and exciton generation occurs through direct charge injection at the junction. Since the non-equilibrium carrier concentration is much larger than the equilibrium concentration, the dopant-concentration of the p - and n -layers should not have a significant influence on the EL intensity. In contrast, the p -GaSe/ n -InSe heterojunction diodes exhibit a distinct behavior: the EL emission is peaked at significantly lower energies ($h\nu = 1.1$ - 1.2 eV) relative to the PL emission of bulk InSe and its energy position blue-shifts with increasing current, Figure 8.7. To understand this behavior we need to consider the band alignment at the heterojunction interface: the conduction minimum (CB) of GaSe lies above that of InSe by $\Delta E_c = 0.9$ eV whereas the valence band (VB) edge of InSe lies below ($\Delta E_v =$

-0.1 eV) that of the larger band gap GaSe, resulting in a staggered line up for the holes¹⁷⁵ (inset of Figure 8.4b). Consequently the injection of holes and electrons from the p -GaSe and n -InSe can lead to the formation of spatially indirect excitons with a recombination energy ($h\nu \approx 1.15$ eV), which is below the energy of the direct exciton recombination in InSe, as we observe.

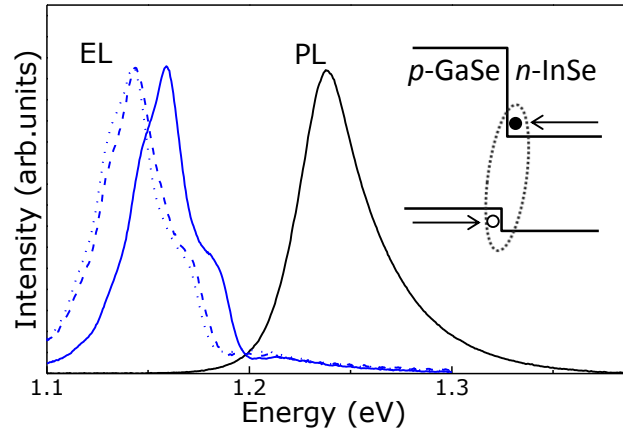


Figure 8.7: Normalized EL spectra (blue lines; $I = 0.8$ mA (dotted line; $\times 3$), 1.8 mA (dashed line; $\times 1.3$) and 3.2 mA (continuous line; $\times 1$) and PL spectrum (black line, $\times 0.002$; $P = 0.1$ mW) of a p -GaSe/ n -InSe heterojunction at $T = 300$ K. The inset sketches the spatially indirect exciton at the GaSe/InSe interface.

As the current increases we find: *i*) the intensity of the EL emission tends to saturate; *ii*) the EL band blue-shifts, and *iii*) weak EL features emerges at high energy. These observations suggest that carrier recombination involves localized states at the junction interface, which tend to fill with increasing bias. As shown in Figure 8.8, the main EL band can be de-convolved into equally energy spaced Gaussians with energy spacing of ~ 0.014 eV (116 cm^{-1}), which corresponds to the energy of non-polar optical phonons in InSe.²⁴⁻³² In γ -InSe, each unit cell has 12 atoms and 36 vibration modes. The Raman mode at 116 cm^{-1} is the dominant mode observed in the Raman spectra under non-resonant conditions (see Figure 8.10 for

Raman modes of InSe). Thus we associate the EL emission to a phonon-assisted electron-hole recombination at the junction interface.

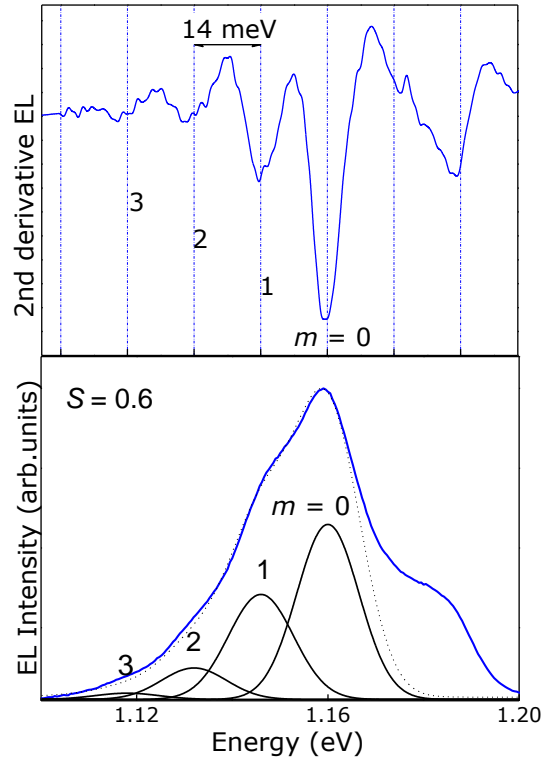


Figure 8.8: Room temperature EL spectrum and fit by equally spaced Gaussians using equation (8.6) in the text. The top figure shows equally spaced minima in the second derivative of the EL spectrum ($I = 3.2$ mA). The energy spacing (0.014 eV) corresponds to the energy of a non-polar phonon of InSe.

Coupling to lattice vibrations can be influenced by local electric fields arising from surface dipoles due to the local atomic structure and charge distribution at the surface of the layers; the degree of coupling to the phonons also increases with the strength of localization particularly for holes due to their larger mass. To estimate the strength of carrier-phonon coupling, we describe the intensity (I) of the main EL emission in Figure 8.7 by equation (8.6):

$$I(h\nu) = \sum_0^{\infty} \frac{S^m}{m!} e^{-S} \exp\left[-\frac{(E_0 - h\nu - mh\nu_p)^2}{2\sigma^2}\right], \quad (8.6)$$

which corresponds to the superposition of a zero-phonon line ($m = 0$) centered at E_0 and phonon sidebands ($m > 0$) peaked at $E_0 - mh\nu_p$. Here S is the Huang-Rhys factor and $h\nu_p = 0.014$ eV is the measured phonon energy.¹⁷⁷ In Figure 8.8, a typical EL spectrum is fitted to Eq. (8.6) with $S = 0.6$, $E_0 = 1.16$ eV and $m = 3$. The high energy part of the EL spectrum is not described by Eq. (8.6), thus suggesting an excitonic recombination involving the absorption of phonons. The specific form of the EL spectrum may change from sample to sample, but the main EL band is always centered at lower energy (~ 0.1 eV) relative to the band gap energy of InSe, thus indicating a well-defined band lineup at the GaSe/InSe interface.

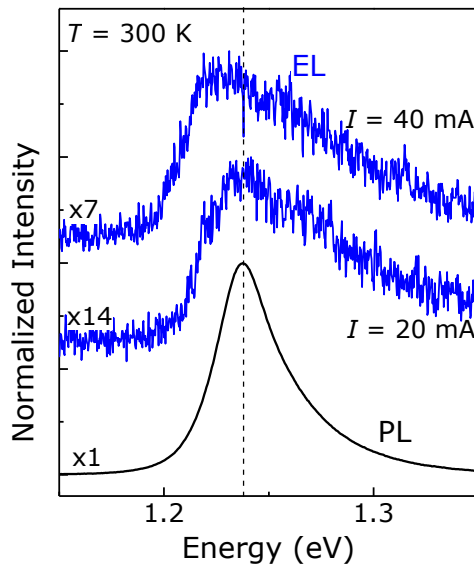


Figure 8.9: Normalized PL and EL ($I = 20$ mA and 40 mA) spectra of a p -InSe/ n -In₂O₃ junction at $T = 300$ K. For clarity, the spectra are offset along the vertical axis.

Figure 8.9 shows the room temperature PL and EL spectra of a p -InSe/ n -In₂O₃ heterojunction. The PL emission is peaked at $h\nu \sim 1.24$ eV which is close to the band gap energy of bulk InSe ($E_g = 1.26$ eV). The I - V characteristic of this heterojunction shows a considerable high current (see Figure 8.5a). However, a weak EL emission was observed for currents $I \geq 20$ mA, and its intensity increases with increasing

current. This weak EL emission may be due to the presence of non-radiative carrier recombination centers in the layers, which require further investigations. The EL emission is peaked at $h\nu \sim 1.24$ eV at $I = 20$ mA and redshifts with increasing current with respect to the PL emission ($h\nu \sim 1.24$ eV). The EL broadening may be due to the interface roughness,¹⁷⁸ while the redshift of the EL band with increasing current could be due to a heating effect.

8.5 Raman spectroscopy

Figure 8.10 shows the Raman spectrum of bulk γ -InSe at $T = 300$ K. The 633 nm line of a He-Ne laser ($P = 0.1$ mW) was focused on the sample along the c -axis in a backscattering geometry. The Raman peaks are centered at 116, 179.2, 201.2, 212.4, 228.0 cm^{-1} . The main Raman line at 116cm^{-1} corresponds to a non-polar phonon mode of energy $h\nu = 0.014$ eV (see inset and Ref [32]). This mode is responsible for the modulation of the EL signal shown in Figure 8.8.

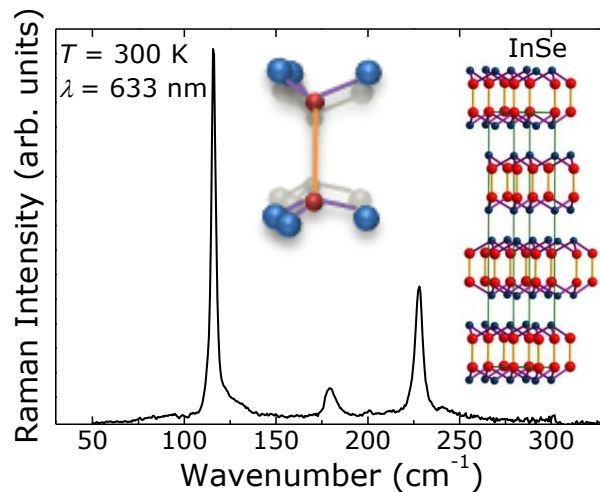


Figure 8.10: Raman spectrum of bulk γ -InSe at $T = 300$ K. Inset: crystal structure for γ -InSe and of a non-polar phonon mode of energy $h\nu = 0.014$ eV.

8.6 Temperature dependent electrical and optical studies

The I - V curves of a p -InSe/ n -InSe junction were measured over an extended temperature range down to $T = 14$ K: in both the forward-bias and reverse-bias conditions, the magnitude of the current decreases with decreasing temperature due to the influence of the temperature on the diffusion and recombination-generation currents, see Figure 8.11a. The temperature dependent EL emission is influenced by recombination and electrical injection of carriers at the junction. For a fixed forward (positive) bias, $V = 5$ V, applied to the junction, the current decreases due to reduced carrier diffusion with decreasing temperature. In turn, this leads to a decrease of the density of injected carriers and of the EL intensity, see Figure 8.11b.

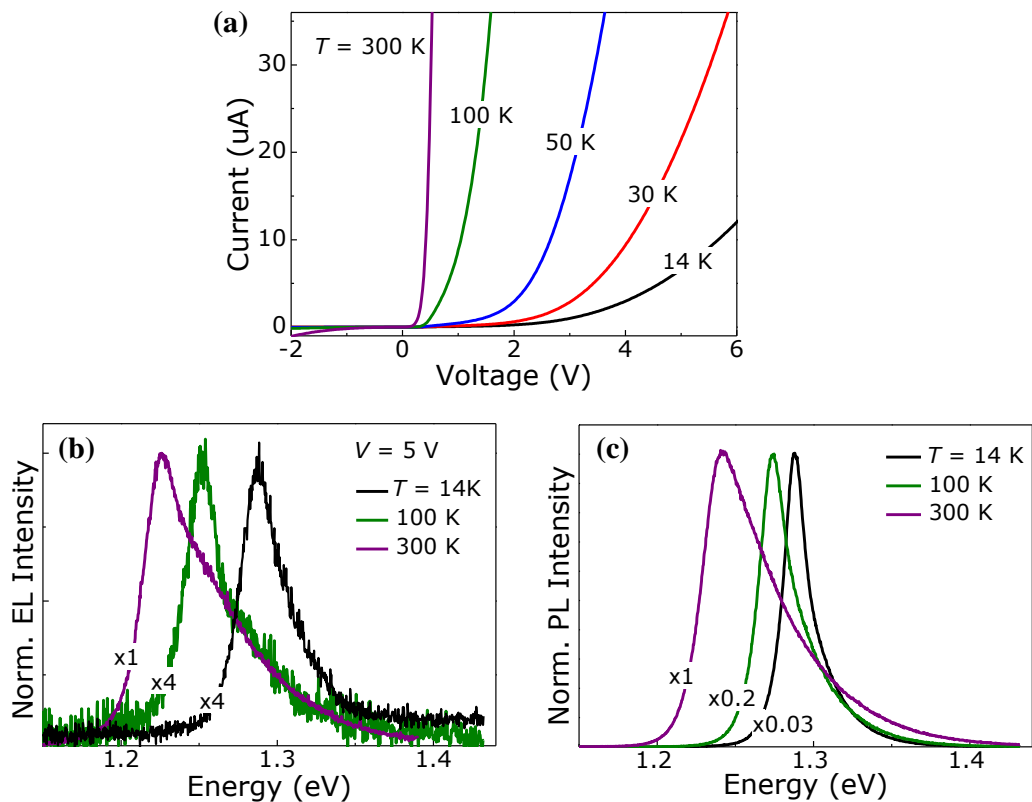


Figure 8.11: I - V characteristics (a), and normalized electroluminescence, EL (b) and photoluminescence, PL (c) spectra for a p -InSe/ n -InSe junction at various T in the range 14 K to 300 K. The EL spectra were acquired at $V = 5$ V.

For the PL study, the *p*-InSe/*n*-InSe junction was excited with a He-Neon laser ($\lambda = 633$ nm; $P = 0.1$ mW). With decreasing temperature from $T = 300$ K to 14 K, the PL emission shifts to lower energies and the PL intensity increases by a factor of ~ 30 , see Figure 8.11c. Similar behaviors were reported in the literature for bulk InSe.¹⁷⁹

8.7 Summary

We demonstrated room temperature electroluminescence from van der Waals semiconductor junctions with atomically flat interfaces, which are fabricated by exfoliation and direct mechanical adhesion or thermal annealing of III-VI layered crystals. Homojunction diodes formed from layers of *p*- and *n*-type InSe and heterojunction diodes formed by *p*-InSe and *n*-In₂O₃ exhibit EL emission peaked at energies ($h\nu \sim 1.23$ eV) close to the band gap energy of InSe ($E_g = 1.26$ eV) at room temperature. In contrast, heterojunction diodes formed by combining layers of *p*-type GaSe and *n*-type InSe emit at lower energies ($h\nu = 1.1$ - 1.2 eV), which we attribute to the generation of spatially indirect excitons and a staggered valence band line-up for the holes at the GaSe/InSe interface. Our results demonstrate the technological potential of mechanically formed heterojunctions and homojunctions of direct-band gap layered III-VI compounds. These can enable tunable and strong optical response over an extended wavelength range, from the near-infrared (NIR) to the visible (VIS) spectrum; it should also be possible to achieve different band alignments and potential profiles by combining different layered semiconductors, and by selecting the doping, *n*- or *p*-type, of the component layers, which cannot be yet achieved in many other van der Waals crystals.

Chapter 9

Conclusion and future directions

The aims of this thesis were to study the effect of *post-growth* hydrogenation on the electronic activity of nitrogen in III-V semiconductor compounds and to investigate the electrical and optical properties of *p-n* junctions formed from *n*- and *p*-type III-VI van der Waals crystals. The novel findings of this research can be summarized as follows: (i) we have shown that the dissociation of N-H complexes by a focused laser beam is a pure photon-assisted effect at low laser powers ($P_a < 40$ mW); (ii) hydrogen can be successfully incorporated into different *p-i-n* LED structures by low energy (100 eV) ion beam irradiation using a Kaufman source, thus modifying electrical and optical properties; and (iii) mechanically formed van der Waals III-VI *p-n* junctions emit electroluminescence at room temperature. In the following, the main findings are summarized and future directions are outlined.

9.1 Band-gap profiling by laser writing of H-containing III-N-Vs

The incorporation of a small concentration (~1%) of N-atoms in III-Vs leads to a large reduction of the band gap energy.⁴¹ On the other hand, the incorporation of hydrogen in III-N-Vs acts to neutralize the electronic activity of N through the formation of dihydrogen N-H complexes with C_{1h} symmetry or C_{2v} asymmetry, thus reversing the effect of the N-atoms on the band structure of the host crystal.^{2-3, 73, 180} In this study, we used a focussed laser beam or thermal annealing to control the electronic activity of N- and H-atoms in III-N-V quantum wells (QWs).

Our laser writing technique and micro-photoluminescence (μ PL) studies provided real-time *in-situ* characterisation and control of the N-H complex

dissociation and of the band gap energy of III-N-Vs. We have shown that the dissociation of N-H complexes in hydrogenated III-N-Vs can be achieved by low laser powers, corresponding to local temperatures much smaller than those required for thermal dissociation (> 200 °C). The photon absorption by the N-H complex mediated by photogenerated carriers provides a mechanism for band-gap profiling: profiles of different shapes can be patterned with submicron spatial resolution and high energy accuracy in the growth plane of the III-N-Vs; the profiles are erasable and the sample can be re-hydrogenated making any nanoscale *in-plane* band gap profile rewritable. The possibility of *in-plane* profiling of the band gap energy offers flexibility in the control and exploitation of the electronic properties of a semiconductor without the implementation of lithographic/etching techniques. The versatility of hydrogen makes this direct laser writing approach of general interest and relevant to the development of fast and easy fabrication approaches to nanotechnologies. Non-thermal (photonic) laser writing may offer an alternative promising route to non-destructive band gap profiling of temperature sensitive material systems. Also, it advances prospects of using hydrogen in III-N-Vs in future nanotechnologies. The results of this study were published in *Physical Review B* **86**, 155307 (2012).

9.2 Tunable spectral response by hydrogen irradiation of Ga(AsN) superlattice diodes

In this work, I demonstrated that the spectral response of a Ga(AsN)/AlAs superlattice (SL) *p-i-n* diode can be tuned by *post-growth* hydrogen irradiation and controlled thermal annealing. Our method exploits the combined effects of hydrogen and nitrogen on the electronic properties of a III-V compound: Hydrogen is diffused

into a III-N-V SL grown well below the surface (> 550 nm) where it neutralizes the electronic activity of nitrogen by forming dihydrogen N-H complexes; the controlled thermal dissociation of the complexes is then exploited to tune the photocurrent absorption and electroluminescence emission of the superlattice; additional versatility is enabled by the photo-stimulated diffusion of H in the Be doped p -type contact layer with a focused laser beam; a focused laser beam is used to create preferential injection paths for the carriers thus creating a nanoscale light emitting diode. Because of the thick capping layer of our device (550 nm), which is larger than the penetration depth (~ 200 nm) of our laser beam with $\lambda = 532$ nm,¹²⁸ we were not able to modify significantly the band gap of Ga(AsN) SLs by dissociating the N-H complexes in the i -region. In order to achieve this, we should to use long wavelength lasers ($\lambda > 900$ nm) for laser writing or re-grow our device with a thin capping layer (< 200 nm). Our approach could be implemented in other materials and heterostructure devices, and offers the advantage of enabling an accurate control of the spectral response of a diode using a single wafer. Also, it could enable the fabrication of planar diode arrays¹⁴⁶ with distinct light absorbing regions, all integrated onto a monolithic semiconductor structure, thus providing an alternative to re-growth techniques. These results were published in *Applied Physics Letters* **104**, 242110 (2014).

9.3 A movable resonant tunneling light emitting diode

In this study, I have reported on the fabrication of a movable micrometer-size light emitting area in a GaAs/AlAs-based resonant tunneling light emitting diode (RT-LED). We have shown that the position of the light emitting area can be spatially shifted over tens of μm by varying the applied voltage by a few hundreds of

mV. The hydrogen passivation of C-dopants on the p -type contact layer of the diode results into an increase of the resistivity of the p -type contact layer in the hydrogenated area (open area), and causes a lateral voltage drop from the metal contact edge towards the center of the mesa. Thus the resonant injection of electrons and holes into the QW subbands occurs at different positions for each applied bias. This *simultaneous resonant injection* of electrons and holes into the QW subbands increases the EL intensity and the peak-to-valley EL ratio. This technique could be implemented in other fields of research that use RTDs for a variety of applications spanning from THz resonators¹⁸¹ to high efficiency single-photon detectors¹⁸² and room-temperature negative-differential-resistance devices.¹⁵⁹⁻¹⁶⁰ These findings were published in *Applied Physics Letters* **103**, 241105 (2013).

9.4 Room temperature electroluminescence from mechanically formed van der Waals III-VI p - n junctions

Following the discovery of high-quality graphene monolayers extracted from graphite crystals by simple exfoliation technique, the research on van der Waals layered crystals has received great interest. The exfoliation technique works well for most van der Waals crystals since the absence of covalent bonds between adjacent layers promotes chemical stability and eliminates problems posed by dangling bonds at the material surface, providing *defect-free* crystals down to the atomic thickness. Among the van der Waals crystals, the III-VI layered semiconductors, such as GaSe and InSe, provide an important class of direct-band gap semiconductors,^{23-24, 32, 96, 99, 172} whose band gap can be tuned in the near infrared spectral range when the crystals are exfoliated into nanometer-thick flakes,²⁴ and the direct-indirect band gap crossover occurs in the single monolayer limit.⁹⁶ In my final year of PhD, I have

contributed to the development of a new class of semiconductor structures based on van der Waals III-VI homojunctions and heterojunctions.

In this work, I demonstrated room temperature electroluminescence from van der Waals semiconductor junctions with atomically flat interfaces, which are fabricated by exfoliation and direct mechanical adhesion or thermal annealing of III-VI layered crystals. Mechanically-formed van der Waals III-VI junctions have atomically flat interfaces, well-defined band lineups and radiative recombination from electrically injected carriers are achieved even in the presence of a large lattice mismatch ($\sim 6\%$ for GaSe on InSe) between the constituent layers. Electroluminescence emission was detected at room temperature in all of the measured p - n junctions (n -InSe/ p -InSe homojunction, p -GaSe/ n -InSe heterojunction, and p -InSe/ n -In₂O₃ heterojunction) thus opening realistic prospects for the implementation of these layered crystals in different sequences of layer stacking. These electroluminescence and photon sensitive junctions could be transferred on different substrates (*e.g.* plastics, graphene, boron nitride, *etc.*); since these crystals are direct-band semiconductors over a range of thicknesses,²⁴ down to a few nanometers, they are promising candidates for electronic and optical components in nanoscale optoelectronics and light emitting diodes. These results were published in *Advanced Optical Materials* **2**, 1064 (2014).

9.5 Future directions

It would be interesting to study the effect of hydrogen incorporation during the growth of a device structure based on III-Vs or dilute III-N-Vs. For example, the incorporation of hydrogen during the growth of a GaAs spacer layer lies between the p -type GaAs and the i -region of a resonant tunneling p - i - n diode could enable to

diffuse interstitial hydrogen donors, H^+ , from the GaAs spacer layer towards the *i*-region using a focused laser beam. The diffused H^+ could produce a set of well resolved and discrete electronic energy levels through which electrons can tunnel. Similar studies on diffusion of mobile double charged manganese interstitial atoms (Mn_i^{2+}) from a *p*-doped (GaMn)As layer to an AlAs/GaAs/AlAs QW *p-i-n* diode by conventional thermal annealing and laser writing are discussed in Refs [183] and [141, 151], respectively.

Also, my future work will focus on the fabrication and characterization of new device structures based on exfoliated-thin flakes of III-VI van der Waals crystals. We have reported the room temperature electroluminescence from mechanically formed *p-n* junctions based on exfoliated III-VI vdW bulk crystals. Fabricating similar junction devices with ultrathin flakes is challenging, but could provide new physics. Device structures based on the combination of transparent graphene and exfoliated thin flakes of III-VI vdW crystals could also be potential candidates for 2D optoelectronics and give access to new functionalities.

Appendix A

Electron effective mass in dilute nitride III-V alloys

The incorporation of N in a III-V compound tends to modify the curvature of the energy–wave vector $E(k)$ dispersion of the CB, thus changing the electron effective mass m^* , which is defined as

$$m^*(k) = \frac{\hbar^2}{\frac{d^2 E(k)}{dk^2}}. \quad (\text{A. 1})$$

According to the BAC model, the k -dependence of the $E_-(k)$ sub-conduction band is

$$E_-(k) = \frac{1}{2} \left\{ (E_N + E_M(k)) - \sqrt{[(E_N - E_M(k))^2 + 4C_{NM}^2 x]} \right\}, \quad (\text{A. 2})$$

where $E_M(k)$ and E_N are, respectively, the energies of the conduction band minima of the host matrix and of the N level measured with respect to the top of the valence band, C_{NM} is a constant dependent on the host matrix, and x is the mole fraction of substitutional N.

The first derivative with respect to k of $E(k)$ is

$$\frac{dE_-(k)}{dk} = \frac{1}{2} \frac{dE_M(k)}{dk} \left[1 - \frac{(E_N - E_M(k))}{\sqrt{(E_N - E_M(k))^2 + 4C_{NM}^2 x}} \right]. \quad (\text{A. 3})$$

The second derivative with respect to k of $E(k)$ is

$$\begin{aligned} \frac{d^2 E_-(k)}{dk^2} = & \frac{1}{2} \frac{d^2 E_M(k)}{dk^2} \left[1 - \frac{(E_N - E_M(k))}{\sqrt{(E_N - E_M(k))^2 + 4C_{NM}^2 x}} \right] + \\ & \frac{1}{2} \frac{dE_M(k)}{dk} \frac{d}{dk} \left(1 - \frac{(E_N - E_M(k))}{\sqrt{(E_N - E_M(k))^2 + 4C_{NM}^2 x}} \right). \end{aligned} \quad (\text{A. 4})$$

At $k = 0$, $\frac{dE_-(k)}{dk} = 0$ and $\frac{dE_M(k)}{dk} = 0$. Thus we can write

$$\left. \frac{d^2 E_-(k)}{dk^2} \right|_{k=0} = \left. \frac{d^2 E_M(k)}{dk^2} \right|_{k=0} \left[1 - \frac{(E_N - E_M(k))}{\sqrt{(E_N - E_M(k))^2 + 4C_{NM}^2 x}} \right]_{k=0}. \quad (\text{A.5})$$

Equation A.5 can also be written as

$$\frac{\hbar^2}{m^*} = \frac{1}{2} \frac{\hbar^2}{m_0^*} \left[1 - \frac{(E_N - E_M(k))}{\sqrt{(E_N - E_M(k))^2 + 4C_{NM}^2 x}} \right], \quad (\text{A.6})$$

where m_0^* is the electron effective mass of the host crystal at $k = 0$. Hence, the effective mass at $k = 0$ of the III-N-V alloy can be written as

$$m^* = \frac{2m_0^*}{\left[1 - \frac{(E_N - E_M(k))}{\sqrt{(E_N - E_M(k))^2 + 4C_{NM}^2 x}} \right]}. \quad (\text{A.7})$$

Appendix B

Electronic bound states of a GaAs_{1-x}N_x/GaAs quantum well

Here we describe the electronic bound states of a Ga(AsN)/GaAs QW using the BAC model and a QW square potential model. The height of the QW is $U_b = E_g(\text{GaAs}) - E_g(\text{GaAs}_{1-x}\text{N}_x)$ where E_g is the band gap energy. The potential profile along the z -direction is given by

$$U(z) = \begin{cases} U_b & |z| > \frac{a}{2} \\ 0 & |z| < \frac{a}{2} \end{cases}, \quad (\text{B.1})$$

where a is the width of the QW.

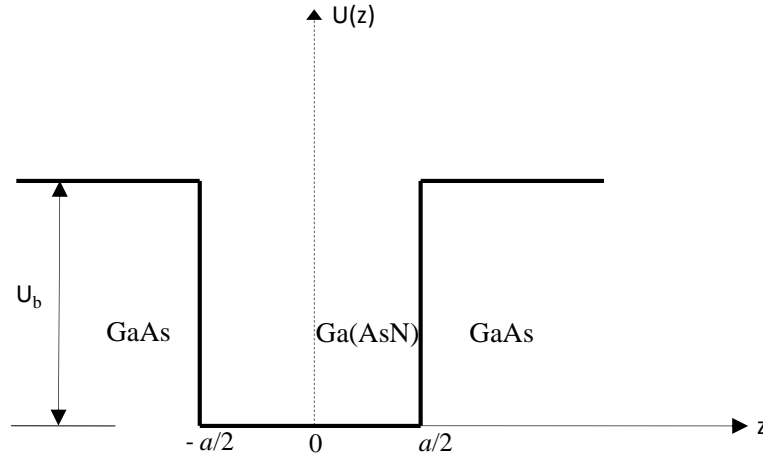


Figure B.1: Schematic diagram of a finite square Ga(AsN)/GaAs QW.

The time-independent Schrödinger equation can be written as

$$-\frac{\hbar^2}{2m^*} \frac{d^2}{dz^2} \psi(z) + U_b \psi(z) = \varepsilon \psi(z), \quad (\text{B.2})$$

where m^* is the electron effective mass and ε is the eigenvalue.

The wave functions inside the well have even/odd symmetry and can be written as

$$\psi(z) = C \begin{cases} \cos kz \\ \sin kz \end{cases}, \quad (\text{B.3})$$

$$\text{with eigenvalue } \varepsilon = \frac{\hbar^2 k^2}{2m_w^*}, \quad (\text{B. 4})$$

where m_w^* is the electron effective mass inside the well.

Outside the well, the eigenfunction can be written as

$$\psi(z) = D \exp(\pm Kz) \quad (\text{B. 5})$$

with

$$\frac{\hbar^2 K^2}{2m_b^*} = U_b - \varepsilon, \quad (\text{B. 6})$$

where $\varepsilon < U_b$ and m_b^* is the electron effective mass outside the well.

Using boundary conditions at $z = \frac{a}{2}$ and the continuity of $\psi(z)$, we obtain

$$\psi\left(\frac{a}{2}\right) = C \begin{pmatrix} \cos \frac{ka}{2} \\ \sin \frac{ka}{2} \end{pmatrix} = D \exp\left(-\frac{1}{2}Ka\right). \quad (\text{B. 7})$$

Similarly, the continuity of the first derivative of ψ at $z = \frac{a}{2}$ gives

$$\left. \frac{d\psi}{dz} \right|_{z=\frac{a}{2}} = \frac{Ck}{m_w^*} \begin{pmatrix} -\sin \frac{ka}{2} \\ \cos \frac{ka}{2} \end{pmatrix} = -\frac{DK}{m_b^*} \exp\left(-\frac{1}{2}Ka\right). \quad (\text{B. 8})$$

Dividing Eq. B.6 and Eq. B.7 to eliminate the normalization factors C and D , we derive

$$\frac{k}{m_w^*} \begin{pmatrix} \tan \frac{ka}{2} \\ -\cot \frac{ka}{2} \end{pmatrix} = \frac{K}{m_b^*} \quad (\text{B. 9})$$

and

$$\begin{pmatrix} \tan \frac{ka}{2} \\ -\cot \frac{ka}{2} \end{pmatrix} = \frac{m_w^* K}{m_b^* k} = \frac{m_w^*}{m_b^* k} \sqrt{\frac{2m_b^*(U_b - \varepsilon)}{\hbar^2}} = \sqrt{\frac{m_w^*}{m_b^*} \left(\frac{2m_w^* U_b}{\hbar^2 k^2} - 1 \right)}. \quad (\text{B. 10})$$

We define $\theta = \frac{ka}{2}$ and $\theta_0^2 = \frac{m_w^* U_b a^2}{2\hbar^2}$.

Thus we can write

$$\begin{pmatrix} \tan \theta \\ -\cot \theta \end{pmatrix} = \sqrt{\frac{m_w^*}{m_b^*} \left(\frac{\theta_0^2}{\theta^2} - 1 \right)}. \quad (\text{B.11})$$

Both sides of Eq. B.11 are plotted against θ and the intersections give the solutions.

The ground state energy ε_{e1}

$$\varepsilon_{e1} = \frac{\hbar^2 k^2}{2m_w^*} = \frac{2\hbar^2 \theta_1^2}{m_w^* a^2}, \quad (\text{B.12})$$

corresponds to the first intersection point at $\theta = \theta_1$.

The energy of the optical transition between the first QW electron subband and the top of the valance band is

$$E_{QW} = E_g + \varepsilon_{e1}, \quad (\text{B.13})$$

where E_g is the band gap energy of GaAs_{1-x}N_x. The valence band is not affected by the N localized states. Since we assumed that the valence band is flat at Γ point.

Therefore the energy of the lowest QW transition is

$$E_{QW} = \frac{1}{2} \left\{ E_N + E_M - \sqrt{[E_N - E_M]^2 + 4C_{NM}^2 x} \right\} + \varepsilon_{e1} \quad (\text{B.14})$$

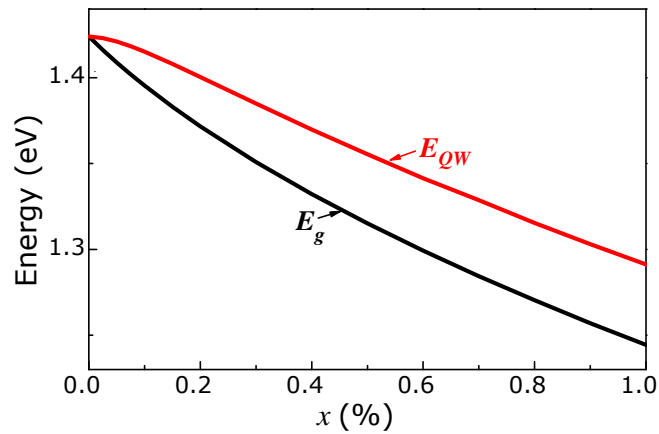


Figure B.2: Dependence on x of the band gap energy of GaAs_{1-x}N_x, E_g , and of the inter band transition energy of a GaAs_{1-x}N_x/GaAs QW, E_{QW} , with $a = 6$ nm, $E_N = 1.65$ eV and $C_{NM} = 2.7$ eV at $T = 300$ K.

Figure B.2 shows the calculated x -dependence of E_g using the BAC model, and the inter band transition energy, E_{QW} , of a GaAs_{1-x}N_x/GaAs QW using Eq. B.14. For the BAC model, we assume an N-level located at 0.23 eV above the conduction band minimum of GaAs at $T = 300\text{K}$ and an interaction parameter $C_{NM} = 2.7 \text{ eV}$.¹²⁶ Also, we have considered the x -dependence of the electron effective mass. We have instead neglected the exciton binding energy, which represents a small correction to the calculated energies.

Appendix C

Laser induced lattice heating in GaAs

Here we describe the laser induced lattice temperature rise in GaAs in terms of the temperature dependent thermal conductivity $K(T)$, and the temperature and wavelength dependent absorption coefficient $\alpha(T, \lambda)$. The laser beam has a Gaussian intensity distribution given by

$$I = I_0 \exp\left(-\frac{r^2}{w^2}\right) = I_0 \exp(-R^2). \quad (\text{C. 1})$$

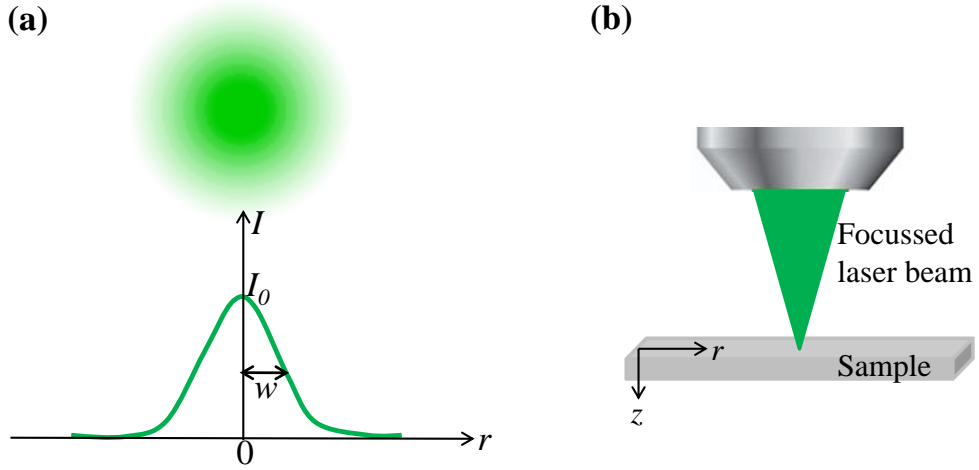


Figure C.1: (a) schematic of a laser spot and its intensity distribution along r . w is the beam waist. (b) Focused laser beam on a sample surface.

Following M. Lax,¹²⁷ the laser induced temperature can be written as

$$T(R, Z, W) = T_{max} N(R, Z, W), \quad (\text{C. 2})$$

where $N(R, Z, W)$ is a reduction factor, $R = r/w$, $Z = z/w$, $W = \alpha(T, \lambda)w$, and $\alpha(T, \lambda)$ is the absorption coefficient. T_{max} is the maximum temperature rise at the beam centre ($R = 0$) and at the surface ($Z = 0$). This occurs when the beam absorption is so large ($W \rightarrow \infty$) that the heat is all generated on the surface.

T_{max} depends on the beam power P , thermal conductivity $K(T)$, and the beam radius w , and can be written as

$$T_{max} = \frac{P}{2\pi^{1/2}K(T)w}. \quad (C.3)$$

For excitation over a finite depth, the temperature rise will be smaller and

$$N(0,0,W) = \left(\int_0^\infty F(\lambda) \frac{W}{W+\lambda} d\lambda \right) \left[\int_0^\infty F(\lambda) d\lambda \right]^{-1}, \quad (C.4)$$

where $F(\lambda)$ is the Bessel transform of $I(R)$.

For the Gaussian case,

$$F(\lambda) = \frac{1}{2} \exp\left(-\frac{1}{4}\lambda^2\right). \quad (C.5)$$

The solution of Eq. C.4 is given by

$$N(0,0,W) = WD \left(\frac{1}{2}W\right) - \frac{W}{2\pi^2} \exp\left(-\frac{1}{4}W^2\right) Ei\left(\frac{1}{4}W^2\right), \quad (C.6)$$

where $D(x) = \exp(-x^2) \int_0^x \exp(t^2) dt$ is Dawson's integral,

$Ei(x) = P \int_{-\infty}^x \frac{\exp(t)}{t} dt$ is the exponential integral and t is laser exposure time.

Therefore, the maximum temperature rise at the beam centre on the surface $T(0,0,W)$, can be written in terms of T_{max} (Eq. C.2) and of a reduction factor $N(0,0,W)$ caused by the finite depth of penetration, i.e.,

$$T(0,0,W) = \frac{P}{2\pi^{1/2}K(T)w} \left[WD \left(\frac{1}{2}W\right) - \frac{W}{2\pi^2} \exp\left(-\frac{1}{4}W^2\right) Ei\left(\frac{1}{4}W^2\right) \right]. \quad (C.7)$$

Let's consider the spatial distribution of the temperature rise in the form of Eq. C.2

$$T(R,Z,W) = T_{max} N(R,Z,W),$$

where $N(R,Z,W)$ describes the reduction in the temperature rise caused by the finite penetration (finite $W = \alpha w$) and deviations R and Z from the centre of the beam at the surface.

For the case of $R \gg 1/W$ (i.e., $r \gg \alpha^{-1}$ the penetration depth of the laser beam),

$N(R, Z, W)$ is given by

$$N(R, Z, W) = \frac{1}{\pi^{1/2}} \frac{1}{(R^2 + Z^2)^{1/2}}. \quad (\text{C. 8})$$

Therefore,

$$T(R, Z, W) = \frac{P}{2\pi K(T)w} \frac{1}{(R^2 + Z^2)^{1/2}}. \quad (\text{C. 9})$$

At first we calculate T_{max} by using the temperature dependent thermal conductivity $K(T)$ from Ref [128], beam waist $w = 0.5 \mu\text{m}$ (our laser spot diameter $\approx 1 \mu\text{m}$), and the laser power $P = P_{max} \times (1-R_f)$, where P_{max} is the laser output power and $R_f = 0.3$ is the surface reflection coefficient. Then we calculate the actual maximum temperature rise at the beam centre and at the surface $T(0,0, W)$ from Eq. C.6 by using the wavelength dependent absorption coefficient of GaAs at $T = 300 \text{ K}$.¹²⁸ For $\lambda = 515 \text{ nm}$, $\alpha = 9.25 \times 10^6 \text{ m}^{-1}$. For $\lambda = 633 \text{ nm}$, $\alpha = 3.95 \times 10^6 \text{ m}^{-1}$. Also we consider a laser exposure time $t = 15 \text{ s}$ and 20 s for $\lambda = 515 \text{ nm}$ and 633 nm , respectively. Finally, we calculate the temperature distribution along R at the sample surface (we chose $Z = 0$) using Eq. C.9.

Bibliography

- ¹N. López, L. A. Reichertz, K. M. Yu, K. Campman, and W. Walukiewicz, *Phys. Rev. Lett.* **106**, 028701 (2011).
- ²G. Ciatto, F. Boscherini, A. Amore Bonapasta, F. Filippone, A. Polimeni, and M. Capizzi, *Phys. Rev. B* **71**, 201301(R) (2005).
- ³L. Wen, F. Bekisli, M. Stavola, W. B. Fowler, R. Trotta, A. Polimeni, M. Capizzi, S. Rubini, and F. Martelli, *Phys. Rev. B* **81**, 233201 (2010).
- ⁴M. Felici, A. Polimeni, G. Salviati, L. Lazzarini, N. Armani, F. Masia, M. Capizzi, F. Martelli, M. Lazzarino, G. Bais, M. Piccin, S. Rubini, and A. Franciosi, *Adv. Mater.* **18**, 1993 (2006).
- ⁵M. Bissiri, G. Baldassarri Höger von Högersthal, A. Polimeni, M. Capizzi, D. Gollub, M. Fischer, M. Reinhardt, and A. Forchel, *Phys. Rev. B* **66**, 033311 (2002).
- ⁶M. Berti, G. Bisognin, D. De Salvador, E. Napolitani, S. Vangelista, A. Polimeni, M. Capizzi, F. Boscherini, G. Ciatto, S. Rubini, F. Martelli, and A. Franciosi, *Phys. Rev. B* **76**, 205323 (2007).
- ⁷G. Bisognin, D. De Salvador, E. Napolitani, M. Berti, A. Polimeni, M. Capizzi, S. Rubini, F. Martelli, and A. Franciosi. *J. Appl. Cryst.* **41**, 366-372 (2008).
- ⁸Z. D. Kovalyuk, V. M. Katerynychuk, A. I. Savchuk, and O. M. Sydor, *Mater. Sci. Eng.* **109**, 252 (2004).
- ⁹C. G. Van de Walle and J. Neugebauer, *Nature* **423**, 626 (2003).
- ¹⁰J. Chevallier and M. Aucouturier, *Ann. Rev. Mater. Sci.* **18**, 219 (1988).
- ¹¹R. Fischer, G. Peter, E. O. Göbel, M. Capizzi, A. Frova, A. Fischer, and K. Ploog, *Appl. Phys. Lett.* **60**, 2788 (1992).
- ¹²M. Sparvoli, R. D. Mansano, and J. F. D. Chubaci, *Phys. Status Solidi A* **210**, 1606 (2013).

- ¹³S. T. B. Goennenwein, T. A. Wassner, H. Huebl, M. S. Brandt, J. B. Philipp, M. Opel, R. Gross, A. Koeder, W. Schoch, and A. Waag, *Phys. Rev. Lett* **92**, 227202 (2004).
- ¹⁴D. C. Elias, R. R. Nair, T. M. G. Mohiuddin, S. V. Morozov, P. Blake, M. P. Halsall, A. C. Ferrari, D. W. Boukhvalov, M. I. Katsnelson, A. K. Geim, and K. S. Novoselov, *Science* **323**, 610 (2009).
- ¹⁵R. Trotta, A. Polimeni, F. Martelli, G. Pettinari, M. Capizzi, L. Felisari, S. Rubini, M. Francardi, A. Gerardino, P. C. M. Christianen, and J. C. Maan, *Adv. Mater.* **23**, 2706 (2011).
- ¹⁶S. Birindelli, M. Felici, J. S. Wildmann, A. Polimeni, M. Capizzi, A. Gerardino, S. Rubini, F. Martelli, A. Rastelli, and R. Trotta, *Nano Lett.* **14**, 1275 (2014).
- ¹⁷A. S. Mayorov, R. V. Gorbachev, S. V. Morozov, L. Britnell, R. Jalil, L. A. Ponomarenko, P. Blake, K. S. Novoselov, K. Watanabe, T. Taniguchi, and A. K. Geim, *Nano Lett.* **11**, 2396 (2011).
- ¹⁸A. A. Balandin, S. Ghosh, W. Bao, I. Calizo, D. Teweldebrhan, F. Miao, and C. Ning Lau, *Nano Lett.* **8**, 902 (2008).
- ¹⁹K. S. Novoselov, A. K. Geim, S. V. Morozov, D. Jiang, Y. Zhang, S. V. Dubonos, I. V. Grigorieva, and A. A. Firsov, *Science* **306**, 666 (2004); Y. Wang, V. W. Brar, , A. V. Shytov, Q. Wu, W. Regan, H. -Z. Tsai, A. Zettl, L. S. Levitov, and M. F. Crommie, *Nat. Phys.* **8**, 653 (2012).
- ²⁰A. Ayari, E. Cobas, O. Ogundadegbe, and M. S. Fuhrer, *J. Appl. Phys.* **101**, 014507 (2007).
- ²¹H. Fang, S. Chuang, T. C. Chang, K. Takei, T. Takahashi, and A. Javey, *Nano Lett.* **12**, 3788 (2012).

- ²²D. Braga, I. Gutiérrez Lezama, H. Berger, and A. F. Morpurgo, *Nano Lett.* **12**, 5218 (2012).
- ²³P. Hu, Z. Wen, L. Wang, P. Tan, and K. Xiao, *ACS Nano* **6(7)**, 5988 (2012).
- ²⁴G. W. Mudd, S. A. Svatek, T. Ren, A. Patané, O. Makarovskiy, L. Eaves, P. H. Beton, Z. D. Kovalyuk, G. V. Lashkarev, and Z. R. Kudrynskiy, *Adv. Mater.* **25**, 5714 (2013).
- ²⁵W. Jin, P. Yeh, N. Zaki, D. Zhang, J. T. Sadowski, A. Al-Mahboob, A. M. van der Zande, D. A. Chenet, J. I. Dadap, I. P. Herman, P. Sutter, J. Hone, and R. M. Osgood, *Phys. Rev. Lett.* **111**, 106801 (2013).
- ²⁶W. Zhao, Z. Ghorannevis, L. Chu, M. Toh, C. Kloc, P. Tan, and G. Eda, *ACS Nano* **7(1)**, 791 (2013).
- ²⁷Y. Ma, Y. Dai, M. Guo, L. Yu and B. Huang, *Phys. Chem. Chem. Phys.* **15**, 7098 (2013).
- ²⁸Y. Zhang, J. Ye, Y. Matsushashi, and Y. Iwasa, *Nano Lett.* **12**, 1136 (2012).
- ²⁹O. Lopez-Sanchez, D. Lembke, M. Kayci, A. Radenovic, and A. Kis, *Nat. Nanotechnol.* **9**, 497 (2013).
- ³⁰B. W. H. Baugher, H. O. H. Churchill, Y. Yang, and P. Jarillo-Herrero, *Nat. Nanotechnol.* **9**, 262 (2014).
- ³¹D. J. Late, B. Liu, J. Luo, A. Yan, H. S. S. Ramakrishna Matte, M. Grayson, C. N. R. Rao, and V. P. Dravid, *Adv. Mater.* **24**, 3549 (2012).
- ³²S. Lei, L. Ge, S. Najmaei, A. George, R. Koppera, J. Lou, M. Chhowalla, H. Yamaguchi, G. Gupta, R. Vajtai, A. D. Mohite, and P. M. Ajayan, *ACS Nano* **8**, 1263 (2014).
- ³³S. R. Tamalampudi, Y. Lu, R. Kumar U., R. Sankar, C. Liao, K. Moorthy B., C. Cheng, F. C. Chou, and Y. Chen, *Nano Lett.* **14**, 2800 (2014).

- ³⁴H. Yonezu, *Dilute III-V Nitride semiconductors and material systems: Physics and technology*, Springer series in Material Science **105**, 405 (2008).
- ³⁵C. W. Tu, *J. Phys. Condens. Matter* **13**, 7169 (2001).
- ³⁶Y. Furukawa, H. Yonezu, and A. Wakahara, *IEICE transactions on electronics* **E91C (2)**, 145 (2008).
- ³⁷S. B. Zhang and S. Wei, *Phys. Rev. Lett.* **86**, 1789 (2001).
- ³⁸D. N. Talwar, *International Conference on Emerging Trends in Electronic and Photonic Devices & Systems (ELECTRO-2009)*, 24 (2009).
- ³⁹J. F. Geisz, D. J. Friedman, J. M. Olson, S. R. Kurtz, and B. M. Keyes, *J. Cryst. Growth.* **195**, 401 (1998).
- ⁴⁰C. Skierbiszewski, P. Perlin, P. Wisniewski, W. Knap, T. Suski, W. Walukiewicz, W. Shan, K. M. Yu, J. W. Ager, E. E. Haller, J. F. Geisz and J. M. Olson, *Appl. Phys. Lett.* **76**, 2409 (2000).
- ⁴¹W. Shan, W. Walukiewicz, J. W. Ager III, E. E. Haller, J. F. Geisz, D. J. Friedman, J. M. Olson, and S. R. Kurtz, *Phys. Rev. Lett.* **82**, 1221 (1999).
- ⁴²G. Pettinari, M. Felici, R. Trotta, M. Capizzi, and A. Polimeni, *J. Appl. Phys.* **115**, 012011 (2014).
- ⁴³M. Weyers, M. Sato and H. Ando, *Jpn. J. Appl. Phys.* **31**, L 853 (1992).
- ⁴⁴S. Wei and A. Zunger, *Phys. Rev. Lett.* **76**, 664 (1996).
- ⁴⁵K. M. Yu, W. Walukiewicz, W. Shan, J. W. Ager III, J. Wu, and E. E. Haller, *Phys. Rev. B* **61**, R13337 (2000).
- ⁴⁶W. Walukiewicz, W. Shan, J. W. Ager III, D. R. Chamberlin, E. E. Haller, J. F. Geisz, D. J. Friedman, J. M. Olson, and S. R. Kurtz, *NREL/CP* **520**, 29583 (1999).
- ⁴⁷J. Wu, W. Walukiewicz, and E. E. Haller, *Phys. Rev. B* **65**, 233210 (2002).
- ⁴⁸J. Wu, W. Shan and W. Walukiewicz, *Semicond. Sci. Technol.* **17**, 860-869 (2002).

- ⁴⁹S. K. Estreicher, *Mater. Sci. Eng.* **R14**, 319 (1995).
- ⁵⁰K. B. Nielsen, B. B. Nielsen, J. Hansen, E. Andersen, and J. U. Andersen, *Phys. Rev. B* **60**, 1716 (1999).
- ⁵¹K. B. Nielsen, L. Dobaczewski, S. Søgård, and B. B. Nielsen, *Phys. Rev. B* **65**, 075205 (2002).
- ⁵²S. J. Breuer, R. Jones, P. R. Briddon, and S. Öberg, *Phys. Rev. B* **53**, 19289 (1996).
- ⁵³A. Amore Bonapasta, M. Capizzi, and P. Giannozzi, *Phys. Rev. B* **57**, 12923 (1998).
- ⁵⁴M. Capizzi, V. Emiliani, A. Frova, F. Sarto, and R. N. Sacks, *Phys. Rev. B* **47**, 12563 (1993).
- ⁵⁵A. Amore Bonapasta, M. Capizzi, and P. Giannozzi, *phys. stat. sol (b)* **210**, 277 (1998).
- ⁵⁶M. Capizzi, C. Coluzza, V. Emiliani, P. Frankl, A. Frova, F. Sarto, A. Amore Bonapasta, Z. Sobiesierski, R. N. Sacks, *J. Appl. Phys.* **72 (4)**, 1454 (1992).
- ⁵⁷M. J. Ashwin, B. R. Davidson, K. Woodhouse, R. C Newman, T. J Bullough, T. B Joyce, R. Nickling and R. R Bradley, *Semicond. Sci. Technol.* **8**, 625-629 (1993).
- ⁵⁸M. J. Ashwin, R. E. Pritchard, R. C. Newman, T. B. Joyce, T. J. Bullough, J. Wagner, C. Jeynes, S. J. Breuer, R. Jones, P. R. Briddon, and S. Öberg, *J. Appl. Phys.* **80 (12)**, 6754 (1996).
- ⁵⁹D. M. Kozuch, M. Stavola, S. J Pearton, C. R. Abernathy, and J. Lopata, *Appl. Phys. Lett.* **57**, 261 (1990).
- ⁶⁰A. Polimeni, G. Ciatto, L. Ortega, F. Jiang, F. Boscherini, F. Filippone, A. Amore Bonapasta, M. Stavola, and M. Capizzi, *Phys. Rev. B* **68**, 085204 (2003).
- ⁶¹P. J. Klar, H. Grüning, M. Güngerich, W. Heimbrod, J. Koch, T. Torunski, W. Stolz, A. Polimeni, and M. Capizzi, *Phys. Rev. B* **67**, 121206(R) (2003).

- ⁶²P. Dixon, D. Richardson, R. Jones, C. D. Latham, S. Öberg, V. J. B. Torres, and P. Briddon, *Phys. Status Solidi B* **210**, 321 (1998).
- ⁶³A. Jonotti, S. B. Zhang, and S. -H. Wei, *Phys. Rev. Lett.* **88**, 125506 (2002).
- ⁶⁴Y. -S. Kim and K. J. Chang, *Phys. Rev. B.* **66**, 073313 (2002).
- ⁶⁵A. Jonotti, S. B. Zhang, S. -H. Wei, and C. G. Van de Walle, *Phys. Rev. Lett.* **89**, 086403 (2002).
- ⁶⁶A. Amore Bonapasta, F. Filippone, P. Giannozzi, M. Capizzi, and A. Polimeni, *Phys. Rev. Lett.* **89**, 216401 (2002).
- ⁶⁷A. Amore Bonapasta, F. Filippone, and P. Giannozzi, *Phys. Rev. B* **68**, 115202 (2003).
- ⁶⁸F. Jiang, M. Stavola, M. Capizzi, A. Polimeni, A. Amore Bonapasta and F. Filippone, *Phys. Rev. B* **69**, 041309(R) (2004).
- ⁶⁹S. Kleekajai, F. Jiang, K. Colon, M. Stavola, W. B. Fowler, K. R. Martin, A. Polimeni, M. Capizzi, Y. G. Hong, H. P. Xin, C. W. Tu, G. Bais, S. Rubini, and F. Martelli, *Phys. Rev. B* **77**, 085213 (2008).
- ⁷⁰M. -H. Du, S. Limpijumnong, and S. B. Zhang, *Phys. Rev. B* **72**, 073202 (2005).
- ⁷¹A. Amore Bonapasta, F. Filippone, and G. Mattioli, *Phys. Rev. Lett.* **98**, 206403, (2007).
- ⁷²G. Ciatto, F. Boscherini, A. Amore Bonapasta, F. Filippone, A. Polimeni, M. Capizzi, M. Berti, G. Bisognin, D. De Salvador, L. Floreano, F. Martelli, S. Rubini, and L. Grenouillet, *Phys. Rev. B* **79**, 165205 (2009).
- ⁷³R. Trotta, A. Polimeni, and M. Capizzi, *Adv. Funct. Mater.* **22**, 1782 (2012).
- ⁷⁴K. S. Novoselov, V. I. Fal'ko, L. Colombo, P. R. Gellert, M. G. Schwab, and K. Kim, *Nature* **490**, 192 (2012).

- ⁷⁵D. Jariwala, V. K. Sangwan, L. J. Lauhon, T. J. Marks, and M. C. Hersam, *Chem. Soc. Rev.* **42**, 2824 (2013).
- ⁷⁶D. Jariwala, A. Srivastava, and P. M. Ajayan, *J. Nanosci. Nanotechnol.* **11**, 6621 (2011).
- ⁷⁷F. Schwierz, *Nat. Nanotechnol.* **5**, 487 (2010).
- ⁷⁸A. K. Geim and I. V. Grigorieva, *Nature* **499**, 419 (2013) and references therein.
- ⁷⁹L. A. Ponomarenko, A. K. Geim, A. A. Zhukov, R. Jalil, S. V. Morozov, K. S. Novoselov, I. V. Grigorieva, E. H. Hill, V. V. Cheianov, V. I. Fal'ko, K. Watanabe, T. Taniguchi, and R. V. Gorbachev, *Nature Phys.* **7**, 958 (2011).
- ⁸⁰S. J. Haigh, A. Gholinia, R. Jalil, S. Romani, L. Britnell, D. C. Elias, K. S. Novoselov, L. A. Ponomarenko, A. K. Geim, and Gorbachev, *Nature Mater.* **11**, 764 (2012).
- ⁸¹L. Britnell, R. V. Gorbachev, R. Jalil, B. D. Belle, F. Schedin, A. Mishchenko, T. Georgiou, M. I. Katsnelson, L. Eaves, S. V. Morozov, N. M. R. Peres, J. Leist, A. K. Geim, K. S. Novoselov, and L. A. Ponomarenko, *Science* **335**, 947 (2012).
- ⁸²T. Roy, M. Tosun, J. S. Kang, A. B. Sachid, S. B. Desai, M. Hettick, C. C. Hu, and A. Javey, *ACS Nano* **8**, 6259 (2014).
- ⁸³R. A. Kaindl, F. Eickemeyer, M. Woerner, and T. Elsaesser, *Appl. Phys. Lett.* **75**, 1060 (1999).
- ⁸⁴W. Shi and Y. Ding, *Appl. Phys. Lett.* **84**, 1635 (2004).
- ⁸⁵J. Martinez-Pastor, A. Segura, J. L. Valdés, and A. Chevy, *J. Appl. Phys.* **62**, 1477 (1987).
- ⁸⁶G. V. Lashkarev, A. I. Dmitriev, A. A. Baida, Z. D. Kovalyuk, M. V. Kondrin, and A. A. Pronin, *Semiconductors* **37**, 134 (2003).

- ⁸⁷L. Plucinski, R. L. Johnson, B. J. Kowalski, K. Kopalko, B. A. Orlowski, Z. D. Kovalyuk, and G. V. Lashkarev, *Phys. Rev. B* **68**, 125304 (2003)
- ⁸⁸J. E. Palmer, T. T. Saitoh, A. Yodo, and M. Tamura, *Cryst. Growth* **150**, 685 (1995).
- ⁸⁹L. C. T. Shoute and D. F. Kelly, *J. Phys. Chem. C* **111**, 10233 (2007).
- ⁹⁰A. G. Kyzym-zade, V. M. Salmanov, A. G. Guseinov, L. G. Gasanova, and R. M. Mamedov, *Opt. Spectrosc.* **116**, 595 (2013).
- ⁹¹D. H. Mosca, N. Mattoso, C. M. Lepienski, W. Veiga, I. Mazzaro, V. H. Etgens, and M. Eddrief, *J. Appl. Phys.* **91**, 140 (2002).
- ⁹²V. N. Katerinchuk, Z. D. Kovalyuk, V. V. Netyaga, and T. V. Betsa, *Inorg. Mater.* **37**, 336 (2001).
- ⁹³O. Madelung, *Semiconductor: Data Handbook*, Springer, London, (2003).
- ⁹⁴M. Millot, J. M. Broto, S. George, J. Gonzalez, and A. Segura, *Phys. Rev. B* **81**, 205211 (2010).
- ⁹⁵Z. D. Kovalyuk, V. N. Katerinchuk, and T. V. Betsa, *Opt. Mater.* **17**, 279 (2001).
- ⁹⁶V. Zòlyomi, N. D. Drummond, and V. I. Fal'ko, *Phys. Rev. B* **89**, 205416 (2014).
- ⁹⁷W. Feng, W. Zheng, W. Cao, and P. Hu, *Adv. Mater.* (2014); DOI: 10.1002/adma.201402427.
- ⁹⁸A. Segura, J. Bouvier, M. V. Andrés, F. J. Manjón, and V. Muñoz, *Phys. Rev. B* **56**, 4075 (1997).
- ⁹⁹S. Lei, L. Ge, Z. Liu, S. Najmaei, G. Shi, G. You, J. Lou, R. Vajtai, and P. M. Ajayan, *Nano Lett.* **13**, 2777 (2013).
- ¹⁰⁰K. R. Allakhverdiev, M. Ö. Yetis, S. Özbek, T. K. Baykara, and E. Yu. Salaev, *Laser Phys.* **19**, 1093 (2009).

- ¹⁰¹S. M. Sze and M. K. Lee, *Semiconductor devices physics and technology*, John Wiley & sons, Singapore, 3rd Ed., Ch. 3, p.82 (2013).
- ¹⁰²S. M. Sze, *Physics of semiconductor devices*, John Wiley & sons, Singapore, 2rd Ed., Ch. 2, p.117 (1981).
- ¹⁰³A. P. Godse, U. A. Bakshi, and A. V. Bakshi, *Electron devices*, Technical publications Pune, p.5-29 (2008).
- ¹⁰⁴H. Mizuta and T. Tanoue, *The Physics and Applications of Resonant Tunnelling Diodes*, Cambridge University Press, UK, (1995).
- ¹⁰⁵C. R. H. White, H. B. Evans, L. Eaves, P. M. Martin, M. Henini, G. Hill, and M. A. Pate, *Phys. Rev. B* **45**, 9513 (1992).
- ¹⁰⁶R. Tsu, *Superlattice to Nanoelectronics*, Elsevier, London (2011).
- ¹⁰⁷S. Wang, *Fundamentals of semiconductor theory and device physic*, Prentice-Hall, Inc., USA, p.146 (1989).
- ¹⁰⁸J. H. Davies, *The physics of low dimensional semiconductors: an Introduction*, Cambridge university press, UK, (1998).
- ¹⁰⁹D. J. Sharp, J. K. G. Panitz, and D. M. Mattox, *J. Vac. Sci. Technol.* **16**, 1879 (1979).
- ¹¹⁰R. Trotta, D. Giubertoni, A. Polimeni, M. Bersani, M. Capizzi, F. Martelli, S. Rubini, G. Bisognin, and M. Berti, *Phys. Rev. B* **80**, 195206 (2009).
- ¹¹¹G. Pettinari, N. Balakrishnan, O. Makarovsky, R. P. Champion, A. Polimeni, M. Capizzi, and A. Patanè, *Appl. Phys. Lett.* **103**, 241105 (2013).
- ¹¹²N. Balakrishnan, G. Pettinari, O. Makarovsky, M. Hopkinson, and A. Patanè, *Appl. Phys. Lett.* **104**, 242110 (2014).
- ¹¹³V. N. Katerinchuk and M. Z. Kovalyuk, *Phys. Stat. Sol. (a)* **133**, K45 (1992).

- ¹¹⁴O. Lang, C. Pettenkofer, J. F. Sanchez-Royo, A. Segura, A. Klein and W. Jaegermann, *J. Appl. Phys.* **86**, 5687 (1999).
- ¹¹⁵O. A. Balitskii, N. N. Berchenko, V. P. Savchyn, J. M. Stakhira, *Mater. Chem. Phys.* **65**, 130 (2000).
- ¹¹⁶HR800 user manual, Horiba Jobin Yvon.
- ¹¹⁷Advanced Research System, Inc. www.arscopy.com.
- ¹¹⁸www.utu.fi/fi/yksikot/sci/yksikot/fysiikka/laboratoriot/materiaali/materiaalitiede/tutkimusmenetelmat/sem/Sivut/home.aspx
- ¹¹⁹A. Patané and N. Balkan, *Semiconductor Research: Experimental Techniques* Springer, Heidelberg, (2012).
- ¹²⁰<http://www.mtholyoke.edu/~menunez/ResearchPage/AFM.html>
- ¹²¹K. Fukui, H. Onishi, and Y. Iwasawa, *Phys. Rev. Lett.* **79**, 4202 (1997).
- ¹²²E. A. Davis, S. F. J. Cox, R. L. Lichti, C. G. Van de Walle, *Appl. Phys. Lett.* **82**, 592 (2003).
- ¹²³N. Balakrishnan, A. Patané, O. Makarovskiy, A. Polimeni, M. Capizzi, F. Martelli, and S. Rubini, *Appl. Phys. Lett.* **99**, 021105 (2011).
- ¹²⁴R. Carron, D. Fekete, P. Gallo, B. Dwir, A. Rudra, M. Felici, B. Bartova, M. Cantoni, and E. Kapon, *Appl. Phys. Lett.* **99**, 101107 (2011).
- ¹²⁵M. Henini, *Dilute Nitride Semiconductors*, Elsevier, Amsterdam, (2005).
- ¹²⁶A. Lindsay and E. P. O'Reilly, *Phys. Rev. Lett.* **93**, 196402 (2004).
- ¹²⁷M. Lax, *J. Appl. Phys.* **48**, 3919 (1977).
- ¹²⁸J. S. Blakemore, *J. Appl. Phys.* **53**, R123 (1982).
- ¹²⁹N. Kobayashi and Y. Kobayashi, *Jpn. J. Appl. Phys. Part 2 - Lett.* **30**, L1699 (1991).

- ¹³⁰L. Felisari, V. Grillo, F. Martelli, R. Trotta, A. Polimeni, M. Capizzi, F. Jabeen, and L. Mariucci, *Appl. Phys. Lett.* **93**, 102116 (2008).
- ¹³¹P. V. Santos, N. M. Johnson, and R. A. Street, *Phys. Rev. Lett.* **67**, 2686 (1991).
- ¹³²D. Loridant-Bernard, S. Meziere, M. Constant N. Dupuy, S. Sombret, and J. Chevalier, *Appl. Phys. Lett.* **73**, 644 (1998).
- ¹³³A. Polimeni, M. Bissiri, M. Felici, M. Capizzi, I. A. Buyanova, W. M. Chen, H. P. Xin, and C. W. Tu, *Phys. Rev. B* **67**, 201303R (2003).
- ¹³⁴H. P. Xin, C. W. Tu, Zhang, and A. Mascarenhas, *Appl. Phys. Lett.* **76**, 1267 (2000).
- ¹³⁵N. Balakrishnan, G. Pettinari, O. Makarovsky, L. Turyanska, M. W. Fay, M. De Luca, A. Polimeni, M. Capizzi, F. Martelli, S. Rubini, and A. Patanè, *Phys. Rev. B* **86**, 155307 (2012).
- ¹³⁶S. Spasov, G. Allison, A. Patanè, L. Eaves, M. Hopkinson, and R. Airey, *J. Appl. Phys.* **100**, 063718 (2006).
- ¹³⁷R. De L. Kronig and W. G. Penney, *Proc. R. Soc. Lond. A* **130**, 499 (1931).
- ¹³⁸W. L. Hansen, E. E. Haller, and P. N. Luke, *IEEE Trans. Nucl. Sci.* **29**, 738 (1982).
- ¹³⁹K. Bergman, M. Stavola, S. J. Pearton, and J. Lopata, *Phys. Rev. B* **37**, 2770 (1988).
- ¹⁴⁰S. Kurtz, J. Webb, L. Gedvilas, D. Friedman, J. Geisz, J. Olson, R. King, D. Joslin, and N. Karam, *Appl. Phys. Lett.* **78**, 748 (2001).
- ¹⁴¹O. Makarovsky, S. Kumar, A. Rastelli, A. Patanè, L. Eaves, A. G. Balanov, O. G. Schmidt, R. Champion, and C. T. Foxon, *Adv. Mater.* **22**, 3176 (2010).
- ¹⁴²P. S. Nandhra, R. C. Newman, R. Murray, B. Pajot, J. Chevallier, R. B. Beall, and J. J Harris, *Semicond. Sci. Technol.* **3**, 356 (1988).

- ¹⁴³A. Bell, S. Srinivasan, C. Plumlee, H. Omiya, F. A. Ponce, J. Christen, S. Tanaka, A. Fujioka, and Y. Nakagawa, *J. Appl. Phys* **95**, 4670 (2004).
- ¹⁴⁴J. Li, S. Iyer, S. Bharatan, L. Wu, K. Nunna, W. Collis, K. K. Bajaj and K. Matney, *J. Appl. Phys* **98**, 013703 (2005).
- ¹⁴⁵V. M. Ustinov, N. A. Cherkashin, N. A. Bert, A. F. Tsatsul'nikov, A. R. Kovsh, J. Wang, L. Wei, and J. Y. Chi, *Mat. Res. Soc. Symp. Proc* **692**, H1.10 (2002).
- ¹⁴⁶J. Herrnsdorf, E. Xie, I. Watson, N. Laurand, and M. Dawson, *J. Appl. Phys.* **115**, 084503 (2014).
- ¹⁴⁷V. Poher, H. X. Zhang, G. T. Kennedy, C. Griffin, S. Oddos, E. Gu, D. S. Elson, J. M. Girkin, P. M. W. French, M. D. Dawson, and M. A. A. Neil, *Opt. Express* **15**, 11196 (2007).
- ¹⁴⁸V. Poher, N. Grossman, G. T. Kennedy, K. Nikolic, H. X. Zhang, Z. Gong, E. M. Drakakis, E. Gu, M. D. Dawson, P. M. W. French, P. Degenaar, and M. A. A. Neil, *J. Phys. D: Appl. Phys.* **41**, 094014 (2008).
- ¹⁴⁹M. Vitzethuma, R. Schmidta, P. Kiesela, P. Schafmeisterb, D. Reuterb, A. D. Wieckb, and G. H. Dohlera, *Physica E* **13**, 143 (2002).
- ¹⁵⁰S. Li and A. Waag, *J. Appl. Phys.* **111**, 071101 (2012).
- ¹⁵¹F. Intonti, V. Matarazzo, A. Nasir, O. Makarovsky, R. Campion, A. Patane`, S. Kumar, A. Rastelli, O. G. Schmidt, and M. Gurioli, *Appl. Phys. Lett.* **98**, 183102 (2011).
- ¹⁵²J. Zaumseil, R. H. Friend, and H. Sirringhaus, *Nature Mater.* **5**, 69 (2006).
- ¹⁵³J. Liu, I. Engquist, X. Crispin, and M. Berggren, *J. Am. Chem. Soc.* **134**, 901 (2012).
- ¹⁵⁴B. B. Y. Hsu, C. Duan, E. B. Namdas, A. Gutacker, J. D. Yuen, F. Huang, Y. Cao, G. C. Bazan, I. D. W. Samuel, and A. J. Heeger, *Adv. Mater.* **24**, 1171 (2012).

- ¹⁵⁵S. W. Culligan, A. C.-A. Chen, J. U. Wallace, K. P. Klubek, C. W. Tang, and S. H. Chen, *Adv. Funct. Mater.* **16**, 1481 (2006).
- ¹⁵⁶P. M. Martin, R.K. Hayden, C.R.H. White, M. Henini, L. Eaves, D.K. Maude, J.C. Portal, G. Hill, M.A. Pate, *Semicond. Sci. Technol.*, **7**, B456 (1992).
- ¹⁵⁷N. Pan, S.S. Bose, M.H. Kim, G.E. Stillman, F. Chambers, G. Devane, C.R. Ito, M. Feng, *Appl. Phys. Lett.* **51**, 596 (1987).
- ¹⁵⁸R. Rahbi, B. Pajot, J. Chevallier, A. Marbeuf, R.C. Logan, M. Gavand, *J. Appl. Phys.* **73**, 1723 (1993).
- ¹⁵⁹C. Bayram, Z. Vashaei, M. Razeghi, *Appl. Phys. Lett.* **97**, 092104 (2010).
- ¹⁶⁰Y. Suda, H. Koyama, *Appl. Phys. Lett.*, **79**, 2273 (2011).
- ¹⁶¹F. Capasso, K. Mohammed, and A. Y. Cho, *IEEE J. Quantum Electron.* **22**, 1853 (1986).
- ¹⁶²J. Kim, O. Benson, H. Kan, and Y. Yamamoto, *Nature* **397**, 500 (1999).
- ¹⁶³A. J. Shields, *Nature Photon.* **1**, 215 (2007).
- ¹⁶⁴A. D. Yoffe, *Annu. Rev. Mater. Sci.* **3**, 147 (1973).
- ¹⁶⁵K. S. Novoselov, D. Jiang, F. Schedin, T. J. Booth, V. V. Khotkevich, S. V. Morozov, and A. K. Geim, *PNAS* **102**, 10451 (2005).
- ¹⁶⁶T. Georgiou, R. Jalil, B. D. Belle, L. Britnell, R. V. Gorbachev, S. V. Morozov, Y. J. Kim, A. Gholinia, S. J. Haigh, O. Makarovskiy, L. Eaves, L. A. Ponomarenko, A. K. Geim, K. S. Novoselov, and A. Mishchenko, *Nature Nanotech.* **8**, 100 (2013).
- ¹⁶⁷C. R. Dean, A. F. Young, I. Meric, C. Lee, L. Wang, S. Sorgenfrei, K. Watanabe, T. Taniguchi, P. Kim, K. L. Shepard, J. Hone, *Nature Nanotech.* **10**, 722 (2010).
- ¹⁶⁸D. Jariwala, V. K. Sangwan, L. J. Lauhon, T. J. Marks, M. C. Hersam, *ACS Nano* **8**, 1102 (2014).

- ¹⁶⁹W. J. Yu, Y. Liu, H. Zhou, A. Yin, Z. Li, Y. Huang, X. Duan, *Nature Nanotech.* **8**, 952 (2013).
- ¹⁷⁰A. Pospischil, M. M. Furchi, T. Mueller, *Nature Nanotech.* **9**, 257 (2014).
- ¹⁷¹J. S. Ross, P. Klement, A. M. Jones, N. J. Ghimire, J. Yan, D. G. Mandrus, T. Taniguchi, K. Watanabe, K. Kitamura, W. Yao, D. H. Cobden, X. Xu, *Nature Nanotech.* **9**, 268 (2014).
- ¹⁷²H. P. Hughes and H. I. Starnberg, eds., *Electron Spectroscopies Applied to Low-Dimensional Materials*; Kluwer Academic Publishers: Dordrecht, Netherlands, 317 (2000).
- ¹⁷³K. F. Mak, C. Lee, J. Hone, J. Shan, T. F. Heinz, *Phys. Rev. Lett.* **105**, 136805 (2010).
- ¹⁷⁴A. Splendiani, L. Sun, Y. Zhang, T. Li, J. Kim, C. Y. Chim, G. Galli, and F. Wang, *Nano Lett.* **10**, 1271 (2010).
- ¹⁷⁵O. Lang, A. Klein, C. Pettenkofer, W. Jaegermann, A. Chevy, *J. Appl. Phys.*, **80**, 3817 (1996).
- ¹⁷⁶H. Nakazawa, Y. Ito, E. Matsumoto, K. Adachi, N. Aoki, and Y. Ochiai, *J. Appl. Phys.* **100**, 093706 (2006).
- ¹⁷⁷G. B. Bachelet, *Crystalline Semiconducting Materials and Devices*; P. N. Butcher, N. H. March, M. P. Tosi, Eds.; Plenum: New York, 243 (1986).
- ¹⁷⁸S. Tsujino, A. Borak, E. Müller, M. Scheinert, C. V. Falub, H. Sigg, D. Grützmacher, M. Giovannini, and J. Faist, *Appl. Phys. Lett.* **86**, 062113 (2005).
- ¹⁷⁹Ch. Ferrer-Roca, A. Segura, M. V. Andrés, J. Pellicer, and V. Muñoz, *Phys. Rev. B* **55**, 6981 (1997).

¹⁸⁰A. Polimeni, G. Baldassarri Höger von Högersthal, M. Bissiri, V. Gaspari, F. Ranalli, M. Capizzi, A. Frova, A. Miriametro, M. Geddo, M. Fischer, M. Reinhardt, and A. Forchel, *Physica B* **308**, 850 (2001).

¹⁸¹M. Feiginov, C. Sydlo, O. Cojocari, P. Meissner, *Appl. Phys. Lett.* **99**, 233506 (2011).

¹⁸²J. C. Blakesley, P. See, A.J. Shields, B.E. Kardynał, P. Atkinson, I. Farrer, D. A. Ritchie, *Phys. Rev. Lett.* **94**, 067401 (2005).

¹⁸³O. Makarovskiy, O. Thomas, A. G. Balanov, L. Eaves, A. Patanè, R. P. Champion, C. T. Foxon, E. E. Vdovin, D. K. Maude, G. Kiesslich, and R. J Airey, *Phys. Rev. Lett.* **101**, 226807 (2008).